UNIVERSITÀ DEGLI STUDI DI TRIESTE

UNIVERSITÀ DEGLI STUDI DI TRIESTE

XXXV CICLO DEL DOTTORATO DI RICERCA IN

NANOTECNOLOGIE

Borsa MIUR/Ateneo cofinanziata dal Dipartimento di Fisica su fondi CNR-IOM

EXPLORING CARDIAC MECHANOBIOLOGY USING NANOTECHNOLOGY

Settore scientifico-disciplinare: **FIS/07**

DOTTORANDO
MICHELE ZANETTI

COORDINATORE
PROF. ALBERTO MORGANTE.

SUPERVISORE DI TESI
DR. MARCO LAZZARINO

CO-SUPERVISORE DI TESI
DR.SSA LAURA ANDOLFI

ANNO ACCADEMICO 2021/2022

Preface

For 28 short years, John lived an extraordinary life. As a professional NBA player, he inspired countless people with his passion and hard work. But on the night of his last game, John was found lifeless in his bed. An autopsy later revealed that John had a form of silent cardiomyopathy and had died of sudden cardiac arrest.

While John's story may be fictional, such represented tragedy is far from being so. Cardiovascular diseases in their many forms are the leading cause of death worldwide according to the World Health Organization and many efforts are being taken to tackle this global epidemic.

During recent years, studying the mechanical properties of the myocardium has become an imperative task that biophysicists must face to build accurate disease prediction models, regeneration strategies, and drug screening and testing tools.

In this dissertation, nanotechnological tools will be applied to highlight new insights into the mechanobiology of cardiac physiology and disease.

In the first two chapters, an overview of heart tissue mechanics from the macro to the nanoscale will be provided, and current strategies to investigate heart mechanics will be discussed, with a focus on Atomic Force Microscopy (AFM) based approaches.

In the third chapter, an study on two dimensional cultures of filamin C-mutated cardiac cells will be presented, as an example of how the AFM can easily disclose *significant* biophysical markers of the diseased cardiomyocyte.

Three-dimensional cardiac spheroids will be then introduced in the fourth chapter as superior physiological-like myocardial models, together with an innovative strategy to study and trigger their functional response at the whole-spheroid level, through the application of novel custom-fabricated AFM macro-cantilevers.

After the foundations of such models are laid down, a further application of this AFM-based strategy will be discussed in chapter five, as of a biophysical investigation of cardiac spheroids specifically tuned to display some pathological traits of fibrotic remodeling.

Finally, in the last chapter, the in-vitro maturation of a myocardial regenerative model will be presented in the form of a passive electromechanical conditioning by means of nanoengineered reverse thermal gels.

Abstract

Nanotechnological tools applied to the field of Heart Biophysics have advanced the knowledge about the role of mechanics on cardiac physiopathology. Two-dimensional (2D) and three-dimensional (3D) cardiomyocytes cultures enable a systematic manipulation and precise control of force dynamics, to address the myocardial multiscale organization and mechanobiology.

In this dissertation, an analysis performed on a 2D culture of Filamin C-truncated cardiomyocytes showed cell stiffness and adhesion impairments as measured by Atomic Force Microscopy (AFM) loading-unloading sweeps.

To investigate a physiological-like system, multicellular 3D cardiac spheroids (CSs) were developed to bridge the gap between 2D cultures and the heart tissue. The measure of CSs mechanical properties by AFM required *Macro-cantilevers* to be purposedly fabricated, in order to interrogate the CS whole mechanics.

After having optimized such AFM-based approach, a pathological complexity layer was added by probing spheroids of co-cultured cardiomyocytes and fibroblasts, aiming to analyze the mechanical background of myocardial fibrosis (MF). In this study, myocardial fibrotic spheroids showed higher stiffnesses, which represents a hallmark of MF.

Finally, in the framework of a possible regeneration strategy, a nanoengineering-guided passive electromechanical conditioning was combined with dynamic AFM loadings, disclosing an improved CSs contractile performance. CSs grown in conductive hydrogels exhibited advanced maturation levels as shown by an enhanced gap junctions' expression, higher reactivity to the AFM mechanical pacing and, in turn, higher twitch power.

The results herein presented are likely to bring a positive impact on the study of heart regeneration and cardiovascular diseases, pushing towards unexplored venues of cardiac mechanobiology through nanotech-inspired bioengineering tools.

TABLE OF CONTENTS

Chapter 1

Heart mechanics from the Macro to the Nanoscale

1.1 Cardiac Mechanics at the Macroscale

1.1.1 An anatomical overview

The heart is a vital organ playing a central role in the circulatory system of humans and other mammals. It is located behind the breastbone, slightly to the left, and sits on the diaphragm. Histologically, it is made of multiple layers of tissue, including the myocardium, pericardium, and endocardium, which work together to ensure that blood is effectively pumped all over the body.

Indeed, the heart acts like a biological pump. Its cavity is divided into a right and left side, with each side further split into two chambers: an atrium and a ventricle. Accordingly, the heart can be thought of as a *double* pump that propels blood through *two distinct* circuits: the pulmonary circulation, and the systemic circulation.

The right atrium collects venous blood coming from the upper body through the superior vena cava, and blood from the lower body via the inferior vena cava. The, such deoxygenated blood passes through the tricuspid valve to the right ventricle, which propels it through the pulmonary artery toward the lungs. Here, venous blood meets inhaled air, absorbs oxygen, and releases carbon dioxide.

Oxygenated blood returns to the left atrium through the pulmonary veins. The left atrium transfers the oxygenated blood through the mitral valve to the left ventricle (LV), which is the strongest chamber of the heart. The left ventricle pumps the oxygen-rich blood through the aorta to the rest of the body, where it supplies oxygen and nutrients to the cells. The right and left atria work in coordination with the right and left ventricles to ensure that oxygen-rich blood is continuously circulated throughout the body.

1.1.2 The cardiac cycle: electrical considerations

The heart's rhythmic beating is caused by the repeated contraction and relaxation of the myocardium. These contractions are prompted by electrical signals from a natural pacemaker, the sinoatrial (SA) node in the right atrium. An electrical signal from the SA node triggers the two atria to contract, pushing blood into the ventricles.

The contraction of the ventricles is controlled by electrical signals from the atrioventricular (AV) node at the junction of the two atria. After the ventricles contract, they relax, and the pressure inside them decreases. Oxygenated blood from the pulmonary circulation flows back into the atria, and a new electrical impulse from the SA node starts the cycle again. This process is known as the cardiac cycle.

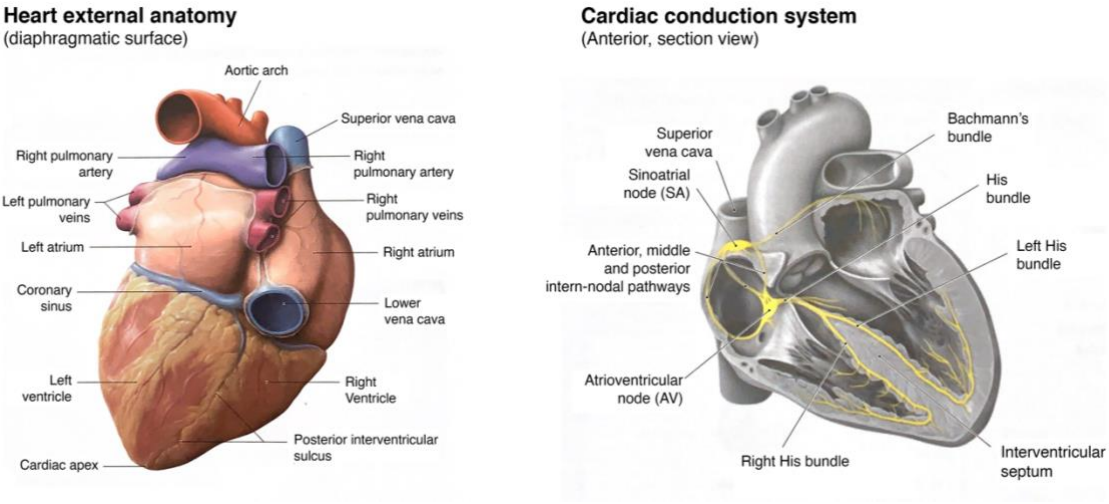

Figure 1.1 The anatomy of the heart and its electrical conduction system. Pictures are sourced and later modified from *Prometheus – Atlante di Anatomia (Anne M. Gilroy et al.)*

The contraction is called systole, while the relaxation it is called diastole. Diastole is the longer of these two, allowing the heart some rest time in-between.

Heartbeat rate varies during different circumstances such as exercise, emotional excitement, and sleep. In humans, the average adult rate is 70 beats per minute at rest. The rhythmic pulsation felt on the chest, coinciding with the heartbeat, is called the apex beat. It is caused by pressure exerted on the chest wall at the beginning of systole by the rounded and hardened ventricular wall.

1.1.3 The cardiac cycle: mechanical considerations

The main task of the LV is to circulate blood to the various organs and extremities of the body. This pumping action efficacy is influenced by various factors, such as the strength of myocardial contractions, the blood loading conditions, the size and shape of the LV, and the valve function. Thus, biomechanics plays a critical role in determining the heart pumping performance.

1.1.3.1 The ventricular pressure-volume relationship

At the beginning of the systolic phase, the LV is filled with blood up to a pressure of around 8 mm Hg and pressures higher than 16 mm Hg are considered abnormal. Both the mitral valve and the aortic valve are closed at this stage. The active contraction of the LV myocardium rapidly increases the fluid pressure above the aortic pressure. At this stage no blood flows in or out the LV, so it is referred to as *isovolumetric contraction* stage. Once the blood pressure inside the LV overcomes the aortic pressure, the aortic valve opens, and the pressurized blood is pushed out of the chamber and into circulation. This stage is known as *ejection phase*. As the contractile force generated by the LV decreases, the blood into the LV chamber falls below the systemic circulatory pressure and the aortic valve closes, marking the end of the ejection phase and of the whole systole itself.

During the initial phase of diastole, an *isovolumetric relaxation* happens, as the relaxation of LV wall leads to a rapid decrease in pressure within the LV chamber. As the pressure in the chamber falls below that of the left atria, the mitral valve opens, allowing for blood to flow into the LV chamber. The contraction of the atria pushes the residual blood inside the LV and raises the pressure within the chamber to its end-diastolic level. This phase of the cardiac cycle is known as the diastolic filling phase.

The cardiac cycle can be effectively illustrated using a pressure-volume (PV) diagram, which displays the cycle as a counterclockwise loop (Figure 1.2, right). The left and right halves of the loop represent the isovolumetric contraction and isovolumetric relaxation phases, respectively, while the bottom segment represents the filling phase and the top segment represents the ejection phase. The volume difference enclosed within the loop is known as the *stroke volume*, while the total area enclosed by the loop is referred to as the *stroke work* (SW) and quantifies the energy imparted by the left ventricle to the ejecting blood. SW is a crucial measure of cardiac function, reflecting the level of effort exerted by the LV. Sarnoff and Berglund [x] were the first to report SW and calculated it in units of [gfm] (i.e., grams force-meters), but listed the units simply as gram-meters. Over time, this frequent misreporting has led to confusion. As the SW is a measure of *work*, the correct units would be [mmHg – mL], or simply Joules.

Typically, diastolic PV curves are exponential, consistent with the exponential stress-strain behavior of most biological soft tissues. By superimposing distinct cardiac cycles with different *end-diastolic volumes*, two significant mechanical relationships are determined, namely the *end-diastolic pressure volume* relationship (EDPVR) and the *end-systolic pressure volume* relationship (ESPVR), both of which are depicted in Figure 1.2.

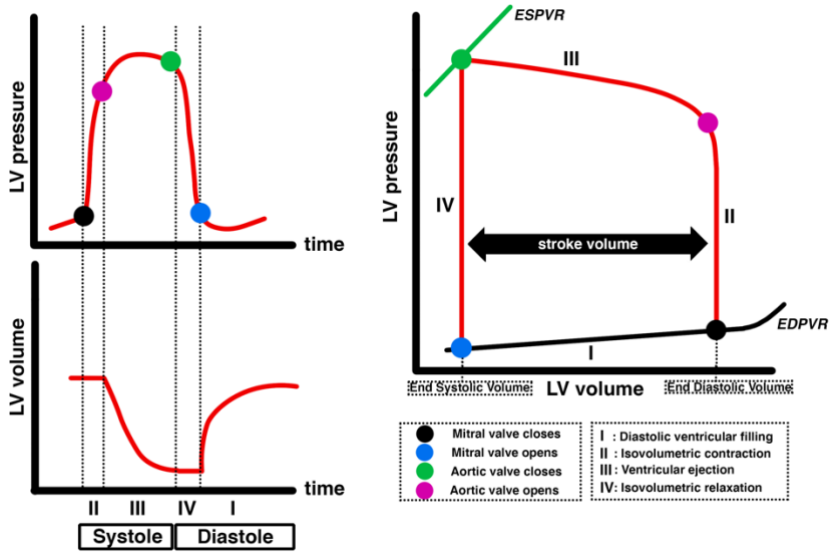

Figure 1.2. Normal Pressure-Volume diagram where blood pressure and volumetric changes of the LV are compared, highlighting valves and cardiac cycle dynamics.

1.1.3.2 The Starling's Law of the Heart

As an increase in diastolic volume stretches the myocardial tissue, it leads to an increase in blood pressure. Therefore, the PV curve reflects the passive mechanical properties of the myocardium, with volume corresponding to *strain* and pressure equivalent to *stress*.

The Starling's Law of the Heart is a fundamental principle of ventricular mechanics. Such principle tells that an increase in diastolic filling leads to an increase in the heart stroke volume, which can be observed by examining the PV curves and noting that as the volume of blood during diastole increases, the end-diastolic point on the EDPVR moves farther away from the ESPVR, thereby increasing the stroke volume.

Diastolic dysfunction is a condition in which the heart's ventricular muscle becomes stiff, leading to a change in the shape of the heart. This results in a decrease in the

heart's ability to pump blood effectively. The EDPVR shifts upward and leftward due to the stiffening, and rightward if an adverse remodeling causes the LV to dilate.

The ESPVR relates the amount of blood left in the ventricle to a given aortic pressure. As the aortic pressure increases, the less amount of blood is able to leave the LV. ESPVR is generally linear, and the slope of this relationship is referred to as the maximum elastance. This is a measure of the contractile ability of the LV for a given inotropic state. Inotropic state refers to the performance of contraction and, therefore, can be affected by various inotropic drugs. For example, hormones like epinephrine or drugs like beta blockers alter the maximum elastance and changes – in both directions – the amount of blood the LV is able to eject. Hence, inotropic agents are currently being investigated as a potential therapy for heart failure, but the results of clinical trials have been mixed [x].

1.1.3.3 Stroke Volume and Ejection Fraction

Many parameters can be used to quantify heart function. However, since the organ's main purpose is to pump blood, the most useful ones quantify the actual volume of blood being pumped. Accordingly, Stroke Volume (SV) is defined as the difference between LV volume at end-diastole (EDV) and LV volume at end-systole (ESV), which is represented by width of the pressure-volume loop (Figure 1.2).

$$\mathrm{SV} = \mathrm{EDV} - \mathrm{ESV}$$

While SV represents the amount of blood the heart is pumping pumps per each beat, another parameter is often associated while describing heart function: it goes under the name of ejection fraction (EF).

$$EF = \frac{SV}{EDV} \cdot 100$$

As the LV size varies subjectively, the EF is normalized by the EDV as noticeable by equation (2). The human EF typically sits between 50% and 80%, and readings below are strongly associated to heart failure.

1.1.4 Heart pathophysiology

Heart Failure (HF) is a complex syndrome characterized by the inability of the heart to pump blood efficiently. In HF, the heart muscle's contractility is affected, leading to a lowered EF. The heart's ability to fill with blood is also compromised, leading to an increase in EDV. Such changes in cardiac mechanics lead to an imbalance between the heart's oxygen supply and demand, causing a cascade of pathophysiological changes, such as inflammation and myocardial fibrosis (MF).

It is important to note that HF is not a disease *per se*, but rather a group of signs and symptoms caused by a *variety* of diseases displaying a common underlying paradigm: they all put the heart muscle to strain. A detailed discussion about each of these diseases and clinical presentations goes beyond the scope of this dissertation, however, some of them are introduced to provide context, as they represent the pathophysiological background of what will be tackled in the next chapters.

1.1.4.1 Cardiomyopathies

Cardiomyopathies are a group of disorders affecting the structure of the heart muscle and hence its functionality. These diseases cause the thickening, weakening, or stiffening of the heart muscle, leading to several mechanical implications.

In *Dilated Cardiomyopathy*, also known as DCM, the LV becomes enlarged and weakened. This results in decreased contractility and increased EDV. DCM can be caused by a variety of factors including, but not limited to, genetic mutations, viral infections, or alcohol abuse. It is a common complication of other heart conditions such as hypertension, valvular heart disease and thyroid disorders. DCM can cause heart failure, arrhythmias, and can also lead to sudden cardiac death.

Hypertrophic cardiomyopathy (HCM) is a condition where the heart muscle thickens, leading to impaired diastolic filling and increased wall stress. This thickening can happen in any part of the heart, but it is most commonly affecting the interventricular septum. Consequently, HCM obstructs blood flow through the LV outflow tract, leading to arrhythmias and possibly to sudden cardiac death, as well as to a vast plethora of complications (being DCM itself one of them). HCM is one of the

commonest inherited heart diseases, occurring in at least 1:500 of the general population [x].

In *Restrictive Cardiomyopathy* (RCM), the heart muscle stiffens. Its etiology is mostly genetic [x], leading to heart failure and arrhythmias as well. RCM is an issue in the way the ventricles fill and adapt. HCM, though similar in its hemodynamics, is more varied in its presentations and is primarily caused by ventricular hypertrophy.

Arrhythmogenic Cardiomyopathy (ACM) is a genetic heart condition characterized by the fibrofatty replacement of an otherwise healthy heart muscle. ACM primarily affects the right ventricle. The difference between right-ventricular ACM (RVACM) and left-ventricular ACM (LVACM) is the location and extent of the fibrofatty replacement.

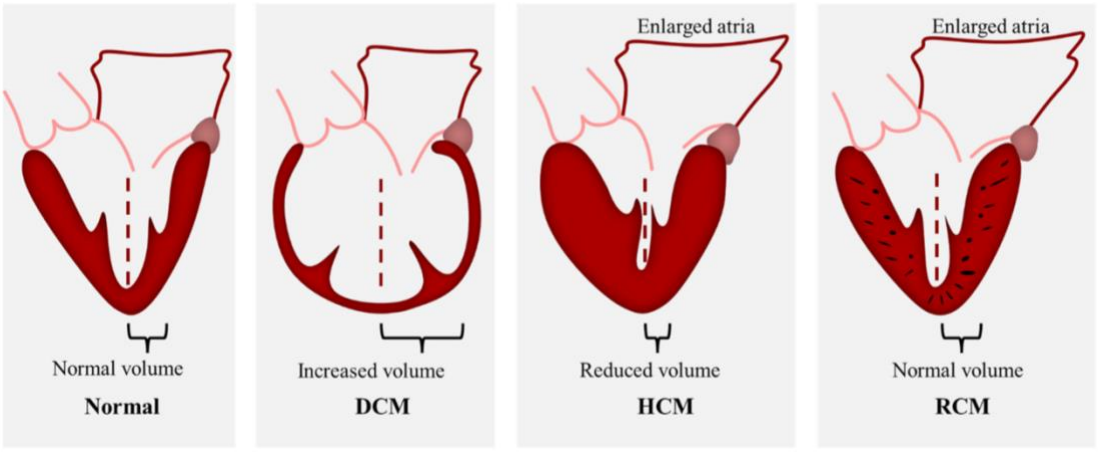

Figure 1.3. A depiction of the main morphological features of DCM, HCM, and RCM, with respect to a healthy heart. (Hassoun et al., 2021)

Overall, cardiomyopathies are a diverse group of heart muscle disorders that can present with a wide range of symptoms and clinical features. While each type of cardiomyopathy has its own specific set of mechanical features, it is important to note that these disorders often overlap in their manifestation. Moreover, there is always the possibility of co-occurring cardiac conditions displaying similar clinical presentations, such in the case of coronary artery disease. Hence, cardiomyopathies are a challenging and multifaceted issue that calls for a multidisciplinary approach to better understand their pathophysiological fingerprint.

1.1.4.2 Myocardial Infarction

Myocardial infarction (MI) is commonly known as a *heart attack*. It is a serious medical condition that occurs when the blood flow to a portion of the heart is blocked, leading to a reduced oxygen perfusion (i.e., to *ischemia*) and, therefore, a damage or death of heart muscle therein.

This blockage can be caused by a variety of factors, including the arteriosclerotic buildup, thrombosis, or spasms in the coronary arteries.

The mechanical consequences of MI can be significant. In the short-term, the damaged tissue leads to changes in the heart's pumping ability and can be generally revealed as marked lowering in the LV EF. Moreover, such damage can cause the left ventricle to dilate, which further decreases EF while increasing the risk of heart failure. The dilated left ventricle may also cause the walls of the ventricle to become thinner, which can lead to an increased risk of arrhythmias and sudden cardiac death.

The long-term consequences of MI can be equally serious. One of the most significant is the development of HF, which can result in symptoms such as shortness of breath, fatigue, and fluid accumulation in the lungs and legs. Another long-term consequence of MI is the formation of scar tissue which is, in turn, the hallmark of myocardial fibrosis.

1.1.4.3 Myocardial Fibrosis

Myocardial fibrosis is a pathological condition where the heart's extracellular matrix (ECM) is altered. The ECM is the structural architecture of the heart and, when it changes, it can lead to the thickening and stiffening of the heart's walls. Myocardial fibrosis is classified into two categories: *replacement* and *interstitial* fibrosis. Replacement fibrosis typically results from tissue necrosis following a myocardial infarction (MI) but is associated with conditions such as HCM itself (for which it represents a hallmark), sarcoidosis, myocarditis, chronic renal insufficiency, and toxic cardiomyopathies. Interstitial fibrosis is characterized as diffuse and can be further divided into *reactive* and *infiltrative* subtypes. The former is present in various diseases including aging and hypertension, while the latter, a less common occurrence, is caused by progressive accumulation of insoluble proteins in the interstitial space. Ultimately, both interstitial and infiltrative fibrosis may lead to replacement fibrosis.

The fibrotic remodeling of the heart leads to myocardial scarring, which further stiffens the heart. This, in turn, elevates the pressure within the heart chambers, leading to poor mechanical compliance. Hence, MF represents one of the main structural correlates of HF. and it will be furtherly discussed in more depth at the micro and nanoscales.

1.2 Cardiac Mechanics: from Micro to Nanoscale

1.2.1 Histological overview

The myocardium is a complex tissue that requires a specialized structure and function to carry out its vital role in the circulatory system. At a histological level, it consists of several key structures, each with its own unique functions.

The *cardiomyocytes* are the primary contractile cells of the myocardium. They are elongated in shape and multinucleated, as they constitute the *functional syncytium* of the heart. The synchronized contraction of such syncytia is achieved through the presence of intercalated disks, specialized junctions that provide mechanical and electrical coupling between cells. Intercalated disks (Figure 1.4) are made up of gap junctions (detail of Figure 1.4), which allow for the transfer of electrical signals between cells, and desmosomes, which provide mechanical stability.

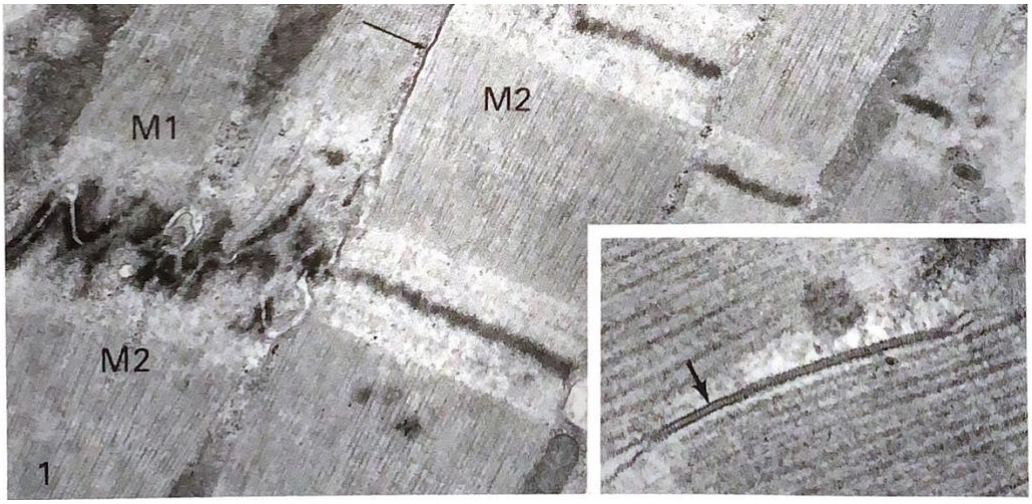

Figure 1.4 Transmission Electron Micrograph showing the myocardium ultrastructure. M1 and M2 represent two distinct myocytes connected by intercalated disks. Arrows indicate lateral gap junctions. Large micrograph is approximately 2 x 4 μm (h x w). Detail is approximately 500 x 800 nm. The pointed gap junction width is ~ 20 nm. Micrographs are sourced from Cell and Tissue Ultrastructure: A Functional Perspective (P.C. Cross, K.L. Mercer, 1995)

In addition to the myocytes, the myocardium also contains blood vessels, nerve fibers, and fibroblasts. **Blood vessels**, specifically the coronary arteries and veins, provide a rich blood supply to the myocardium, which is necessary to meet its high metabolic demands during contraction.

Fibroblasts, which are connective tissue cells, play a crucial role in maintaining the structure and integrity of the myocardium. These cells produce the extracellular matrix (ECM), which provides mechanical support to the tissue but needs to be finely controlled in its deposition, to avoid fibrotic imbalance.

1.2.2 The Myocytes' architecture

The cytoskeleton of a cardiomyocyte, i.e., its structural scaffold, plays a crucial role in linking the cell and its contractile machinery to the external environment. At certain focal points, cytoskeletal proteins like *α-actinin*, *talin*, and *desmin* interact with the intracellular domain of *integrins*, which can be viewed as molecular anchors holding the cytoskeleton itself to the external ECM.

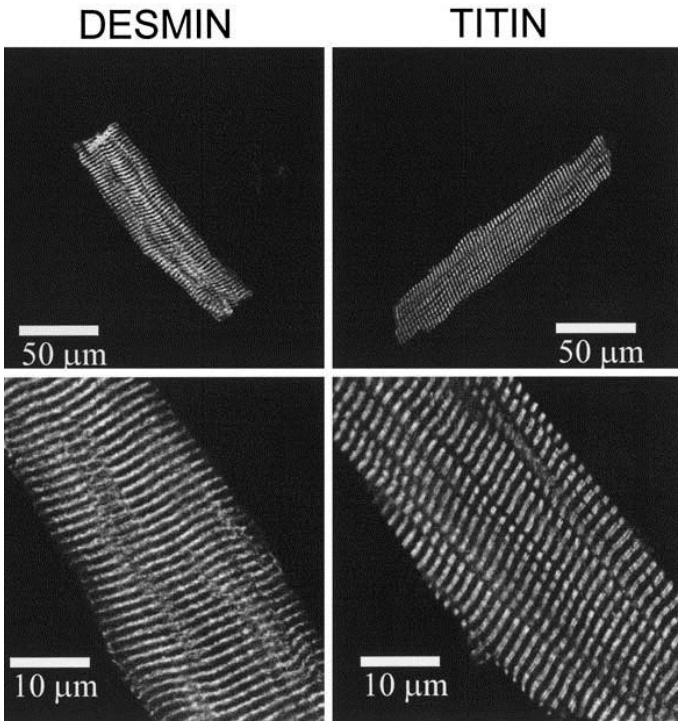

Figure 1.5. The cytoskeleton in myocytes is intricately structured and made up of several proteins that are involved in transmitting signals, maintaining cell shape, and guiding contractile element formation. This figure displays images of the cytoskeletal protein desmin (**left**) and titin (**right**) produced through immunofluorescent staining. Desmin is an intermediate filament that is found in myocyte Z-bands and helps align myofibrils. Its periodic presence within the myocytes can be easily seen under high magnification (**bottom left panel**). Titin, the largest cytoskeleton protein in myocytes, is crucial in maintaining sarcomere alignment, providing elasticity, and preventing excessive strain. Its doublet pattern, visible under high magnification (**bottom right panel**), can be seen at 100-nm intervals on either side of the Z-band. C.A. Walker and F.G. Spinale, 1999

Additionally, the large protein *titin* provides elasticity to the CM and helps protecting the myofilament from excessive strain. A representation of these proteins in a normal myocyte can be seen in the Figure X, depicting photomicrographs that were produced by immunofluorescent staining for desmin and titin.

1.2.3 The sarcomere

The sarcomere is the basic functional unit of the cardiomyocyte, containing its contractile proteins. It is made up of alternating thick and thin filaments, and has a length of 1.8 to 2.4 μm. The main components of the contractile apparatus are *myosin*, *actin*, *tropomyosin*, and the *troponin complex*.

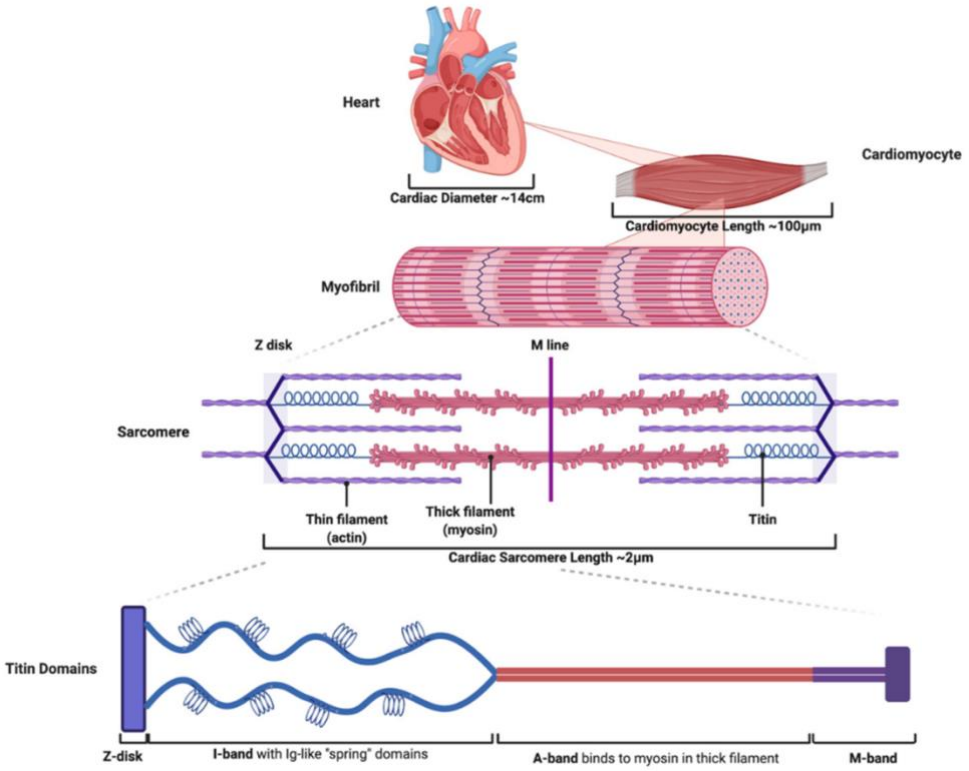

Figure 1.6. Titin is a vital part of the cardiomyocyte contractile function. It is found in the sarcomere of the myofibril, which makes up the cardiomyocyte. Titin has four structural domains, each serving specific functions. The N-terminal domain anchors titin to the Z-disk. The I-band holds Ig domains that add elasticity and give titin a spring-like quality. The A-band, where titin binds to myosin, acts as a stiff region during contraction. The C-terminal domain connects titin to the M-band. C. Tharp, 2022

When there's increased extracellular calcium, interactions between these proteins cause ATP hydrolysis and physiochemical changes, resulting in tension in the myocyte. Myosin, the thick filament, bears a filamentous tail and a globular head

region that houses the actin binding site and displays an ATPase activity. Actin, the major contractile protein in the thin filament, comes in two forms: G and F. F-actin forms the backbone of the thin filament and G-actin acts as a stabilizer. Each G-actin monomer has two myosin binding sites. Crossbridge formation and sarcomere shortening occur when myosin's globular head interacts with the G-actin monomer in the presence of ATP. Tropomyosin, also found in the thin filament, is a rigid molecule that adds rigidity to the thin filament by lying on either side of actin. It regulates actin-myosin crossbridge formation by interdigitating with the actin-myosin cleft and preventing calcium binding. The troponin complex, in the thin filament, consists of three proteins: troponin T, I, and C. It regulates crossbridge formation and contributes to the sarcomere's structural integrity. Troponin T binds the troponin complex to tropomyosin and anchors it to the thin filament. Under normal conditions, phosphorylated troponin I weakens calcium's affinity for troponin C. Calcium binding to troponin C leads to a conformational change in the complex and subsequent actin-myosin interaction, triggering crossbridge formation.

1.2.4 The Excitation-Contraction Coupling

EC coupling refers to the mechanism by which an incoming action potential and the resulting contraction of a myocyte occur. The key ion involved is calcium (Ca^{2+}). EC coupling begins by increasing the concentration of cytosolic Ca^{2+} from low nanomolar (100 nM) to high micromolar (10 μM) levels. Figure X illustrates key components of the EC coupling.

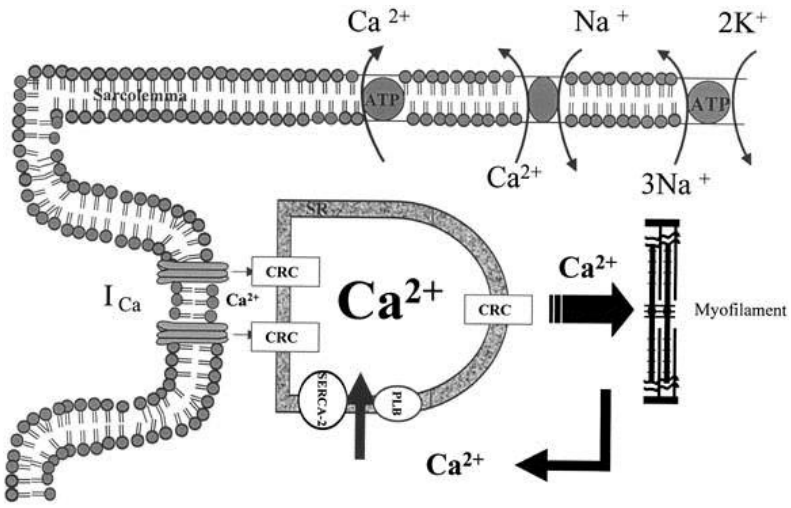

Figure 1.7. Schematics of the EC coupling. C.A. Walker and F.G. Spinale, 1999

The sarcolemma contains ion channels and pumps that regulate Ca^{2+} levels. The Na^{+}/Ca^{2+} exchanger and sarcolemmal Ca^{2+}-ATPase help to remove Ca^{2+} from the myocyte cytosol, while a Na^{+}/K ATPase helps maintain the resting membrane potential by extruding Na^{+}. Depolarization of the myocyte activates the L-type Ca^{2+} channel, leading to an influx of Ca^{2+} through ICA. This triggers the opening of the Ca^{2+} release channel (CRC) on the sarcoplasmic reticulum, releasing a large amount of Ca^{2+} *from the inside*. This leads to a dramatic increase in cytosolic Ca^{2+} resulting in crossbridge formation between actin and myosin. The SERCA-2, found on the sarcoplasmic reticulum, helps remove Ca^{2+} from the cytosol, allowing crossbridge disengagement and relaxation of the myofilaments.

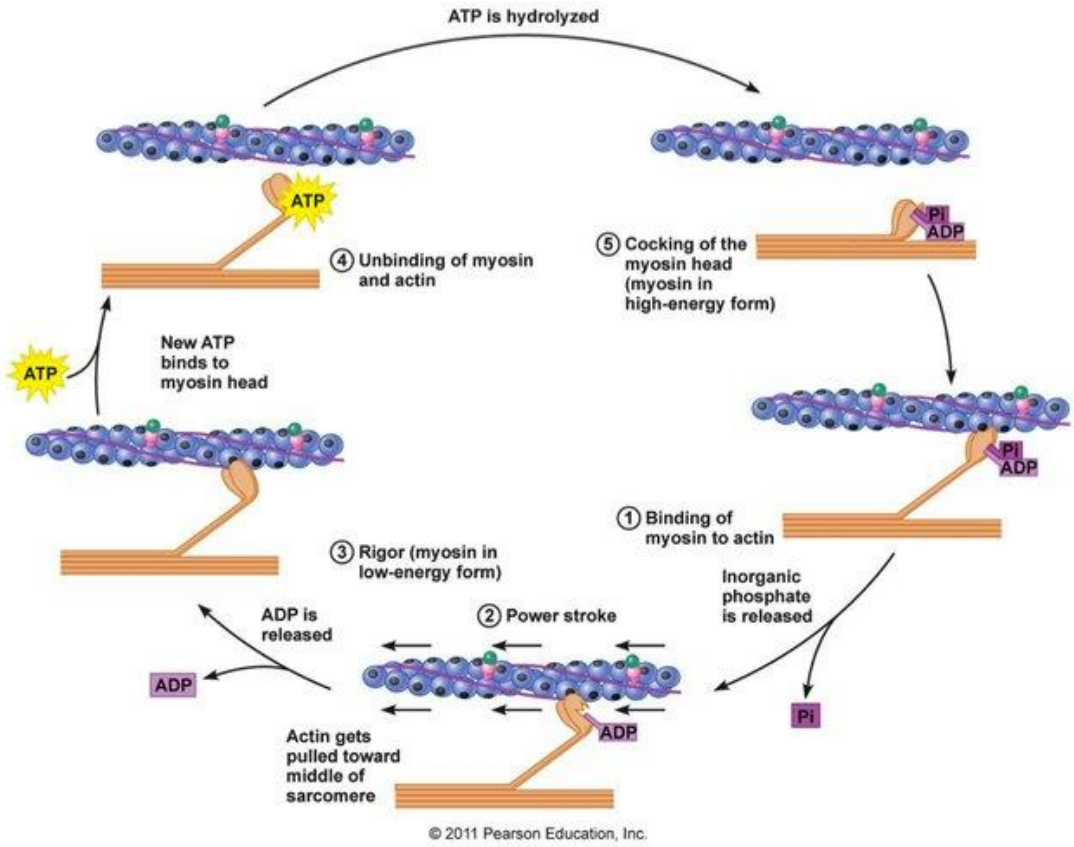

Figure 1.8. Scheme of the sarcomeres contraction cycle. K. Frei, 2013

The process of contraction in a cardiomyocyte is initiated by the arrival of an action potential, which triggers the opening of L-type Ca^{2+} channels in the sarcolemma and results in the influx of a small amount of Ca^{2+}. This small amount of Ca^{2+} acts as a

trigger and activates the release of a large amount of Ca^{2+} from the sarcoplasmic reticulum into the cytosol. The increase in cytosolic Ca^{2+} concentration causes a conformational change in the troponin-tropomyosin complex, which then unblocks the actin-myosin binding site, leading to crossbridge formation. This initiates a cycle of ATP hydrolysis, crossbridge formation and detachment, causing a thin filament shirt relative to the thick filament, resulting in the sarcomere contraction. The contraction length and speed are dependent on the number of crossbridges, action potential duration, Ca^{2+} release from the sarcoplasmic reticulum, and stored ATP molecules. The contraction continues until Ca^{2+} is removed from the cytoplasm, or until ATP stores are exhausted.

1.2.5 The action potential: electrical considerations

What has been described in the previous section is not the result of a *spontaneous* depolarization cycle, nor something initiated by nervous activity as it happens in the case of a skeletal muscle. Instead, it starts from a specialized group of cells known as *pacemaker cells*, that can spontaneously depolarize. In healthy hearts, these cells form the cardiac pacemaker and are primarily found in the SA node.

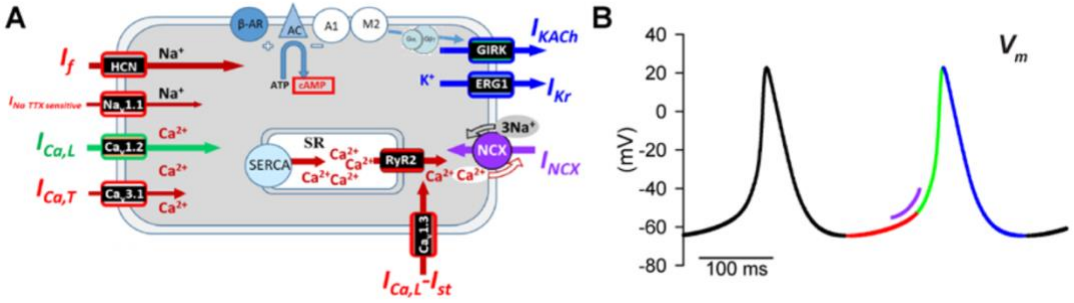

Figure 1.9. (A) Schematic of a SA pacemaker cell showing the main membrane bound receptors and ion channels together with RyR2, the SR calcium pump SERCA and the Na^+/Ca^{2+} exchanger (NCX1). **(B)** Simulated transmembrane potential (Vm) during a spontaneous action potential (AP) generated by a computational model of the mouse SAN myocyte, with color-code corresponding to the major AP phases [colors also indicate corresponding underlying currents in **(A)**]: Diastolic depolarization (red), AP upstroke (green), repolarization (blue). P. Mesirca, 2021

The first phase (i) of their spontaneous activity is the slow depolarization phase, which is initiated by the slow influx of Na^+ ions into the cell and the gradual decrease of K^+ permeability. This causes the inside membrane potential of the cell to become more

positive, which eventually reaches a threshold for generating an action potential. In pacemaker cells, this depolarization is called the "funny" or pacemaker current.

The second phase (ii) of the action potential is the rising phase, where there is a rapid influx of Ca^{2+} ions into the cell. This influx is driven by voltage-sensitive Ca^{2+} channels that open when the threshold is reached. The rising phase of the action potential results in the immediate reversal of the membrane potential, reaching a peak of about +10mV. It is important to note that in pacemaker cells, this phase is driven by the activation of L-type calcium channels, which are different from the voltage-gated fast Na^{+} channels that initiate action potentials in contractile cells. As a result, the pacemaker action potential rising phase is more gradual compared to a contractile cell.

The third and final phase (iii) of the cardiac action potential is the repolarization phase, where there is a rapid loss of K^{+} ions from the inside of the cell. This loss of potassium ions is driven by the opening of K^{+} *leak* channels. At the same time, Ca^{2+} channels are inactivated while, in addition, Na^{+} permeability is decreased. These changes in ion concentration and permeability cause the cell to repolarize, restoring the resting membrane potential (-60mV). After repolarization, ionic pumps work to restore the ion concentrations to their pre-action potential state. The Na^{+}-Ca^{2+} exchanger pumps Ca^{2+} outside, effectively relaxing the cell. The Na^{+}/K^{+} pump restores the ion concentrations of such ions. This ion restoration phase is crucial as it enables the cell to reset itself, allowing the pacemaker cell to start the process of spontaneous depolarization again.

1.2.6 Myocardial pathophysiology

In this section, an overview of the cellular and subcellular features of cardiac pathophysiology will be briefly introduced regarding the pathological conditions discussed in section 1.1.4.

1.2.6.1 Cardiomyopathies

We are herein focusing on the impairment of some cytoskeletal proteins that have been shown to relate to DCM, in order to provide a *general* example on the influence of such genetic mutations into the development of a diseased phenotype.

DCM is a complex disease characterized by genetic and phenotypic heterogeneity. So far, all of the identified DCM-related genes are expressed in cardiomyocytes and encode proteins that are involved in various metabolic or structural functions in cardiomyocytes.

One mechanism involves mutations in sarcomeric proteins, which are believed to cause a deficit in force production. These mutations could result in reduced actomyosin interaction or impaired ATP utilization, leading to decreased force production. Another mechanism could be a deficit in force transmission from cell to cell, caused by mutations in proteins involved in intermediate filament, cytoskeletal architecture, and sarcomere anchoring such as desmin, dystrophin-sarcoglycan complex, and metavinculin. These proteins play a role in the transduction of mechanical forces through the cellular architecture and to adjacent cells, and mutations in these genes could impair this process, leading to heart dilation.

Mutations in the LMNA gene, which encodes lamin A/C protein, have also been associated with DCM. This gene is organized as a network and is involved in membrane structure integrity and chromatin interaction. However, the underlying mechanisms for the cardiac or non-cardiac disorders resulting from LMNA mutations are still not well understood.

More recently, a role for calcium cycling regulation has been demonstrated in a family with a mutation in the phospholamban protein, a regulator of the sarcoplasmic endoplasmic reticulum calcium ATPase (SERCA)2a calcium pump of the endoplasmic reticulum. The mutation results in chronic inhibition of SERCA function, leading to depressed contractility and, ultimately, heart dilation.

Nevertheless, the most prevalent mutations leading to a cardiomyopathic phenotype are the ones affecting Titin, which is the largest protein known of our body. Modifications in the expression of different titin isoforms have been linked to systolic and diastolic heart failure.

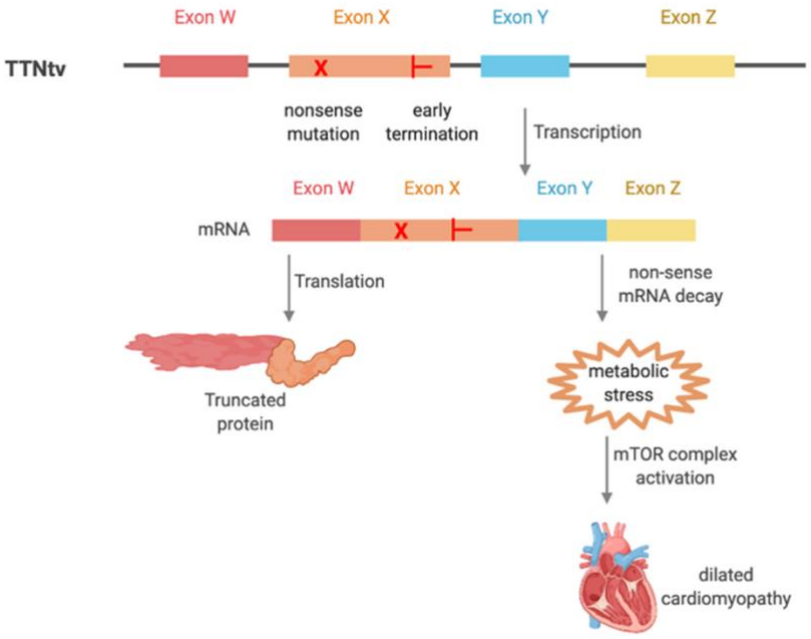

Figure 1.10. Titin truncation variations (TTNtv) leads to dilated cardiomyopathy because of haploinsufficiency and heightened metabolic stress. The non-sense mRNA decay caused by TTNtv triggers increased metabolic stress and activates the mTOR signaling pathway, which ultimately contributes to the development of dilated cardiomyopathy because of this downstream cascade. Tharp et al., 2020

Titin Ig-like domains give the cardiac tissues important properties such as length dependent activation and passive tension of the ventricle. Mutations in the titin gene are the most common genetic cause of DHC. Truncation mutations in the titin gene lead to increased intracellular stress and activate the mTOR signaling cascade. This results in abnormalities in cellular metabolism, leading to cardiomyocyte dysfunction. Additionally, factors such as age, chemotherapy, alcohol use, and pregnancy can further increase the risk of developing DHM in individuals with such mutations.

There are potential therapies being developed to treat such truncations, including mTOR inhibitors and oligonucleotides that lead to alternative splicing and exclusion of mutated exons. Increasing the expression of the shorter, stiffer N2B isoform may

improve systolic heart failure, while favoring the longer, softer titin isoform may improve diastolic dysfunction.

1.2.6.2 MI and MF at the cellular scale

The heart's ECM is formed by a variety of proteins, including collagen and elastin, which are the most prominent structural polypeptides of this organ [x]. In particular, the heart collagen network's main components are type-1 collagen (Col 1, accounting for the 80-85% of the total collagen content) and type-III collagen (Col III, around 10%). Moreover, a gel-like network of proteoglycans provides hydration and swelling pressure, enabling the tissue to withstand its compressional forces [x]. All these proteins uphold the shape and integrity of the heart during its contraction cycles and their balance is therefore essential to keep the cardiovascular system in its optimal shape.

Indeed, many pathological conditions, such as hypertensive cardiac disease, idiopathic dilated cardiomyopathy, and coronary artery disease, lead to extensive myocardial injury. This process is sustained by necrotic cardiomyocytes who release, among other pro-inflammatory molecules, damage-associated signals as high motility group box 1 (HMGB1) [x]. Resident macrophages who recognize such signals begin secreting pro-inflammatory cytokines, such as the tumor necrosis factor alpha (TNF-α). Consequently, resident fibroblasts are activated by TNF-α signaling [x] and start transitioning to a myofibroblast (myoFb) phenotype, i.e., a fibroblast possessing the contractile machinery typical of a smooth muscle cell [x]. In turn, myoFbs secrete TNF-α (and other cytokines) by themselves, thus initiating an inflammatory positive feedback loop [x]. After the initial inflammatory phase, followed by a proliferative one, myoFbs eventually enter a reparative phase [x]. At this stage, they secrete new collagen fibers, particularly Col 1, altering the Col1/Col III balance ratio in the heart. Nevertheless, scar formation is a physiological process per se, as it offers a protective environment for wound healing, at least initially. However, as cardiomyocytes are terminally differentiated cells [x], they hold limited regenerative capabilities [x].

Therefore, such scar is never replaced by a functional contractile tissue. Instead, this pathological remodeling leads to myocardial fibrosis (MF).

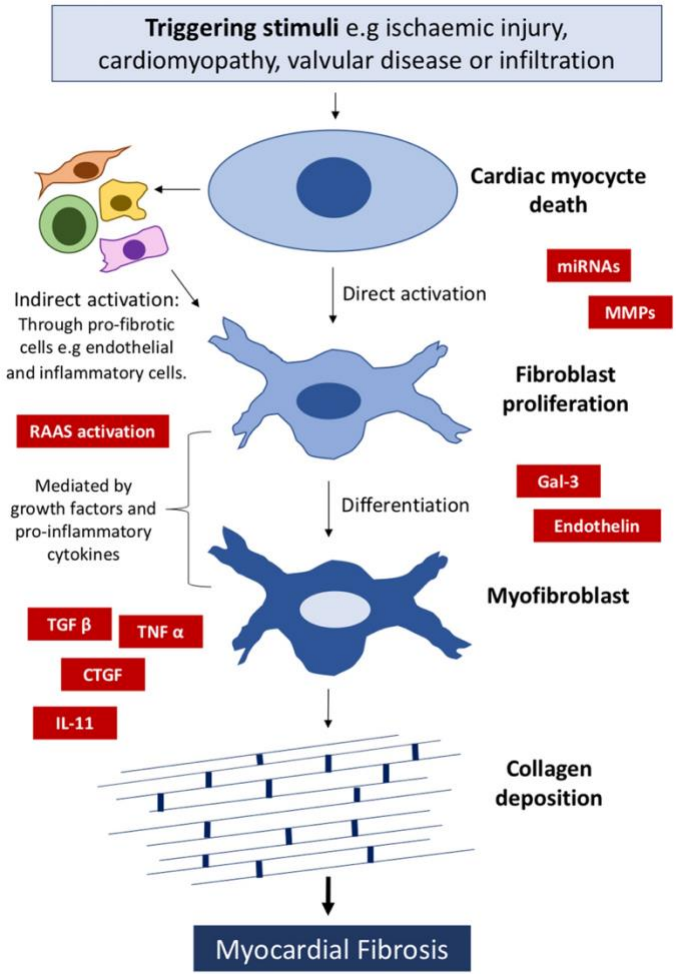

Figure 1.11. Schema depicting myocardial fibrosis progression and potential therapeutic target sites of action. The following are abbreviated: RAAS (renin–angiotensin–aldosterone system), TGFβ (tissue growth factor-β), TNFα (tumour necrosis factor-α), CTGF (connective tissue growth factor), IL-11 (interleukin-11), miRNA (microRNA), MMP (matrix metalloproteinases), Gal-3 (galectin-3). M. Webber et al. 2020

MF is defined as an abnormal buildup of ECM in the heart muscle [x]. As the excessive collagen builds up, its bundles isolate the cardiomyocytes within the tissue, selectively reducing side-to-side gap junctions in-between. This impairs transverse electrical propagation between myocytes, leading to spatial wave decoupling, ultimately promoting heart arrhythmia [x]. Besides, MF causes gap junctions at the intercalated disks to be – if not completely lost – redistributed along the myocytes' sides. This lateralization further reduces the longitudinal (i.e., along the major axis of the same

fiber) conduction velocity [x], further compromising the native heart's electrophysiology.

Mechanically, MF causes myocardial stiffening [x] and a reduction of heart elasticity [x], affecting its ability to contract and relax, ultimately leading to ventricular dysfunction [x]. Over time, the heart's pumping efficiency becomes less effective. Hence, MF represents the structural correlate of heart failure, which is globally the leading cause of hospitalization in people older than 65 [x].

Chapter 2

Exploring cardiac cell functionality using nanotechnological methods

2.1 Models to study cardiac mechanics *in vitro*

In this section, a *brief* introduction on some available in-vitro models to study the cardiomyocyte mechanobiology will be provided as examples, emphasizing on those methods that clearly benefited from the application of nanotechnological tools.

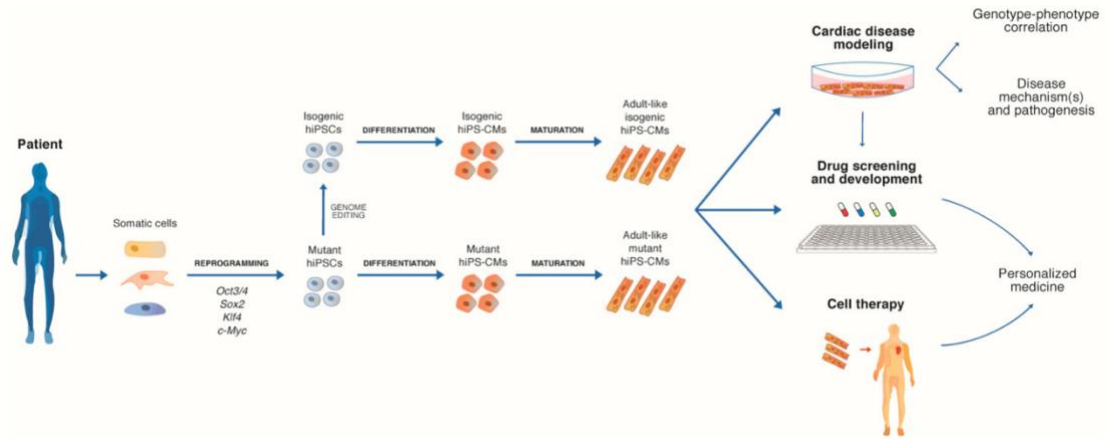

Figure 2.1. Generation of hiPS-CMs from patient-derived human induced pluripotent stem cells, involves three main steps: reprogramming of somatic cells to hiPSCs, differentiation to hiPSC-derived CMs, and maturation to obtain "adult-like" hiPS-CMs. These cells are used in research and clinical applications. Sacchetto et al., 2020

iPSCs are a type of pluripotent stem cells generated from the reprogramming of adult cells into an embryonic stem cell-like state. These cells can be differentiated into various cell types, including cardiomyocytes, opening to various applications in the fields of disease modeling, drug screening, and regenerative medicine. The key advantage of this technology relies in the potential usage of patient-specific cells, reducing the risk of immune rejection in the case of tissue reimplantation. However, current iPSC-CM generation methods require improved efficiency and functional maturation, as iPSC-CMs still display a high degree of immaturity, as well as requiring finely tuned and sensitive culture conditions.

On the other hand, Neonatal Rat Ventricular Myocytes (NRVMs), derived from P0-3 neonatal rat hearts, have several advantages such as their robustness and ease of culture. NRVMs exhibit a number of physiological and electrophysiological characteristics that are similar to those of adult cardiomyocytes, including action potential duration and calcium handling. Therefore, they represent a valuable model

for studying cellular mechanisms underlying normal and abnormal heart function, as well as for evaluating the efficacy and safety of potential new drugs.

Despite their advantages, NRVMs are limited in their ability to fully recapitulate the complexity of the human heart, and it is important to be aware of these limitations when interpreting results obtained from related experiment. Nonetheless, they remain a widely used and valuable model in cardiovascular research.

2.2 Bi-dimensional and 2.5D cardiac constructs

In 2D cultures, cardiac cells are forced to adhere on a flat surface, typically in a plastic dish. This simple strategy allows an easy manipulation and observation of the cells and is used to study a range of biological processes, including differentiation and gene expression. However, 2D cultures are a poor representation of a native myocardium because, as in the case of most tissues, myocardial cells thrive in 3D.

Nevertheless, it should be noted that by tuning the geometrical features of 2D surfaces, *specific* cell-substrate interactions can be successfully driven to investigate the CM mechanosensing pathways.

Accordingly, we refer to 2.5D surfaces as to a surface which has been modified to pattern sub-micrometric features, thus promoting a certain CMs alignment, interconnectivity, differentiation, and more.

Carson et al. [x] presented a nanogrid culture array made up of nanogrooved topographies with groove widths ranging from 350 to 2000 nm. This array was used to examine the impact of different nanoscale structures on the structural development of iPSC-CMs in vitro. The nanotopographies were designed to mimic the oriented myocardial extracellular matrix fibers found in vivo and were integrated with a self-assembling chimeric peptide that contained the Arg-Gly-Asp (RTG) cell adhesion motif. The organization and structural development of the cardiomyocytes were dependent on the nanotopographical feature size in a biphasic manner, with the best results achieved on grooves in the 700–1000 nm range. These findings demonstrated the ability of surface-functionalized, bioinspired substrates to influence

cardiomyocyte development and the versatility of such platforms for investigating the role of topographical guidance cues on cell behavior.

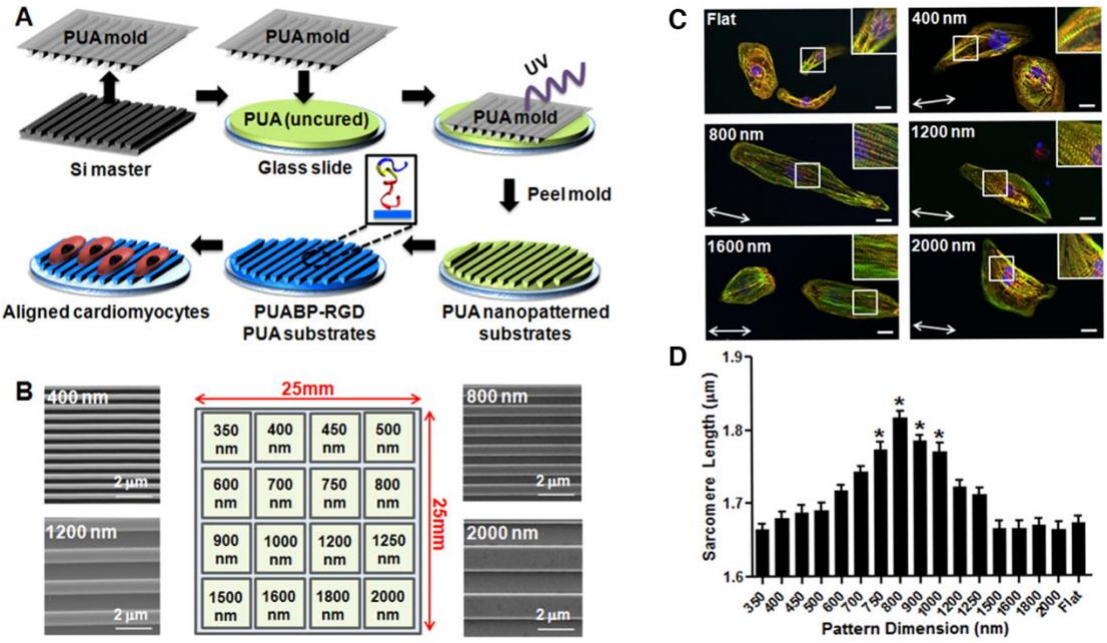

Figure 2.2. A, scheme of the nanofabrication workflow followed by the authors. B, cell culture array disposition. C and D, biphasic sarcomere alignment behavior following the underlying topography. Carson et al., 2016

In a similar study, pioneered using NRVMs, Deok-Ho et al. designed a unique cell substratum based on their observation that the extracellular matrix underlying the aligned cell arrays in the native myocardium is present in the form of aligned fibers parallel to the direction of cell alignment. They fabricated biocompatible PEG-based substrata with precisely controlled nanoscale topography, which allowed for electrophysiological analysis and biochemical tests. The substrata caused neonatal NRVMs to form highly anisotropic cell arrays, guided by the direction of the underlying nanoridges. The group discovered that the difference in the cell-substratum interface might place distinct spatial constraints on cellular organization, leading to a relative increase of cell spreading on the same. The relative increase in cell spreading can enhance cell-cell coupling and lead to an optimal topography for cell-cell coupling, which maximizes the area of cell-substratum contact. The mechanism

emphasized the importance of the degree of separation between individual ridges, which mimics the variable local separation between individual extracellular matrix fibrils.

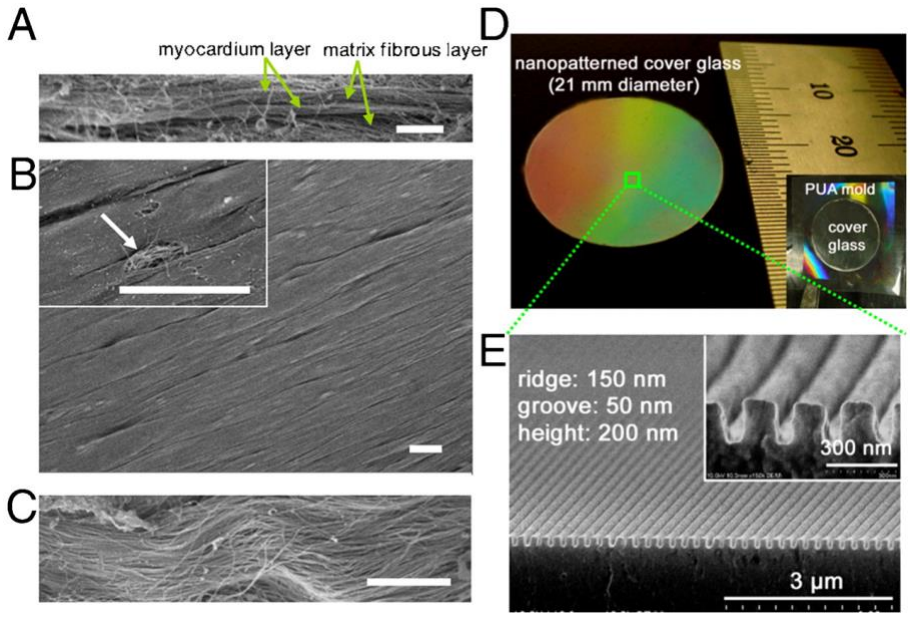

Figure 2.3. Design and fabrication of nanopatterned substratum of PEG hydrogels. (**A–C**) SEM images of ex vivo myocardium of adult rat heart. Side view (**A**) and top view (**B**) show well-aligned myocardium. The Inset in (**B**) and the magnified view in (**C**) demonstrate that the structural organization of the myocardium correlates with matrix fibers aligned in parallel beneath. (**D**) Photograph of a large-area (~3.5 cm^2) substrate on a glass coverslip. (**E**) Cross-sectional SEM image of the patterned substrate. [Scale bar: 5 μm in (**A**); 10 μm in (**B**) and (**C**).] Deok-Ho et at., 2009

Apart from geometrical features, it should also be noted that the *mechanical* properties of the underlying substrate play a fundamental role in the functional maturation of cardiomyocytes. In a pioneering work, Jacot et al. [x] plated NRVMs on polyacrylamide gels varying in the elastic moduli. Their results showed that cells grown on 10 kPa substrates had aligned sarcomeres, while those grown on stiffer substrates displayed unaligned sarcomeres and stress fibers. The cells twitched with greater mechanical force on 10 kPa gels compared to either stiffer or softer substrates. Moreover, NRVMs grown on physiological (10 kPa) gels showed the largest calcium transients and had the highest expression of sarcoplasmic/endoplasmic reticular calcium ATPase2a. They eventually found that deviations from ideal extracellular stiffness led to lower expression of sarcoplasmic/endoplasmic reticular calcium

ATPase, reduced stored calcium, smaller calcium transients, and lower force generation.

2.2.1 3D cardiac constructs

3D in-vitro cardiac structures are booming nowadays, as countless of attempts are being made towards the fabrication of a fully functional heart to eventually replace the diseased one. While such goal is far from being reached, novel technologies like 3D bioprinting are constantly pushing the boundaries of such progress, creating more and more physiological-like *organoids*.

The field of 3D cultures is a rather complex one, as many parallel strategies are being pursued together to reach the aforementioned goal. However, some preliminary classification can be introduced by discerning between scaffold-free and scaffold-based methods.

2.2.1.1 Scaffold-free cultures

The simplest type of a 3D auto-assembled culture is the multicellular spheroid. Originally introduced to study the tumor microenvironment, it has been recently shown to mimic important features of the heart microenvironment as well. Cardiac spheroids are easily built by the hanging-drop method, or through more advanced incubation vessels such as Ultra-Low Attachment (ULA) microplates. In either case, a dense cell suspension is allowed to settle over the course of 4-5 days inside a spherical-shaped meniscus, which allows for the cells to aggregate altogether. Moreover, multiple cell phenotypes can be aggregated together, promoting supportive ECM formation as well as endothelial vascularization. Cardiac spheroids show an improved physiology compared to standard 2D cultures and are currently being exploited as a bio-ink to print arbitrary 3D structures.

A new method for delivering stem cells using 3D bioprinted cardiac patches without biomaterials has been developed by Chin et al.

Such method involves aggregating iPSC-CMs, fibroblasts, and endothelial cells, to create mixed cell spheroids in various cell ratios. Then, the spheroids were loaded inside a 3D bioprinter and used to print cardiac patches. Cardiac patches were evaluated using various techniques such as light and video microscopy,

immunohistochemistry, immunofluorescence, cell viability assays, and electrical mapping.

The results showed that all the cardiac patches beat spontaneously after 3D bioprinting, exhibiting ventricular-like action potential waveforms and uniform electrical conduction. Furthermore, the conduction velocities were higher and the action potential durations were significantly longer in the patches with a lower percentage of FBs (15%). Immunohistochemistry showed that rudimentary CD31+ blood vessel formation was ongoing. Immunofluorescence showed an abundant distribution of Cx43, the primary cardiac gap junction protein, localized to cell-cell borders. Finally, the patches were implanted into a rat heart, showing successful engrafting with the hosting tissue.

To improve single spheroid maturation from the electrical physiology perspective, Yu et al. reported on the use of electrically conductive silicon nanowires (e-SiNWs) to enhance the maturation of cardiac spheroids. They incorporated trace amounts of e-SiNWs into both NRVMs and hiPSC-CM cardiac spheroids, creating electrically conducting microenvironments.

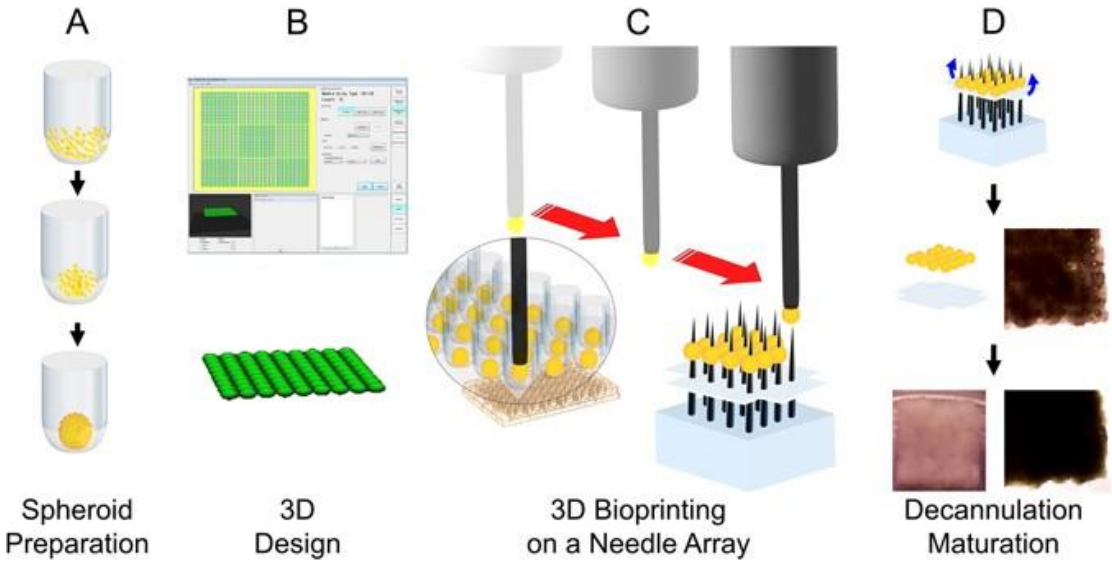

Figure 2.4. Schematic overview of biomaterial-free cardiac 3D bioprinting process. (**A**) Cells (CMs, FBs, ECs) are aggregated in ultra-low attachment 96-well plates to form cardiospheres. (**B**) The desired 3D structure to be bioprinted is designed using computer software. (**C**) The 3D bioprinter picks up individual cardiospheres using vacuum suction and loads them onto a needle array. (**D**) Cardiospheres are allowed to fuse. The 3D bioprinted cardiac tissue is then removed from the needle array, and cultured further to allow the needle holes to be filled in by surrounding tissue. Chin et al., 2017

The results showed that the e-SiNWs induced synchronized and enhanced contraction, promoting structural and contractile maturation. This was evidenced by improvements in contraction amplitude, contractile protein expression, and assembly over a 3-week culture period. However, further maturation of the hiPSC-derived cardiomyocytes was not observed.

This study demonstrated the use of silicon-based nanomaterials without involving conventional scaffolding materials like polymers and hydrogels, highlighting the potential for e-SiNWs to have a major impact in the treatment of arrhythmia caused by unsynchronized contractions.

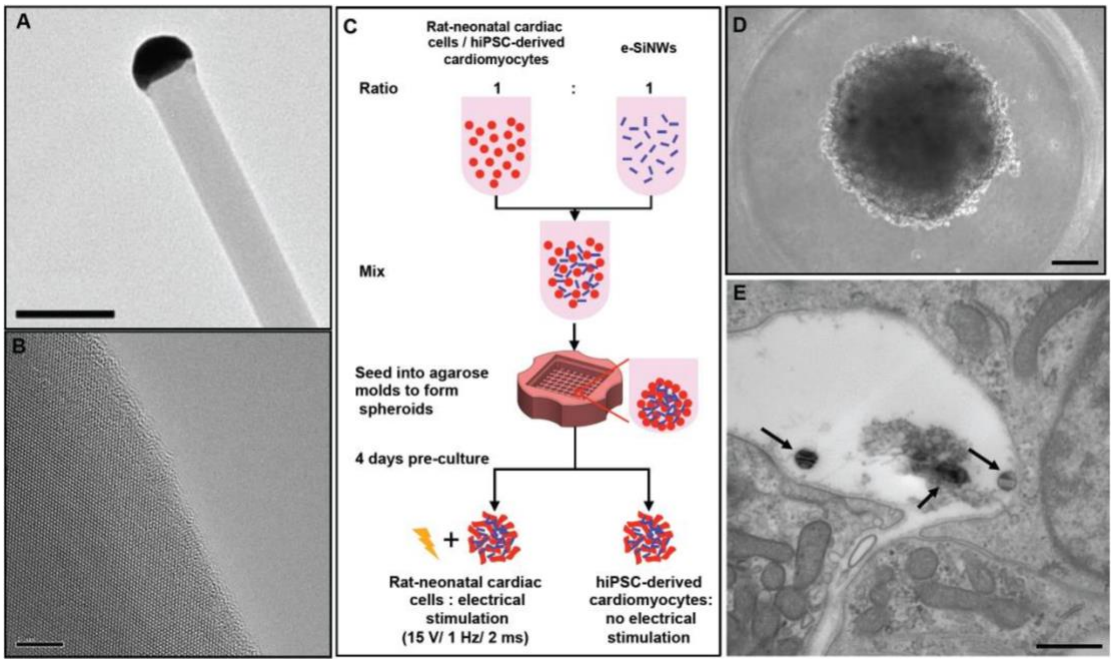

Figure 2.5. (A) TEM image of an e-SiNW (diameter ≈ 100 nm; length ≈ 10 μm) and **(B)** high-resolution TEM image of the e-SiNW. **(C)** Schematic representation of spheroid fabrication using NRVMs or iPSC-CMs at a ratio 1:1 (number of cells/number of e-SiNWs) with or without electrical stimulation. **(D)** Bright field image of iPSC spheroid with e-SiNWs. **(E)** TEM image of iPSC spheroid with e-SiNWs, black arrow indicates the e-SiNWs located in the extracellular area. Scale bars: **(A)** = 0.2 μm; **(B)** = 5 nm; **(D)** = 100 μm; **(E)** = 500nm. Yu et al., 2015

2.2.1.2 Scaffold-based cultures

The use of polymer-based scaffolds, particularly hydrogel-based ones, is very promising as it allows to provide a nurturing mechanical environment for cardiac myocytes to grow in. Moreover, such scaffolds are easily functionable with many chemical groups enabling to covalently bond electrifying nanomaterials such as

carbon nanotubes or gold nanoparticles, allowing action potentials to shortcut between cells, thus enhancing their electromechanical coupling.

In a recent work, Martinelli et al. aimed to investigate the impact of an elastomeric 3D scaffold made of polydimethylsiloxane (PDMS) with micrometric cavities and integrated multi-wall carbon nanotubes (MWCNTs) on NRVMs. By combinating fluorescence microscopy, cell biology, and calcium imaging they compared the viability and maturity of NRVMs cultured on the 3D-PDMS+MWCNT scaffold versus the 3D PDMS control. NRVMs cultured on the electroactive scaffold showed improved viability and a more defined and mature sarcomeric phenotype compared to the control, with an increase in connexin-43 gene expression, gap junction areas, and enhanced electrophysiology. Additionally, the scaffold was found to boost NRVM proliferation while hindering cardiac fibroblast expansion compared to the control PDMS.

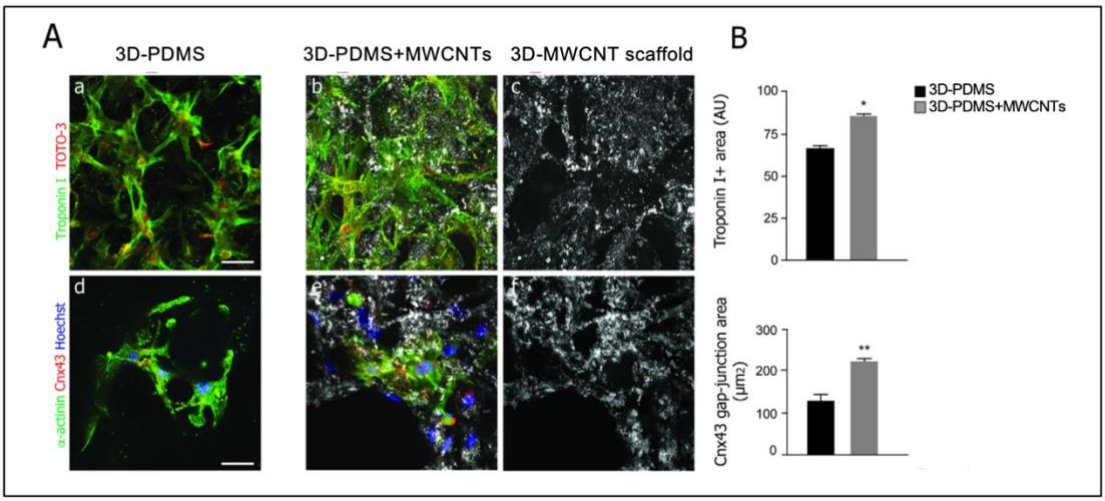

Figure 2.6. Phenotype of 3D grown cardiomyocytes seeded on 3D-PDMS (control) and the electroactive scaffold. **A, upper panel**: IF images of Troponin-I and TOTO-3 showing a more defined CM phenotipe on 3D-PDMS-CNTs scaffolds. **A, lower panel**: Connexin-43 (red dots), sarcomeric-alpha-actinin (green), and TOTO-3 (nuclei, blue) staining, revealed an increase in Cx-43 distribution on 3D-PDMS+MWCNTs, much more homogeneously distributed with a significative high number of cell-junctions. Martinelli et al., 2018

These findings offered new perspectives for the development of innovative therapies for cardiac repair in cardiac tissue engineering.

In another study, Pena et al. developed novel Reverse Thermal Gels (RTGs) that were designed to have a water-like viscosity at RT, while transitioning to a gel-state above 32-35 °C. Such RTGs were later functionalized with either CNTs, or gold nanoparticles

(AuNPs), and both CNT-RTGs and AuNP-RTGs demonstrated superior performance in supporting the growth and maturation of NRVMs grown into them.

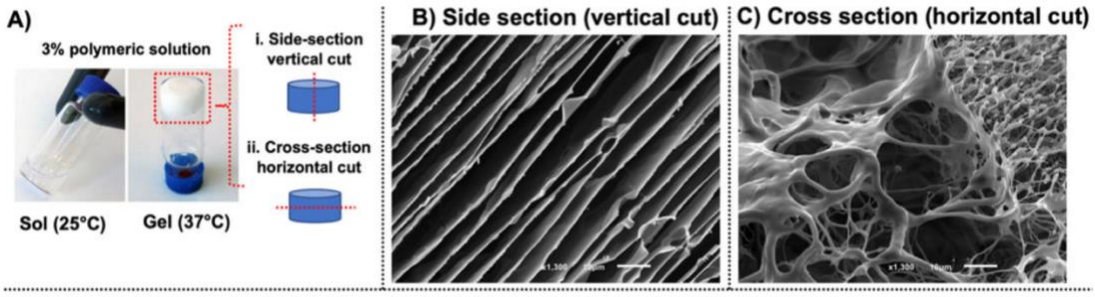

Figure 2.7. (A) Morphological characterization of the RTG–AuNPs was analyzed in vertical and horizontal cuts. **(B)** Vertical cuts of the hydrogel demonstrate a laminar sheet-like configuration. **(C)** Horizontal cuts of the hydrogel showed a highly interconnected porosity. Pena et al., 2017

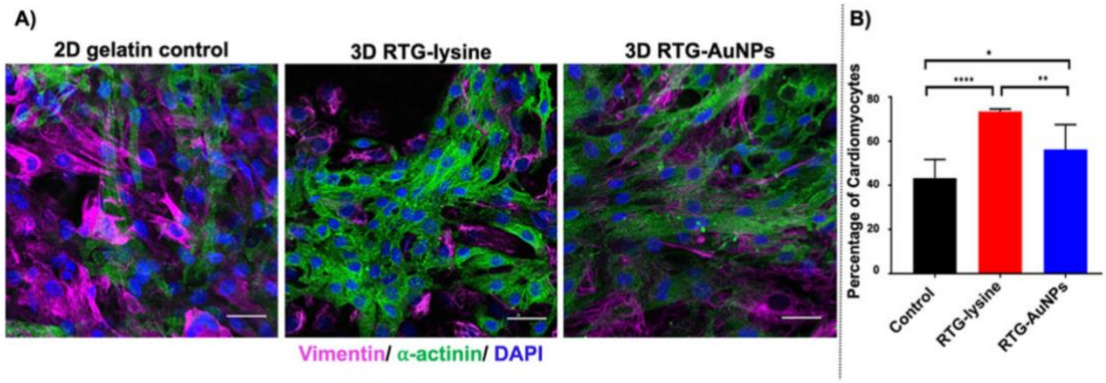

Figure 2.8. Immunocytochemistry labeling of NRVMs and CFs cultured in 2D and 3D systems for 21 days. **(A)** Antibody staining against α-actinin (green) and vimentin (pink) label NRVMs and CFs, respectively, with nuclei labeled using DAPI (blue). **(B)** Quantification of immunocytochemistry staining against α-actinin indicates the percentage of cells likely to be NRVMs, showing both 3D systems to contain a greater percentage of NRVMs than the 2D gelatin control. Scale bar 40 μm. Pena et al., 2017

Such gels were designed to be highly translational in the framework of clinical practice, as they can be injected in a MI site with a syringe, thanks to their low viscosity, with the goal of supporting cardiac regeneration *in situ*.

RTGs will be discussed in detail in Chapter 6, as they represent the scaffold used to induce a passive electromechanical conditioning of 3D cardiac spheroids probed by whole-spheroid AFM.

2.3 Mechanical properties of cells

Countless physical models have been proposed to gauge the mechanical complexity of cells. These models often share a common concept, which tells a cell can be represented as a continuous mass that reacts to external stimuli by exhibiting different types of mechanical behavior. These include *plasticity* and *viscoelasticity*.

A plastic material is permanently deformed after an applied load is removed. Most of cells in physiological conditions constantly adapt to internal or external stimuli by displaying a high degree of adaptation. However, these are not representations of a plastic behavior *per se*, being active responses driven by a chain of mechanotransduction events. Indeed, the key mechanical behavior to consider here is viscoelasticity.

2.3.1 Cell stiffness and elasticity

When an elastic object with a certain dimension L_0 is deformed with a certain force F, acting on the same direction as L, it will deform its dimension by $\delta = L_1 - L_0$. According to Hooke's law:

$$F \propto \delta$$

i.e, the force acting on such object is directly proportional to its extension. The factor of such proportionality is defined as:

$$k = \frac{F}{\delta}$$

Therefore, stiffness (k) is the extent to which an object withstands a deformation in response to an applied load: the higher the k, the less the object will deform to such load, and vice-versa. While being very simple, this relationship has been attracting remarkable interest in the field of cellular biomechanics, particularly in the study of cancer. Indeed, increased ECM stiffness is a classic hallmark of solid tumors [x]. A stiffer matrix drives cancer cells, through mechanosensing, to undergo epithelial-to-mesenchymal transition (EMT), hence promoting dissemination (i.e., metastasis). Therefore, cellular stiffness has been recently proposed as a possible diagnostic and prognostic mechanical marker, for various types of tumors. However, if we were able to act what has been fictionally depicted in Richard Fleischer's *Fantastic Voyage*, thus

becoming a microscopic-sized human inside a person's body, pressing a cell with a definite force to derive its k would be a poorly planned experiment. The reason does not rely in the infeasibility of such shrinkage – as our imagination allows it – rather because different cells can have different size and geometries while being made of a very similar material. When two objects made of a similar material, but different volumes, are pressed with an equal amount of force, the tinier one will deform greatly. Hence, if we were interested in discriminating two cells based on the properties of the *material* per se, we must account for the geometrical implications of the applied force. *Stress* (σ) is the measure of force per unit area:

$$\sigma = \frac{F}{A}$$

The greater this force and the smaller the cross-sectional area of the object – with respect to the applied force's direction – the greater the stress will be.

By normalizing the induced extension by the object's initial length, we further indulge in the concept of *strain* (ε), which is defined as:

$$\varepsilon = \frac{\delta}{L_0}$$

The relationship between the applied stress and the resulting strain is the relationship we were looking for, and it is defined as:

$$E = \frac{\sigma}{\varepsilon}$$

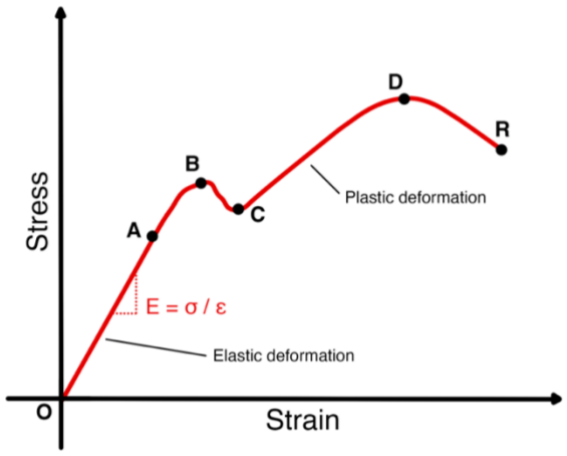

Figure 2.9. Stress-strain diagram for ductile materials, highlighting the proportional limit (O-A), the elastic limit (O-B), upper yield point (B), lower yield point (C), ultimate tensile strength (D), and breaking strength (R).

2.3.2 Measuring cellular elasticity

The ratio between stress and strain within the proportional limit of the stress-strain curve is defined as *Young's Modulus* of elasticity, and it is one of the simplest yet commonly used quantitative parameters to depict the elasticity of a cell experiencing uniaxial strain. Cell elasticity can be measured using different techniques such as Micropipette Aspiration, Brillouin microscopy, Optical Tweezers, Atomic Force Microscopy, and many others.

Micropipette aspiration is a popular method consisting in the application of a gentle suction to the cell membrane through a hollow micropipette. A portion of the cell is sucked into the capillary, and the ratio between the calculated stress and given strain leads to the Young's modulus of that cell portion (Figure 2.10-A). One of the main issues related to this technique is related to its resolution, being it unable to detect possible heterogeneities in Young's moduli distribution within the nanometric scale on the cell membrane.

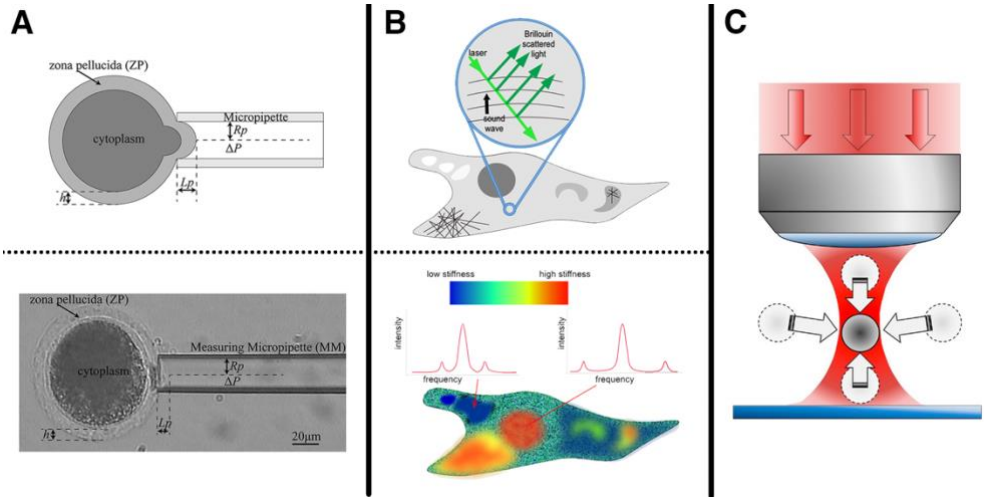

Figure 2.10. Panel (A-top) Diagram of a micropipette aspiration-based approach to estimate the Young's modulus of an egg cell. (**A-bottom panel**) Micropipette aspiration of a porcine oocyte. **Panel (B-top)** Liu et al. 2019. **Panel (B)** Principle of Brillouin microscopy. Laser light is scattered by thermally generated acoustic waves and undergoes a frequency shift **(top)**. The high shift corresponds to a large longitudinal modulus of the probed volume, which can be interpreted as being 'stiffer' **(bottom).** Prevedel Lab., EMBL Heidelberg. **Panel (C).** Drawing of a focused optical tweezer laser trapping a microsphere. A.Blázquez-Castro, 2019

Brillouin microscopy is an emerging tool in mechanobiology. The technique is based on the Brillouin scattering principle (Figure 2.10 B-top), which is the frequency shift of

light scattered by a material when such material is under stress. By measuring the Brillouin shift, the elastic properties of the sample can be determined (Figure 2.10 B-bottom). One of the key advantages of Brillouin microscopy is its high sensitivity and spatiotemporal resolution, which allows for the measurement of mechanical properties at the cellular and subcellular level in real-time, both at cell surface and below.

In **Optical tweezers**, a micrometric-sized bead is placed in contact with the sample surface. The bead is focused by a laser beam, creating an optical trap (Figure 2.10-C). The trapped bead is used to apply a controlled force to the sample, which can be done by moving by tuning the laser beam intensity itself. The position of the trapped bead or particle is measured using a position-sensitive detector to determine the displacement of the bead caused by the applied force. The Young's modulus is calculated by dividing stress by strain, as usual. To obtain a complete stress-strain curve, the above steps can be repeated for different forces, and the resulting Young's moduli are plotted against the corresponding strains.

One of the most widespread tools that has vastly been employed to study the cellular and subcellular mechanics is the **Atomic Force Microscope** (AFM). Its key advantage relies on the tremendous versatility and unmatched range of forces, from 5 pN – the breakage of a single hydrogen bond – up to several micronewtons. The AFM is considered a gold standard in the field of mechanobiology [x], not only as a force *measuring* tool, but especially as a force *modulating* tool, as it allows to apply a specific stress (or a specific strain) to stimulate a cell-specific behavior, while observing such biological response by matching complementary techniques such as *calcium imaging*, *patch-clamp*, and more.

2.4 Atomic Force Microscopy

2.4.1 Introduction to SPM and feedbacks

The AFM belong to the greater field of *Scanning Probe Microscopic* techniques (SPM), where the sample is physically scanned to obtain a surface reconstruction down to a *true* atomic resolution in all three dimensions.

The SPM field was founded by Gerd Binning and Heinrich Rohrer with the invention of *Scanning tunnelling microscopy* (STM) in 1981 [x], for which they shared half of the Nobel Prize in Physics five years later, together with Ernst Ruska for his work on electron optics.

In SPM imaging, surfaces are raster-scanned by a sharp tip, recording a value corresponding to a certain tip-sample interaction at discrete points, defined by the operator and by the lateral resolution of the employed *piezoelectric actuators*. Such recorded value depends on the type of SPM and method of operation. For example, in STM, a conductive tip is brought very close to a conductive surface, down to 4-7 Å. A voltage bias is applied between the two, allowing electrons to tunnel through the potential barrier generated in-between. The resulting tunneling current (I_T) is a function of the tip-sample distance (d/d_0) and decays exponentially with it:

$$I_{T(z)} \propto I_0 \cdot e^{\frac{-d}{d_0}}$$

The keystone of all SPM techniques is the implementation of a feedback loop in the Z direction which tracks and tunes the tip-sample interaction.

For example, in the *constant current mode* operational mode of STM, the tunneling current constitutes the process variable fed to the feedback and confronted with a user-setpoint. When the scanning probe encounters an asperity, the tunneling current changes and the error signal becomes non-zero. Consequently, the tip is extended or retracted to take back the current to value dictated by the setpoint.

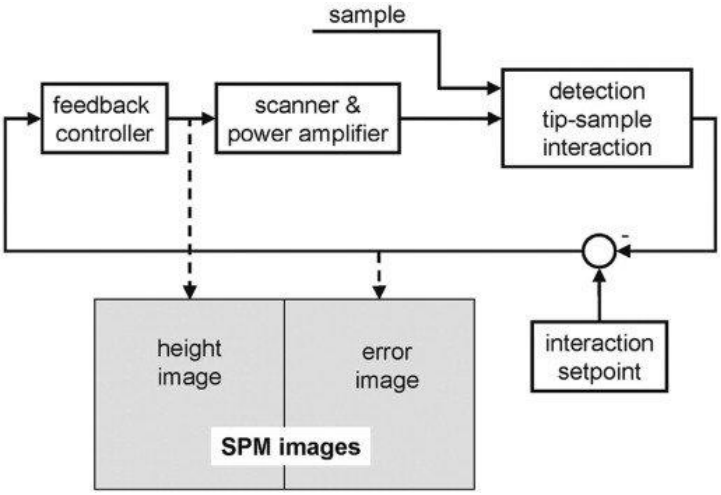

Figure 2.11. SPM feedback loop to track the tip–sample interaction in the Z-direction (height). A proper feedback control implies as much information as possible in the height image with as little as possible in the error image. (G. Schitter., 2008)

2.4.2 The AFM machine

In the Atomic Force Microscope (AFM) the tip is not necessarily conductive, nor it is the sample, and the tip itself hangs from a flexible cantilever behaving like a nearly ideal spring.

The first type of interaction used to investigate a surface with the AFM was atom-atom repulsion (hence the name), but other forces such as electromagnetic, mechanical, and chemical forces can also be dealt with, depending on the specific application.

The tip-sample interaction can be expressed by the Lennard-Jones potential (V_{LJ}, Figure 2.12) as the sum of the attraction and repulsion between the tip's foremost atom and the nearest atom of the sample surface. When the tip approaches the sample, Van der Waals forces cause a tip-sample attraction that scales with r^6, but as the distance between the atoms decreases, they repel with a factor that scales with r^{12}, following Pauli's exclusion principle.

In modern AFM setups, the cantilever's deflection is measured by an optical lever read-out system [x]. An infrared laser is shined on the reflective side of the cantilever, and the reflected beam is collected by a photodiode that converts it to an electric current, thus monitoring its relative displacement during tip-sample interaction. The cantilever's displacement can be converted to an interaction force by further recalling the cantilever behaves like a spring and, therefore, it is subjected to Hooke's law. The

AFM uses two main different modalities for its operation which are referred to as *dynamic* and *contact* modes.

2.4.3 Dynamic mode AFM

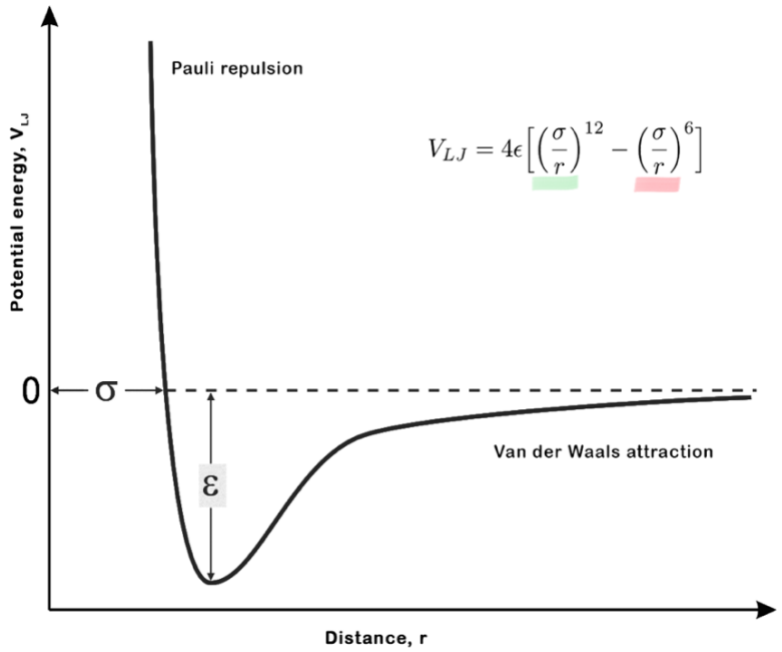

Figure 2.12. The Lennard-Jones potential. Attraction contribution (red) and repulsion contribution (green) are highlighted.

In dynamic mode, the cantilever is dynamically oscillated by a piezo shaker and starts vibrating at the excitation frequency. The tip-sample interaction is confronted to a setpoint variable by the feedback system, which acts to counteract the resulting error signal. The type of such variable varies according to the subtype of operation of the dynamic mode itself. For example – but not limited to – in *frequency modulation* AFM the cantilever's oscillation frequency is the feedback parameter, while in *amplitude modulation* AFM (AM-AFM), the amplitude of such oscillation is the feedback parameter. In *phase modulation* AFM, the phase of such oscillation constitutes the variable regulated by the feedback system.

Dynamic modes can also be classified by means of tip-sample interaction dynamics. In *non-contact* mode, the cantilever is vibrating at an atomic distance from the surface, where only Van der Waals forces are relevant. In *intermittent contact* mode, the

cantilever is brought close to the surface, where both repulsive and attractive forces come into play. In this way, the cantilever is *tapping* on the surface. Generally, intermittent contact AM-AFM is the most common SPM imaging technique for sensitive biological materials such as individual cells, as it allows to gently track their surface while preserving their membrane integrity.

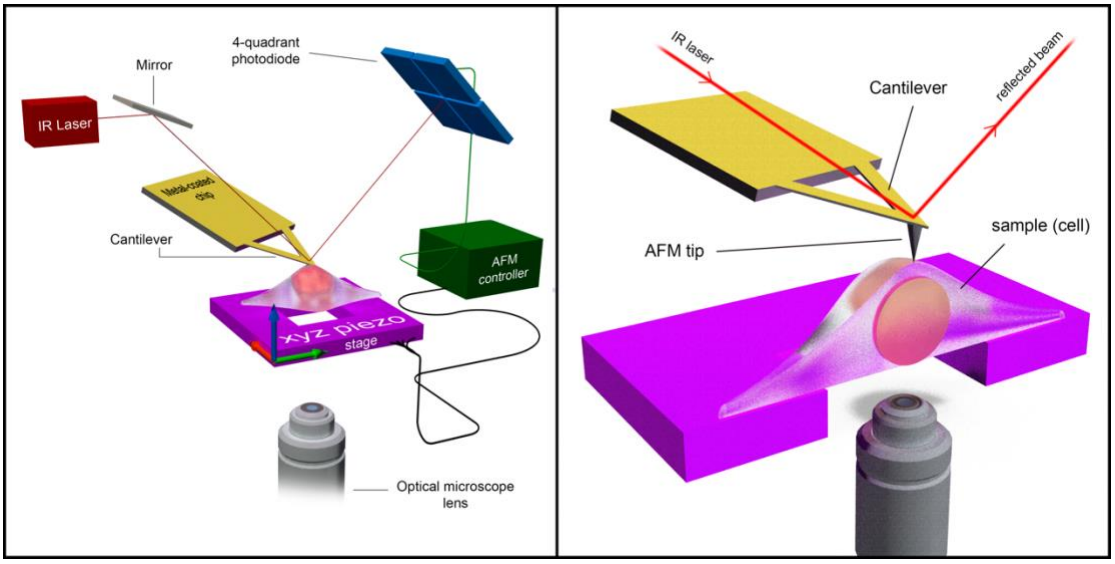

Figure 2.13. Left, scheme of the general setting of an AFM coupled with an optical microscope, highlighting its main components. **Right**, vertically sectioned view of a cell undergoing nanoindentation by a sharp tip. Andolfi et al. 2021

Moreover, the AFM can work in wet conditions, allowing to keep cells in their physiologically optimal shape. In liquid dynamic imaging, however, the mechanical coupling between piezo shaker and the environment – as the liquid itself – leads to a spurious noise in the cantilever's frequency response, making its tuning procedure and the following imaging procedure more challenging. To overcome this issue, the use of a laser beam has been proposed as an alternative strategy to drive cantilever's oscillation [Pini/Vassalli 2010]. In this way, an excitation laser focused on the cantilever's base is modulated at high frequency. As the cantilever's back side is usually metallized, a time-dependent temperature distribution is locally generated, causing a differential longitudinal stress across its thickness. Due to differences within the thermal expansion coefficients of cantilever's bulk and coating, such photothermal effect results in a significant time-dependent bending. *Photothermal excitation* is now a

widely available feature of modern AFMs, allowing a straightforward dynamic imaging procedure in liquid environments.

2.4.4 Contact mode AFM

Contact mode implies that the tip-sample interaction happens within the repulsive regime of the Lennard-Jones potential. The repulsion force acting on the tip is rigidly transferred to the cantilever, causing it to bend upward in a linear manner, following Hooke's law. For brevity, we will only discuss the vertical deformation of the cantilever, although torsion and lateral shifts also occur (and are promptly acquired as a *lateral deflection* thanks to four-quadrant photodiodes in modern AFMs).

2.4.5 Nanomechanical studies by AFM

The AFM is a powerful tool to investigate the mechanical properties of materials, cells, and even individual biomolecules at the micro and nanoscale. By studying the rheological properties of cells, we can gain insight into the complex interactions within and between them, such as the ones driven by adhesion, mechanosensing, and viscoelasticity. Dynamic AFM has been successfully employed to study the rheological properties of cells [x], however, for the purpose of this dissertation, we will focus on contact-based techniques, particularly on the ones regarding a uniaxial deformation and solely along the (Z) vertical axis.

The AFM's feedback can be exploited to apply a certain stress (σ) and measure the resulting strain (ε) of a sample. The sample's strain is the vertical displacement imposed by the cantilever to obtain that σ, corrected for the cantilever's bending. Such bending is linearly proportional to its spring constant. Therefore, for contact-based nanomechanical studies, it is imperative to *know* the elastic constant of the cantilever. The *nominal* elastic constant (K) of a cantilever is given by the equation:

$$K = \frac{E \cdot t^3 \cdot w}{4 \cdot l^3}$$

Where E is the cantilever's Young's modulus, t is its thickness, w its width, and l its length. However, the nominal K of a cantilever is a rarely accurate, as each production batch can slightly differ in terms of the material's residual stresses, thus affecting its E.

Therefore, an experimental calibration is needed, prior to each mechanical characterization, to approximate the *real* cantilever's K.

2.4.5.1 AFM probes calibration

The cantilever is mounted on the AFM head and is located close to a non-deformable surface such as glass. Then, the Z-piezo finely drives a calibrated tip-sample interaction (expressed as a distance variation), and the photodiode measures the laser displacement (as a voltage variation) resulting from the cantilever's bending. A linear fit of the repulsive contact region of such *voltage-distance* curve (Figure 2.14-I) provides the *sensitivity* of the system, calculated as the reciprocal value of its slope.

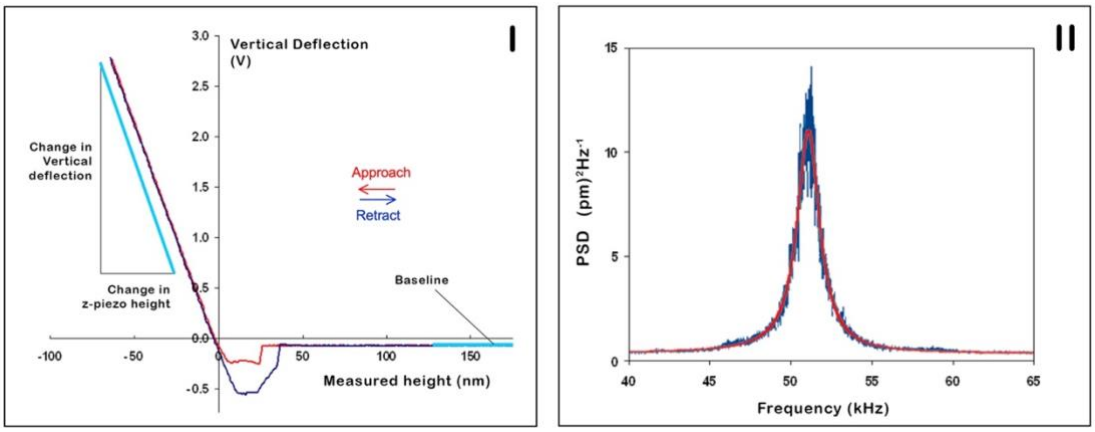

Figure 2.14. I, an indentation curve on a hard surface that shows how the sensitivity of the cantilever is calculated: Δ(vertical deflection) / Δ(z-piezo height). **II**, Thermal noise spectra around the resonance frequency of the cantilever, with the corresponding Lorentzian fit (red line). Bruker Nano GmbH.

Once such deflection is expressed as a distance via the sensitivity ratio, it needs to be converted to an actual force value, by multiplying it by the lever spring constant. The actual spring constant can be derived using various strategies, for example by the *spring-to-spring* method, and the *thermal noise* method. The first will be discussed in detail in Chapter 4, as it represents the way to define the K of our custom-fabricated Macro probes. The thermal noise method is a gold standard in modern AFMs and arises from the equipartition theorem. Indeed, the cantilever oscillates on its own because of intrinsic thermal fluctuations. The equipartition theorem relates the temperature of a system to its average energies, so the energy stored by the spring is equal to its thermal energy:

$$\frac{1}{2}k\langle x^2\rangle = \frac{1}{2}k_B T$$

While the Boltzmann's constant (k_b) and Temperature (T) are known, k is the unknown spring constant, and $\langle x^2 \rangle$ is the mean-square-amplitude of the cantilever's deflection as collected and processed by the control software. A power spectral density (PSD) analysis the cantilever's fluctuation is performed to obtain $\langle x^2 \rangle$. Around its resonant frequency, those fluctuations disseminate around a peak that is fitted to a Cauchy-Lorentz function (Figure 2.14-II). By integrating the curve, the AFM software automatically extrapolates the lever's K.

The following nanoindentations are nowadays conducted in *Z closed-loop mode* to correct for deviation from linearity caused by piezo hysteresis, particularly over large indentation sweeps. Such mode allows for the independent measurement of the z-position of the piezo and modulation of its excursion through an additional closed-feedback loop.

2.4.5.2 AFM nanoindentation: force spectroscopy

To perform a nanoindentation experiment aimed at evaluating cell elasticity, a force spectroscopy sweep is performed at *slow indentation speeds* to minimize viscosity contribution. To do so, the cell is locally poked by the AFM up do a definite *force setpoint.* After the indentation curves are acquired, data post-processing is required to determine Young's modulus. This primarily involves leveling the curve by subtracting its baseline, which is linearly fitted from the non-contact (i.e., approach) region. Then, the lever's elastic contribution is subtracted from the data, to obtain a force-indentation (F-δ) curve. It should be noted that this is not the same as a *stress-strain* curve, as estimating the stress implies the contact area is known. Particularly with soft materials, the relationship between applied load and measured deflection is nonlinear, as the tip-sample contact area progressively increases as the tip is indenting the sample. Therefore, an appropriate contact mechanics model has to be applied in order to quantify the Young's modulus.

2.4.5.3 AFM nanoindentation: stress-relaxation

Another response that can be investigated from a mechanically loaded cell is the one ruled by viscoelasticity. To do so, a *stress-relaxation* experiment can be performed. During stress-relaxation, a cell portion is uniaxially compressed of *a given vertical range* by the cantilever tip. Such controlled displacement is finely regulated by the Z-piezo itself, which is eventually locked exploiting its z-closed loop control, thus holding the position for long time intervals of the order of tens of seconds, minutes or more. In this way, a decaying Force-Time curve is acquired, and analyzed accordingly.

2.5 Models to evaluate cell mechanics

2.5.1 Young's Modulus evaluation

The evaluation of a cell's Young's modulus often relies on the Hertz model of elastic deformation of bodies. This model describes how an elastic sphere deforms under a specific load, and it assumes that certain conditions are met. Those conditions include (i) the indenter must be a parabolic or spherical shape and must not deform, (ii) the sample is isotropic and much thicker than the indentation depth, and (iii) the deformation must be entirely elastic, therefore neglecting viscosity.

If these conditions are met, the Young's modulus can be calculated using the following equation, which assumes a spherical indenter is used:

$$F = \frac{4}{3} \cdot \sqrt{R} \cdot \left[\frac{E}{1-\nu^2} \cdot \delta^{\frac{3}{2}} \right]$$

This is the Sneddon's modification of the Hertz model, usually employed in force-indentation curve fitting. R is the radius of the spherical tip, E is the Young's modulus of the sample, δ the indentation depth and ν the Poisson's ratio, that is the opposite of the ratio between transverse and axial strains of an object under unidirectional deformation (for biological sample usually in the 0.2 – 0.5 range).

However, the coexistence of different structural layers within the cell makes it more complicated than a homogeneous mass, and different structures may contribute to the induced deformation, so different elastic regimens at discrete indentation depths are expected. Indeed, there is always the possibility of considering a modified Hertz model[78] encompassing both the elastic response of the cell outer layer and, a second elastic response of the internal ones. Thus, the curve fitting equation can be modified as it follows:

$$F(\delta) = F_0 + A1(\delta - \delta_1)^{3/2} + A2(\delta - \delta_2)^{3/2}$$

$$A1 = \frac{4}{3} \frac{E1}{(1-\nu^2)} \sqrt{R}$$

$$A2 = \frac{4}{3} \frac{E2}{(1-\nu^2)} \sqrt{R}$$

Where $E1$ and $E2$ represent the Young's modulus as of the first and second elastic component, respectively. δ_1 and δ_2 are the indentation depths interpreted as first and second contact points, and can be obtained from the curve (visually, δ_1 is the point in which the deflection starts to rise, δ_2 is where it sudden changes its trend).

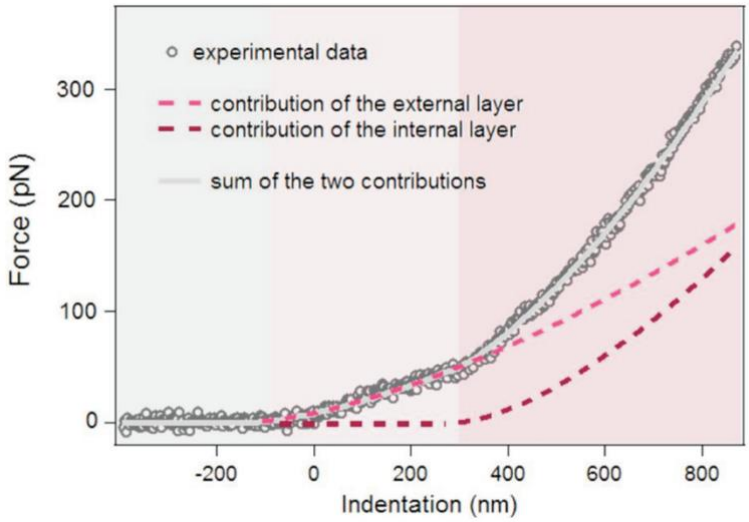

Figure 2.15. Sketch illustrating the indentation steps of a bead on a cell. Before the first contact point: no indentation forces. Between the first and the second contact points: indentation forces are generated exclusively by the contribution of the external layer. After the second contact point: both external and internal layer contribute to the indentation force. Qi et al., 2016

2.5.2 Viscoelastic relaxation time

As occurred for force spectroscopy, the recorded data analysis involves a proper mathematical model to which the decaying curve needs to be fitted, to extrapolate the relaxation time. The viscoelastic behavior of a cell experiencing a sudden and constant deformation is well explained by the generalized Maxwell model.

A Maxwell body is a material characterized by both elastic and viscous properties. Accordingly, a single *Maxwell element* can be represented by a pure viscous damper and an ideal spring connected in series[106]:

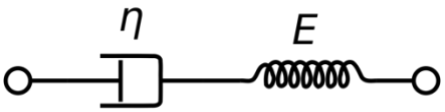

Figure 2.16. A simple Maxwell element diagram.

When a Maxwell material is subjected to a sudden deformation and held to a constant strain, then the stress decays on a timescale of [$\tau = \eta \cdot E^{-1}$] where η is the material coefficient of viscosity, and E the elastic modulus.

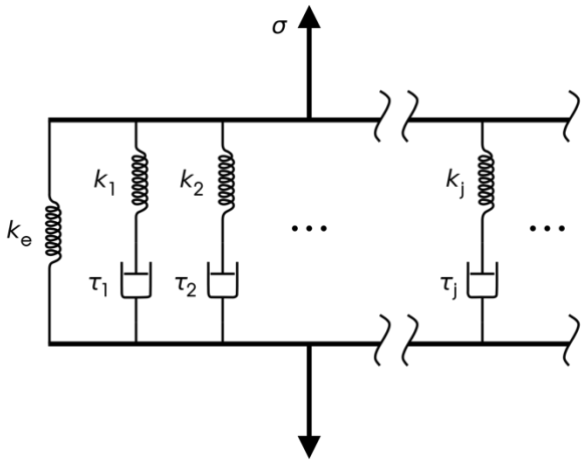

Figure 2.16. Schematics of Maxwell-Wiechert model.

While acknowledging this interpretation as more accurate regarding the challenge to outline the mechanics of a biological system, the presence of several cellular components must not be overlooked (as it happens for Young's modulus estimation). Indeed, these structures are diverse from a molecular perspective, and therefore distinct viscous responses are expectable. The Generalized form of this model (also

called Maxwell-Wiechert model) takes into account that the relaxation occurs in a set of times, rather than in a single time, and can be depicted as in the following:

In the Generalized Maxwell model, a set of Maxwell elements are assembled in parallel. While *many* Maxwell elements could theoretically describe the cell mechanical behavior in a more fulfilling manner, their application should be cautious to avoid data overfitting.

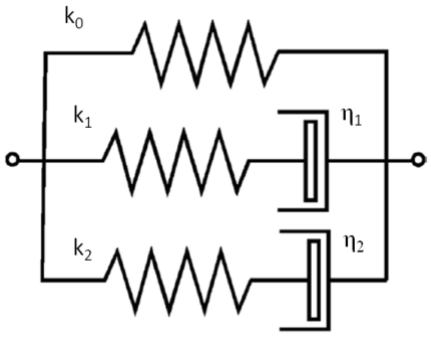

$$F(t) = a_0 + a_1^{-\frac{t-t_0}{\tau_1}} + a_2^{-\frac{t-t_0}{\tau_2}}$$

Figure 2.17. Left, schematics of the generalized Maxwell model used during our experiments (two-exponential model). Right, the equation to which the relaxation decays have been fitted.

2.6 AFM in cardiology

AFM has been used to study the mechanical properties of heart cells, such as their stiffness and viscoelasticity, which turned out to be indicators of cardiomyocytes health. At the single-cell level, some authors were also able to measure the beating force of single or clustered cardiomyocytes. Moreover, it was successfully used to study the pathophysiological fingerprint at the tissue organization level, disclosing relevant mechanical features of the diseased myocardium.

2.6.1 Cardiomyocytes elasticity

The AFM has been extensively used to probe the mechanical properties of single cardiomyocytes.

Azeloglu and Costa [19] used it to study NRVMs during systole and diastole, finding heterogeneity in mechanical properties within cells and increased stiffness during contraction. Blebbistain, a drug that inhibits actin-myosin interaction in the heart, was shown to lower elasticity to diastolic levels.

In another study, primary adult mouse heart cells were exposed to doxorubicin (an anthracycline anticancer drug) and dexrazoxane (a cardioprotective agent) to assess the effects of these drugs on cell stiffness [22]. Doxorubicin-treated cells showed normal stiffness for the first 50 minutes, followed by significant softening, but pre-treatment with dexrazoxane prevented these changes.

AFM was also used to examine the role of cytoskeletal proteins in cell structure and function, as seen in the case of vinculin. Cardiomyocytes from mice lacking vinculin were softer than those from wild-type mice, but vinculin restoration restored elastic modulus to normal levels as shown by Tangney et al. [24].

Liu et al. used AFM to compare the mechanical properties of induced iPSC-CMs from healthy individuals and patients with dilated cardiomyopathy. The findings showed that the elasticity of iPSC-CMs was reduced in patients with DCM.

Regarding actin, embryo-derived CMs were analyzed after administering cytochalasin B to examine the impact of an impaired actin network on their Young's modulus [21], finding a consistent decrease in elasticity after actin depolymerization.

Additionally, the Young's modulus of NRVMs was measured to understand the impact of genetic mutations in A-type lamin, the cause of a specific group of diseases known as laminopathies. Such study by Lanzicher et al. found that NRVMs with the human D192G LMNA mutation were stiffer compared to those with the wild type transfected human lamin, and control NRVMs.

To summarize, mechanical properties of single cardiomyocytes exhibited heterogeneity with increased stiffness during contraction. Common drugs and genetic mutations were shown to impact the elasticity of cardiomyocytes, as also the impairment of cytoskeletal proteins showed the same trend.

2.6.2 Cardiomyocytes viscoelasticity

Far less literature is available with regards to the viscoelastic properties of CMs probed via AFM.

In a study by Lanzicher et al. [43], stress relaxation experiments on the same LMNA-mutated NRVMs were performed. The results showed the cells transfected with the mutant gene showed a decrease in viscosity, which the authors attribute to a reduction in the length and thickness of the actin cytoskeleton elements caused by the lamin mutation.

Deitch et al. [47] assessed the impact of different substrates (fibronectin- or collagen-coated, aligned or not) and aging (1 to 15 days of culture) on the viscoelastic behavior of NRVMs via stress relaxation. Results showed a decrease in percent relaxation from day 1 to 3, then stabilized. CMs on aligned substrates showed generally lower relaxation than those on random coatings due to better orientation of actin fibers which counteracted stress.

Robison et al. [48] used AFM to study the impact of detyrosination on microtubule buckling/sliding during contraction in adult rat ventricular myocytes, where microtubules serve as force-bearing structures anchored to sarcomeric Z-disks by desmin. Results showed a significant reduction in elasticity and viscosity when detyrosination levels decreased compared to controls. Desmin depletion, on the other hand, decreased cell stiffness due to missing connection to microtubules, but had no impact on viscosity after detyrosination reduction.

2.6.3 Cardiomyocytes mechanocardiograms

One of the trendiest applications of AFM in cardiac mechanobiology is the passive monitoring of the CM beating activity. Indeed, by observing the vertical deflection on a beating CM, information about twitching force, frequency, and Z-cell displacement is gained. This is probably one of the most impressive applications of the AFM in CMs mechanobiology, replicating what it is normally done through an ECG, but measuring a mechanical dynamic parameter instead of an electrical one, all done at the single-cell scale.

The first characterization of the beating profile of cardiomyocytes (CMs) was performed by Domke and colleagues in [50]. They measured the height change and the vertical deflection of the cantilever due to each pulse of the beating CMs. However, considering that contraction of CMs is primarily a lateral displacement, Liu et al. [51] suggested the cantilever's lateral (torsional) deflection as a more reliable signal to measure contractile activity. Nevertheless, most studies still consider vertical deflection, since the associated force can be easily calculated by multiplying the deflection signal by the sensitivity and spring constant of the cantilever.

Chang et al. [52] introduced the short-term Fourier transform to identify slight variations in the beating frequency and suggested its application to detect changes in CM dynamics after drug administration. The confluence level of CM culture is a crucial factor affecting the beating profile, with the frequency being more regular in confluent cultures compared to sub-confluent ones. However, the effect on the beating amplitude is still controversial [31, 50, 52].

Coupling AFM with other techniques provides a deeper characterization of the contractile behavior of CMs. AFM is often mounted on inverted microscopes for simultaneous optical and mechanical investigation of cells. Intracellular oscillation of Ca2+ ions can be monitored by loading CMs with a calcium-sensitive medium, as Ca2+ plays a crucial role in the contraction of sarcomeric units that form the contractile apparatus of CMs [53]. Liu et al. [51] showed a linear relationship between torsional force and calcium flux intensity, whereas vertical deflection did not show such dependence.

Synchronizing the mechanical and fluorescent signals was achieved by Burridge et al. [54], who described the time-dependence between calcium flux and force generation. AFM beating measurement was combined with digital holographic microscopy analysis by Yue et al. [22] to overcome the limitations in the resolution of classical optical methods used to monitor contraction.

Tian and colleagues [55] coupled AFM with a microelectrode array (MEA) to simultaneously characterize the electrical and mechanical activity of contractile CMs. Although limitations were identified, such as accurate cell positioning on the MEA and false peaks in the force and extracellular field potential profiles produced by cell clusters, this method was shown to be powerful.

AFM has been widely used to assess the role of specific genes in beating activity, as their mutations are often associated with cardiomyopathies. For example, Nguyen et al. [56] showed that the knockdown of the stromal interaction molecule 1 (STIM1), a transmembrane protein on the sarcoplasmic reticulum acting as a Ca2+ sensor, decreased the beating regularity of HL-1 cardiac cells. Inhibition of the protein kinase C ε isoform (PKCε), which is associated with decreased phosphorylation of troponin T in ischemic heart failure, was demonstrated to reduce contraction amplitude in neonatal rat CMs [57].

Mutations in the cardiac troponin T can lead to dilated cardiomyopathies, and Sun et al. [58] studied the effects of a point mutation of the cardiac troponin TTNNT2 gene carried by a cohort of patients. The authors obtained cardiomyocytes from patient-specific iPSCs and studied them using AFM. Although the beating frequency and duration were similar to healthy donors, the contraction force was weaker.

CHAPTER 3

Altered nanomechanical properties of cardiomyocytes with Filamin C Truncations

3.1 Introduction

In this chapter, a force spectroscopy study performed by AFM loading-unloading curves will be introduced concisely, to show how the AFM can easily distinguish *at the single-cell level* the mechanical implications of a pathological condition, induced by a genetic mutation, from a physiological-like in a 2D in vitro situation. Two mechanical fingerprints will be highlighted: the cardiomyocytes elasticity, and their unspecific membrane adhesion.

Cardiomyocytes need a mechanome - a chain of elements that respond to forces - to react to the environment. The cytoskeleton, an organized network of polymers, is a crucial mechanosensitive element. Among the three components of the cytoskeleton (actin, microtubules, intermediate filaments), actin is particularly important for maintaining the mechanical properties of the cell, through actin cross-linking or actin binding proteins (ABP). An important class of ABP are filamins (FLNs), which have a unique microstructure and cross-linking properties that allow them to create orthogonal networks of actin filaments. FLNs also provide a mechanical link between the extracellular matrix and the actin cytoskeleton, maintaining cell stability. Mutations in FLNs genes can lead to diseases in the nervous system, cardiovascular system, muscle, and connective tissue.

In this study, we investigate the relationship between altered nanophysical and mechanical properties and biological response in human induced pluripotent stem cell-derived cardiomyocytes (hiPSC-CMs) with FLNC mutations, using a mechanomic approach.

3.2 Experiment workflow

3.2.1 Generation of FLNC^{KO} CMs

In this study, we used cardiomyocyte models including CRISPR/Cas9 genome-edited FLNC$^{KO-/-}$ hiPSC-CMs, a condition that is lethal in animal models and FLNC$^{KO+/-}$, which mimics the heterozygous human disease. We differentiated hiPSC-CMs using previously established procedures. Four lines were derived from commercially available hiPSCs and two additional control lines were developed at UCD. We generated at least 6 lines for each FLNCtv variant and used wild-type FLNC hiPSC-CMs as controls.

3.2.2 Nanomechanical probing

To acquire loading/unloading curves, we used a JPK NanoWizard 4a BioScience AFM. All studies were performed on living, intact cells in cell culture medium, and only well-spread and isolated cells were investigated. Cells with a round shape and a dark edge were rejected. To mitigate the difficulties of comparing cells in different states during tests, we collected multiple measurements from different cells to control for variability and determined an average data, while also monitoring cells and observing their morphological details using an optical light microscope.

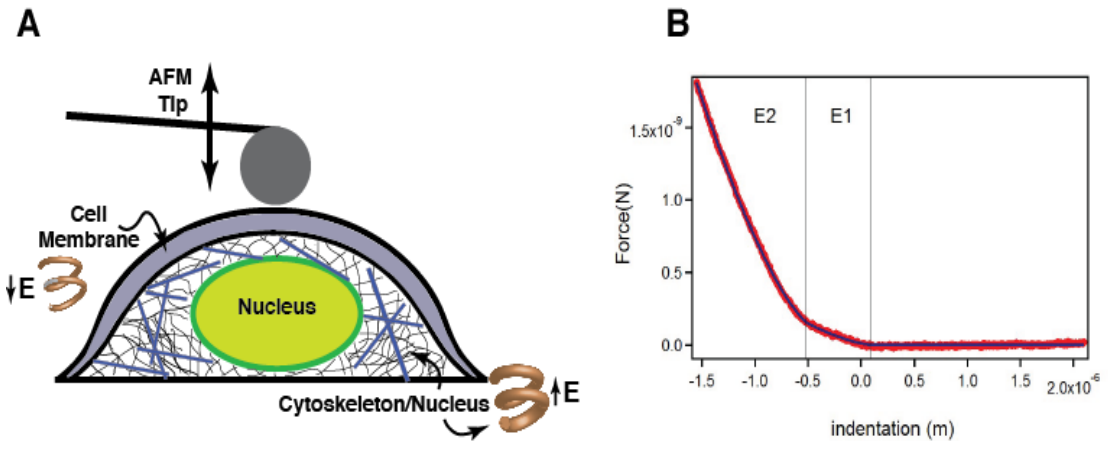

Figure 3.1. hiPSC-CMs single cell spectroscopy. A. Schematic representation of the AFM methodology used to test the stiffness of cardiomyocytes using the spheric tip. **B**. Scheme of the two distinct components of the indentation curve which include E_1 and E_2, where E_1 is related to the compression of the outer cell superficial part, while E_2 to the deeper components of the cell (cytoskeleton and nucleus).

We used a cantilever modified with a polystyrene microsphere Au probe coated with a layer of gold (diameter of ~7 μm) to precisely apply a compression force normal to the nucleus. Spherical probes for soft biological samples are preferrable because they apply the force to a larger cell area, causing lower pressure and less cell damage compared to sharp tips. Additionally, cells or tissues are inhomogeneous, so F-D curves recurrently display two different slopes and do not follow a simple power law function as predicted by the contact mechanics model: E1 is related to the compression of the outer cell superficial part, while E2 corresponds to a deeper part that includes the rest of the cell (cytoskeleton and nucleus).

3.3 FLNC mutations lead to altered nanomechanical properties

3.3.1 FLNC KO cardiomyocytes are softer

When we investigated the hiPSC-CMs models (wild type, $FLNC^{KO+/-}$ and $FLNC^{KO-/-}$), the F-D curve for the analyzed cells showed striking differences, and these differences also emerged in the Young's modulus assessment of cell elasticity. The results based on the modified Hertz model are shown in Figure 3.2B. Both elastic contributions (E1 and E2) show that wild type FLNC iPSC-CMs are stiffer than mutant $FLNC^{KO+/-}$ and $FLNC^{KO-/-}$ iPSC-CMs, which show a progressive loss of stiffness from the heterozygous $FLNC^{KO+/-}$ to the homozygous $FLNC^{KO-/-}$ iPSC-CMs model (Figure 3.2). These results prove that the cell outer superficial layer deforms differently from the rest of the cell underneath, and that this behavior is present in all three cell lines examined.

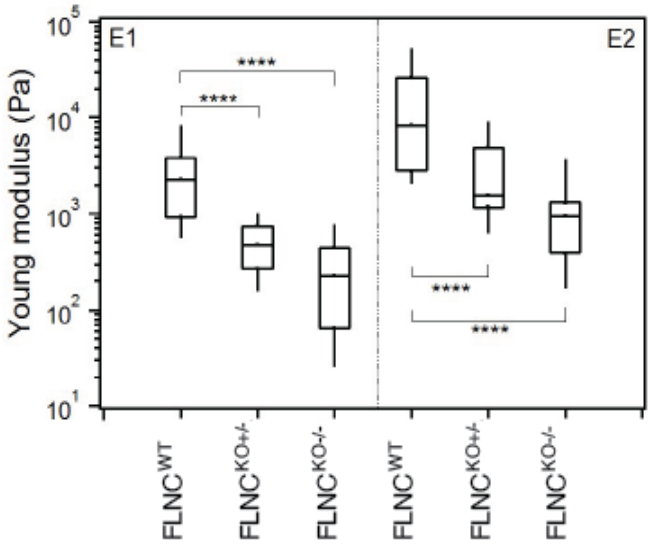

Figure 3.2. Young's modulus distribution of the first (**E1, left**) and second (**E2, right**) Young's moduli. Statistical significance was assessed by Mann-Whitney nonparametric test. All $p < .0001$. Boxplots are showing Median and IQ range. Log(10) vertical scale.

3.3.2 FLNC KO cardiomyocytes' progressive loss of unspecific adhesion

The cell adhesion behavior was measured by assessing the retraction curve of F-D curves. The measured F-D curves were computed in terms of adhesion force (the maximal value of the force exerted by the cell-surface contact to the cantilever during retraction), rupture length (the distance between cell surface and AFM tip at which the

last tether connection breaks) and work of adhesion (integrating the area under the retraction curve), as shown in Figure 3.3.

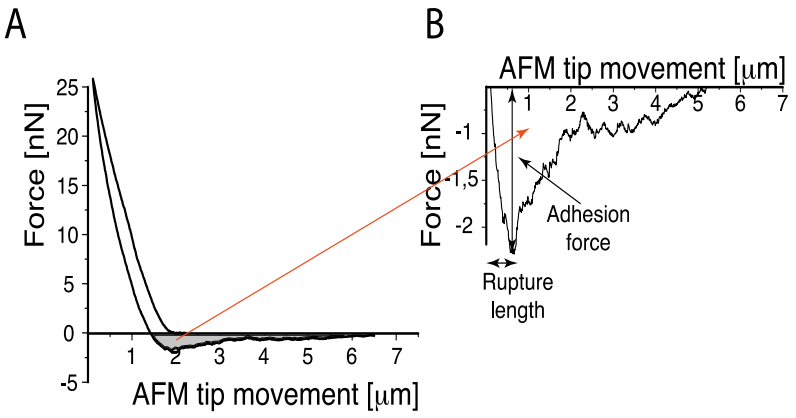

Figure 3.3. (A) an exemplificative AFM loading-unloading curve, where the area from which the adhesion parameters are calculated is highlighted in grey color. **(B)** a detailed view of the area encompassed between the retraction curve and the horizontal axis, which represents the adhesion regime.

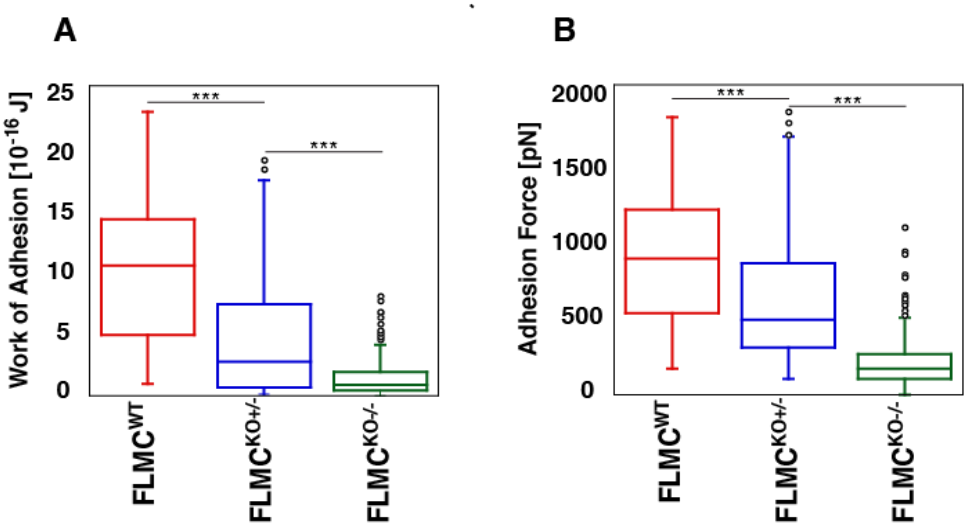

Figure 3.4. Data distribution for Work of Adhesion **(A)** and Maximum Adhesion Force **(B)** showing the progressive loss of unspecific adhesion by FLNC-mutated cardiomyocytes.

The adhesion cell behavior showed the same trend as the elasticity (Figure 3.4): compared to $FLNC^{WT}$ iPSC-CMs, mutant FLNC iPSC-CMs showed progressive decrease of work of adhesion as well as adhesion force from the $FLNC^{KO+/-}$ to the $FLNC^{KO-/-}$ models. Indeed, for the work of adhesion: $FLNC^{WT}$ = 10.90 x 10^{-16} J, std.er. =

1.35; $FLNC^{KO+/-}$ = 2.85 x 10^{-16} J, std.er. = 0.50; and $FLNC^{KO-/-}$ = 0.95 x 10^{-16} J, std.er. = 0.12.

For the adhesion force: $FLNC^{WT}$ = 921.20 pN, std.er. = 64.25; $FLNC^{KO+/}$= 505.09 pN, std.er. = 39.87; and $FLNC^{KO-/-}$ = 176.45 pN, std.er. = 14.77). Finally, the rupture length showed a similar trend, and reached statistical difference between $FLNC^{WT}$ and the $FLNC^{KO-/-}$.

The FLNC protein acts as an actin network crosslinker, thus stabilizing the cytoskeleton. FLNC-depleted cells usually show unorganized cytoskeletal networks. It is therefore reasonable to assume the marked decrease of elasticity, of both the membrane and the underlying structures (showed by E1 and E2 distributions, respectively) is given by such kind of mechanical impairment.

While the measured adhesion was unspecific, as we did not functionalize the AFM spherical indenter by any chemical cues, which could have acted as molecular linkers for membrane proteins (such in the case as RGD motifs for integrins), the observed reduction in both work of adhesion and maximum detachment force is still a relevant aspect, as it may be the result of a reduction of the internal stresses, given by the actin network disarray induced by the FLNC knockout. Indeed, the actin network is involved in cell shape maintenance and force distribution, acting as a tensile scaffold inside the cell. A further discussion of this behavior goes beyond the scope of this chapter, as it is already become clear how the AFM can capture the cell mechanical features in 2D genetic disease models.

Indeed, this finding highlights the role that the AFM could partake in the framework of a diagnostic platform, aimed at discriminating a pathological condition by a physiological one, in a simple 2D culture setting.

It is now the time to move in 3D.

Chapter 4

3D Cardiac Spheroids to investigate heart mechanics

4.1 Introduction

A great deal of interest has been focused on creating more accurate in-vitro constructs of cardiac physiology and disease. Among them, Cardiac Spheroids (CSs) are promising three-dimensional (3D) models [1]. These constructs are built from primary [2] or iPSC-derived cardiomyocytes [3] which assemble to a spherical-like shape. Also, their cell population can be tuned according to the composition of the biological tissue by including other phenotypes, such as cardiac fibroblasts and/or endothelial cells [4]. These models allow to investigate the myocardium behavior within a richer and native environment and are valuable building blocks to bioprint complex microtissues with higher complexity [5,6].

Some studies have already shown the importance of assessing the mechanical properties of CSs. For example, to measure their contractile force, they can be embedded into silicon rubbers whose deflection can be quantified and their action potentials analyzed by fluorescent calcium or potentiometric imaging [7].

However, to have a rigorous estimation of their global mechanical properties such as elasticity, viscosity, and plasticity, we need to consider what has already been developed for similar purposes, but on spheroids made of other cell types. In this regard, we refer to a recent review from Robert C. Boot [8] in which several physical methods are illustrated. Such methods comprise AFM local indentation [9], micropipette aspiration [10], micro-tweezers [11], spheroid fusion [12], and tissue surface tensiometry (TST) [13]. More recently, parallel plate compression has been proposed as a technique able to quantify the viscoelastic properties of living tissues [14]. In parallel plate rheology, a vertical loading of a rigid microplate allows the application of a uniaxial deformation to a spheroid, which is optically monitored by a camera. In this method, as for micropipette aspiration, the main issue is that they both rely on the visual microscopic assessment of the load ratio and, as result, they lack the force sensitivity required to accurately describe relevant phenomena such as small beating force variations.

To address this issue, we have developed AFM-compatible macro-probes that combine the AFM sensitivity with the advantages of parallel plate compression: with such an approach, oocytes deformations were successfully investigated [15], as well as

multiple cell-cell interactions on large areas [16, see also appendix]. With this AFM-based system, the viscous contribution can be assessed by measuring the time of relaxation after sudden stress. During stress relaxation (SR), the whole spheroid is uniaxially compressed between two plates. Its displacement can be finely tuned by acting on the AFM piezoelectric actuator. Finally, its z-feedback loop is exploited to hold the position for long time intervals on the order of tens of seconds, minutes, or more. A Force-vs-Time curve is recorded and analyzed accordingly.

The purpose of this SR experiment is to demonstrate that, by using our AFM parallel macro-probes, it is possible to obtain relevant data regarding the viscoelastic behavior of whole cardiac spheroids and, by extension, of the myocardium itself. To our knowledge, this kind of evidence had not been disclosed yet because of the lack of a direct, and quantitative, physical technique.

More importantly, the macro-probes find their ultimate application in the field of mechanical stimulation. It is now generally accepted that external aids play a fundamental role in cardiomyocyte development. Mechanical stimulation increases matureness by activating hypertrophic pathways, while electrical stimulation improves connections and calcium handling [17]. On this matter, in this article, we also show how these macro-probes can be used to stimulate and monitor CSs contractility in real-time as if we are doing a “micro” heart massage.

4.2 Experiment pipeline

4.2.1 Primary Cardiomyocytes Extraction

Post-natal day 3 (P3) Wistar rats are euthanized by decapitation and their chest cavity exposed by surgical incision. Ventricular Myocytes (NRVMs) are isolated following a well-established protocol [20-22] with minor modifications. Extractions mostly yield ~ 0.4 M viable NRVMs per heart. Briefly, hearts are pulled from the aorta and placed in a 50 mL centrifuge tube containing ice-cold CBFHH (Calcium and Bicarbonate-free Hank's buffer with Hepes) supplemented with Penicillin (50 U/mL) / Streptomycin (50 μg/mL) and Heparin (Sigma® H3149 at 2 U/mL). Each heart is aseptically minced using surgical scissors, attaining regularly sized fragments of ~ 1 mm. Tissue is digested at RT in the same buffer supplemented with Trypsin (Sigma® T4799 at 0.70 mg/mL) and DNAse I (Roche AG at 25 U/mL), to limit cell clumping, over 3 hours. The cell suspension is then centrifuged (300 RCF, 10'), the supernatant discarded, and the pellet resuspended in fresh growth media (Sigma® M0643 MEM supplemented with 5% Calf Serum, 0.2% Penicillin-Vitamin B12). Fibroblasts are removed by pre-plating for 45' into 2x T75 flasks. Finally, enriched NRVMs are collected from the flasks' supernatant, centrifuged again (100 RCF, 5'), and re-suspended at a density of 2.5 M/mL in fresh media.

4.2.2 3D Cardiac Spheroids Plating

Cardiac Spheroids (CS) are formed via the hanging drop method [23] starting from the 2.5 M/mL single-cell suspension. For this purpose, a 96 mm ø polystyrene Petri dish is flipped upside down. Twenty drops of 20 μl each of cell suspension are pipetted on the inner lid, resulting in ~ 50k cells per drop. The bottom plate is then filled with sterile water, and the lid is flipped onto it, leaving the drops hanging. CS assemble over three days of incubation at 95% H_2O, 5% CO_2, 37 °C atmosphere.

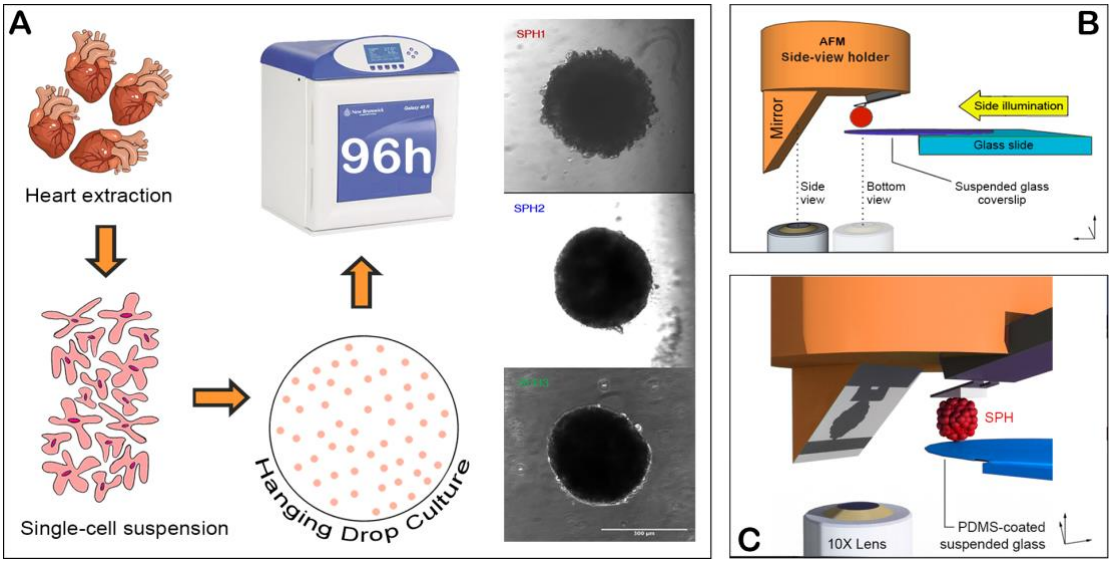

Figure 4.1, A. Scheme of the CSs plating. SPH1/2/3 are shown on its right as taken from the inverted microscope before the actual measurement. Notice how SPH1 displays an irregular cell corona. **B/C.** CAD renders (Adobe® Photoshop 3D) of the JPK NanoWizard® II in side-view configuration. Detail **(C)** shows a computed ray-traced projection of the side-view as reflected by the suspended mirror.

4.2.3 AFM Macro-Probes Fabrication

Different geometries and materials were evaluated using finite element analysis on COMSOL Multiphysics®, to achieve a suitable compromise between strength and sensitivity of the cantilever and to match the geometrical constraints imposed by large biological samples. Considering the size of multicellular spheroids (ranging from 100 to 400 μm), we developed a suspended Si_3N_4 cantilever of 300 x 300 μm in a square area, connected to the chip bulk through a pair of 100 x 100 μm arms. These arms are crucial in defining the stiffness of our system, as they sustain the stress induced by the cantilever deflection. The theoretical spring constant of such probes is ~ 4 N/m as calculated from COMSOL simulations.

The fabrication workflow, as already described in [18], consists of a combination of UV photolithography and dry/wet etching procedures. Those steps have been performed at the Nanofabrication Facility of Friuli Venezia Giulia (FNF, https://fnf.iom.cnr.it).

We begin by sputtering a thin layer (100 nm) of Cr on both sides of a 2 μm low-stress Si3N4-covered silicon wafer using a custom-built magnetron sputter-coater. The wafer surfaces were previously cleaned and activated in Piranha solution (30% H2O2 in 96% H2SO4 3:7). The pattern is transferred on the Cr-coated wafer using UV

photolithography: MEGAPOSITTM SPRTM 220 1.2 (Micro Resist GmbH) is spin-coated at 3000 rpm for 1' on both sides of the wafer, which is later baked at 115 °C for 1'30" on a generic hotplate. The following double-sided exposure under 375 nm UV light - by means of a MA25 mask aligner (Karl Suss KG) - make the exposed areas soluble in MF-24A solvent (Micro Resist GmbH).

After development, the exposed Cr is selectively etched away using an Ammonium Cerium nitrate/Acetic acid/H2O 6/1.1/18 solution. The sample is subjected to Reactive Ion Etching (RIE) for 1 h in a mixture of O2/CF4 plasma sustained by a DC bias of 100 W to expose the silicon beneath. A subsequent wet etching, performed in heated (80 °C) and stirred KOH solution (6.9 M), opens those areas, leaving the chips suspended and connected by structural branches. A thin (25 nm) layer of Au is finally evaporated onto the top side of the wafer to improve laser reflection on the AFM photodiode.

4.2.4 Macro-Probes Polymeric Wedging

In almost every AFM setup, the cantilever hangs tilted from 10° to 20° to prevent any possible chip crash on the uneven sample surface.

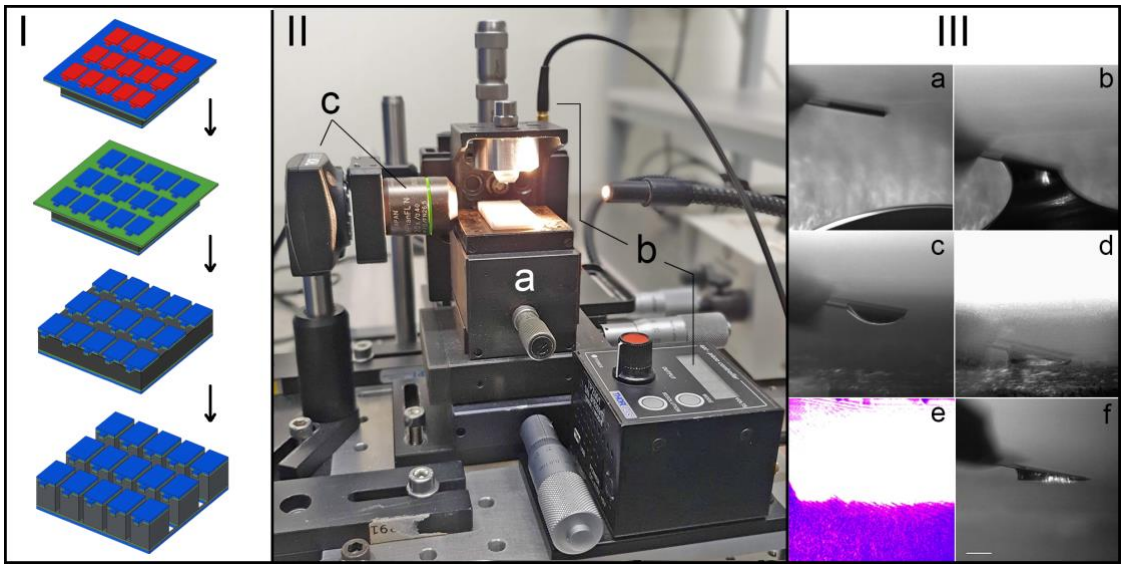

Figure 4.2 (I) Brief scheme of a 3D section of the wafer undergoing progressive etching, after patterning. **(II)** Picture of the wedging setup highlighting the z-stage mount **(a)**, the piezo-driven vertical positioning system **(b)**, and the lens/camera assembly **(c)**. **(III)** micrographs of the actual wedging procedure as taken from camera assembly, showing **(a)** cantilever's approach, **(b)** glue fishing, **(c)** fished drop, **(d)** wedge pre-formation on PDMS, **(e)** UV exposure, **(f)** polymerized wedge. Scalebar: 100 μm

Considering the shape of our macro-probes, the above-mentioned pitch would hinder the application of a uniaxial loading, hence promoting indentation rather than uniform compression or inducing uncontrolled spheroid deformation and shifting during measurements. To provide a parallel and uniform compressing surface, we fabricate a polymeric wedge under the cantilever's active area following the already described protocol by Steward and co-workers. [18]

We set up an optical path on an aluminum optical breadboard (Thorlabs), which is shown in figure 4.2-II. The setup consists of three main components: a 375 nm laser (not shown) which allows a rapid polymerization of the glue, a polymerization stage made of top and bottom plates (figure 4.2-II. a,b), and an optical assembly made of a 20X LWD lens (Olympus) coupled with a CMOS sensor (Thorlabs® 1625) for magnified observation (figure 4.2-II-c).

Once the cantilever is punched out of its fabrication frame, it can be fixed to the appropriate AFM probe holder. The holder should always match the geometry of the available AFM since every instrument has its own mounting tilt. In our case, we employed a spare glass holder from JPK Instruments AG. Afterwards, the holder is secured to the top plate, whose vertical displacement can be adjusted using a single-axis translation stage driven by an amplified piezo motor (Thorlabs® TPZ001). Therefore, the Z position can be controlled in a standardized manner, which is necessary to fabricate reproducible wedges over a batch of macro-probes.

A tiny (about 10 uL) drop of a photopolymerizable glue (NOA 63) is deposited on a polydimethylsiloxane (PDMS, Sylgard 184, 1:10) membrane. Such membrane had been previously silanized to boost its hydrophobicity and ease the detachment of the glue after polymerization. The membrane is then placed on the stage's bottom plate and the glue is localized under the cantilever by focusing on the lens field. While inspecting the camera, the motorized Z-stage is lowered, and the probe is brought into contact with the glue. After 5 seconds, the cantilever is lifted, and the fished glue is again pressed on a membrane's free area, where the wedge is polymerized by the UV laser for 5 minutes. To avoid any breakage when lifting the probe from the PDMS, the stage is retracted at a slow speed of ~ 5 μm/s until complete separation. An additional 2' UV exposure further hardens the glue. The elastic modulus of cured NOA73 is 11 MPa,

which is thousands of times stiffer than that observed on multicellular systems. Therefore, it can be assumed to be infinitely rigid for our purposes.

4.3 AFM Macro probes features

The micromachining process resulted in a series of probes batch suspended from a silicon frame via connecting arms (Figure 4.3-A).

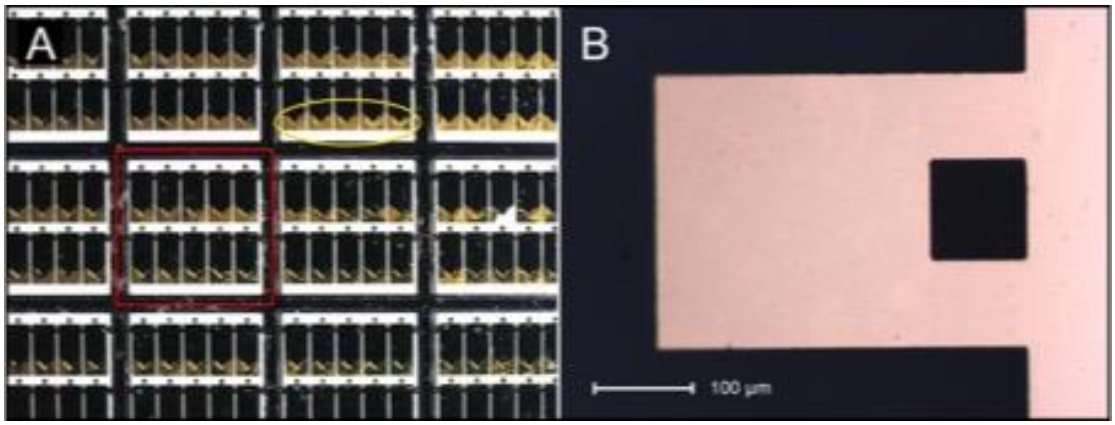

Figure 4.3, A. central section of the processed silicon nitride wafer. A single element is made by 10 individual chips (red square). The opposite end from the macro-probe (yellow circle) displays unwanted silicon etching. **B**, an optical micrograph of the suspended macro-probe prior to wedging.

The fabrication met the physical requirements, although there was an undesirable over/under etching of the silicon at the end of the chip, opposite to the cantilever side. This can be seen in figure 4.3-A where black regions are silicon while the yellow ones are gold-coated silicon nitride membranes. However, if mounted properly, this defect does not affect operation. In attempting to solve this minor problem, a slight redesign of the optical masks might be considered.

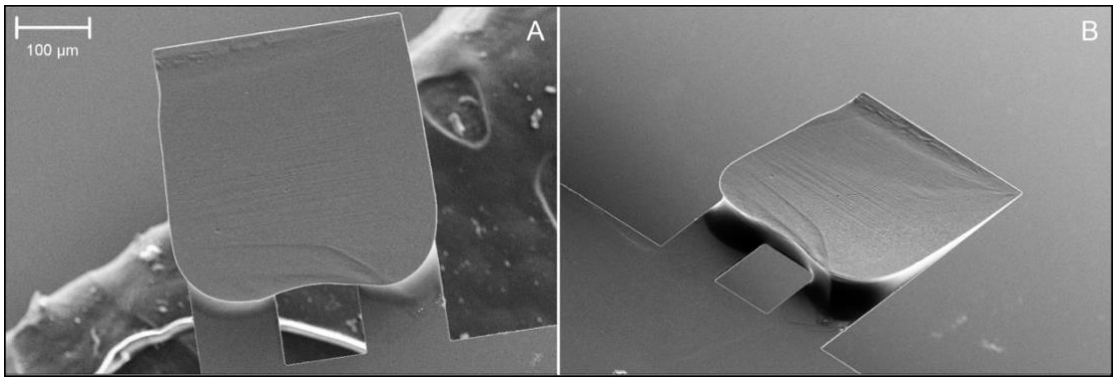

Figure 4.4 SEM micrographs of the bottom side of the probe after its polymeric wedging. Small imperfections can be observed, especially from a tilted angle (**right**).

Regarding the polymeric wedge, SEM imaging (Figure 4.4) shows the detachment pattern of the hardened NOA73 resin, represented by transverse lines. This can result from the separation of the surfaces (i.e., the resin and the PDSM) occurring in discrete steps rather than continuously. One way to minimize this effect would be to extend the curing time, but this could strengthen the bond between the adhesive and PDMS, making them harder to separate, to the point of fracturing the Si3N4 arms. Nevertheless, this microscopic pattern does not affect the performance of the measurements because the lines are narrow, and the roughness lies in the order of hundreds of nanometers. Larger detachment lines could have caused multiple indentations instead of a uniform compression, which is why it is important to fabricate a smooth surface.

After the calibration, we determined the macro-probe spring constant to be K = 1.67 N/m

4.3.1 Macro-Probes Calibration

We calibrate our macro-probes via the spring-to-spring method [27] using a reference spring, a PPP-FM cantilever from Nanosensors®, with a known spring constant KR = 2.15 N/m measured by thermal noise method. We start by mounting our chip on the AFM glass cube and positioning the laser spot on its center. Then, a series of voltage/distance curves are taken by pressing the macro-probe onto a glass surface, extrapolating the ratio between the laser deflection (as voltage variation) caused by the associated piezo excursion. The linear fit of the curve after the contact point leads to its slope, that is, the Absolute Sensitivity of the macro probe (S0). We repeat the exact measurement pressing the probe onto the reference cantilever end, obtaining a Relative Sensitivity (SR) proportional to the concomitant deflection of the reference.

The spring constants (K) of the macro probes are computed according to the equation:

$$K = K_R \cdot \left(\frac{S_R}{S_0} - 1\right)$$

4.3.2 AFM measurement setup

The wedged and calibrated probe is mounted to the side-view cantilever holder of a JPK NanoWizard® II AFM. We choose such a holder as it bears an inclined mirror on

the cantilever forefront, allowing us to look at the spheroid deformation from the aside. However, this implies the need to perform these measurements on the edge of a stepped surface to avoid mirror crashing. For this purpose, a set of 24 mm ø glass coverslips are spin-coated with the PDMS premix at 2000 rpm and cured overnight in a ventilated oven at 70 °C. To obtain a suspended platform, we use NOA73 optical adhesive (Norland Products, Inc.) to glue a cleaved piece of microscope slide inside a 35 mm ø Petri dish cover. On top, we glue the PDMS-coated coverslip in such a way that roughly half of it protrudes toward the center of the Petri. The hanging platform is finally positioned on the JPK CellHesion® module, which enables an extended z-piezo excursion of 100 μm. This measurements setup is represented in figure 4.1, panels B/C.

4.3.3 Stress relaxation measurements of Cardiac Spheroids

At the fourth incubation day, each spheroid has a diameter ranging from 300 to 400 μm (Figure 4.1-A). After its retrieval, a 10 μL drop of Hank's Buffer with Hepes (HHBS) is placed on the edge of the PDMS coverslip and the spheroid is rapidly transferred inside it. Thanks to the surface hydrophobicity, the CS remains confined and is rapidly localized. Then, the CS is approached with the probe and wait for a weak adhesion to set in. After about 1 min, the probe is slightly lifted (5 μm) from the surface, along with the fished CS. Finally, we carefully fill the Petri lid with warm HHBS while the spheroid hangs from the probe.

To start the SR, the stage is lifted by 30 μm (500 ms) towards the cantilever, so the spheroid becomes suddenly compressed. Then, the piezo is locked in position and the relaxation pattern of the spheroid is monitored by measuring the cantilever vertical deflection over time. On each spheroid (SPH1/2/3) 10 to 12 curves are collected with 5 s pauses in-between. Then, each Force vs Time curve is analyzed by fitting the data to a two-component Maxwell model by least-square method. The model is described by the following equation:

$$F(t) = a_0 + a_1 \cdot e^{-\frac{t-t_0}{\tau_1}} + a_2 \cdot e^{-\frac{t-t_0}{\tau_2}}$$

The model considers an initial, elastic response and a following viscous relaxation. Therefore, each CSs is approximated to a pure viscoelastic body whose relaxation occurs in a set of times, $\tau 1$ and $\tau 2$, where:

$$\tau = \frac{\eta}{E}$$

i.e., the ratio between the viscous and the elastic components. The fitting procedure is performed on Igor Pro (Wavemetrics Inc.), and finally, values are mediated for each CS.

4.4 AFM Macro probes to measure the mechanical properties of CSs

An example of the SR experiment on a single spheroid is shown in Figure 4.5.

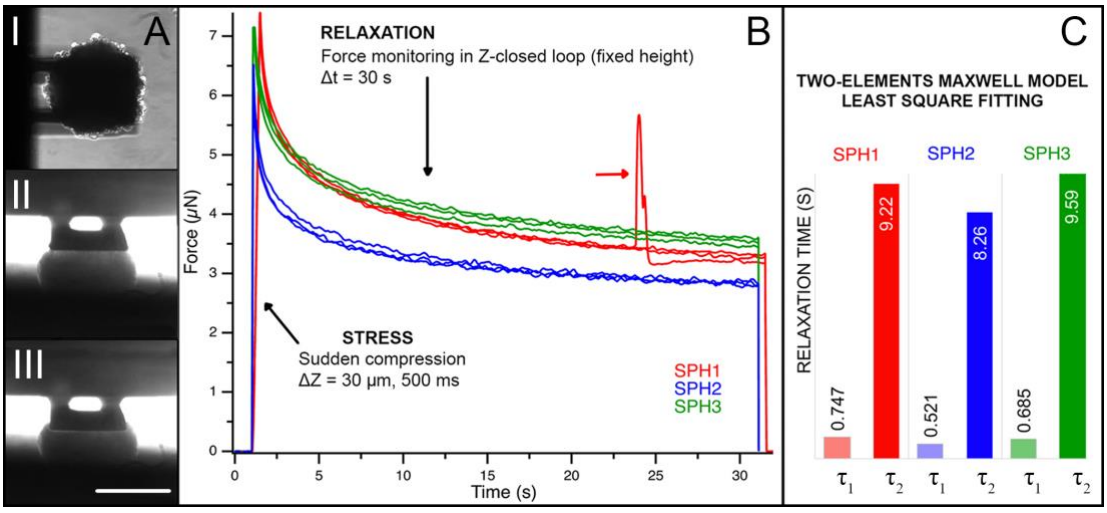

Figure 4.5, A. Optical images of a CS under a macro-cantilever. **(a)** Bottom-view. **(b)** Side-view imaging before compression **(c)** After compression. Scalebar: 300 μm. **B**: nine stress-relaxation curves as obtained through the AFM, after baseline subtraction. The samples (SPH1/2/3) showed similar relaxation patterns. SPH1 shows contractility (red arrow) at ~ 25 s. A fast (τ1) and slow (τ2) relaxation regimens were obtained during fitting procedure (**C**).

The corresponding stress, as shown in figure 4.5-B, reaches about 7 μN per each CS. As a result, the CS recovered from the applied stress in a double exponential decay. All the spheroids showed a similar relaxation pattern consisting of a rapid elastic relaxation followed by a slow viscous dissipation (see Figure 4.5-B) rather than a single exponential decay. This phenomenon is known from studies on other microtissues and has already been discussed in a pioneering work carried out via micropipette aspiration [10].

Two relaxation constants (τ1 and τ2) are extrapolated by least-square fitting. The exemplificative distribution is shown in figure 4.5-C. The first relaxation (τ1) occurs in a time of (0.747 ± 0.153) s, (0.521 ± 0.056) s, (0.685 ± 0.073) s for SPH1, SPH2, and SPH3 respectively (Mean ± SD). The second relaxation occurs in a time (τ2) of (9.22 ± 1.45) s, (9.26 ± 0.61) s, (9.59 ± 0.57) s. Both τ1 and τ2 show a SD less then 11%, apart from SPH1 for which it is higher (20% and 16%). As seen from the optical micrographs in figure

4.1-A, SPH1 appears to be slightly larger than the other two, while its external corona is less compact. It can be hypothesized that the mechanical interactions between the embedded cells differ from the other spheroids because of its apparent looser architecture, resulting in relaxation times which in turn are more dispersed. Moreover, the compression section of the SR plots ("*Stress*" in Figure 4.5-B, first 500 ms of red curves) tells us SPH1 is softer because of the reduced slope, which agrees with the optical evaluation and the longer relaxation times.

4.5 Macro probes to stimulate CSs contractility

Interestingly, in the beginning, CS did not spontaneously contract. However, they started to, after a few SR cycles (see figure 4.6-A). This finding is consistent with the concept of the heart mechano-electric feedback, which tells an electrical current leads to a contraction, but the oppo-site is also true, giving rise to a feedback loop thanks to which a forced contraction often induces an autonomous one [24]. In a recent work [25], the same effect was observed on human-derived self-beating spheroids. Nakano and co-workers were able to uniaxially compress individuals and pairs of CSs and monitor their electromechanical coupling under parallel plates, via creep measurements. They also showed how CS work both under and against mechanical load, and how their beating frequency is influenced by the applied static force. The upper plate of their system was connected to a calibrated spring whose compression was monitored by optical microscopy. We reproduced Nakano's experiment on our spheroids using our macro-cantilevers which offer, thanks to the AFM configuration, a much better force and position sensitivity and faster time responses. Instead of creep experiments, we applied a set of mechanical stimulations via the AFM macro-probe to the CSs. By inducing 10 cyclic compressions (650 ms, 50 μm displacement setpoint), we could induce a transient beating and, at the same time, evaluate the beating pattern. Graphics in figure 4.6-B represent an example of this experiment performed on SPH1 after the SR. The faded portion of the plot (first ~ 7 seconds) shows the cyclic compressions, while the rest of the plot shows the passive force monitoring of the CS

transient beating, i.e., the vertical deflection of the cantilever over time, while the CS is displacing it upwards by its contractions.

After 4-5 contractions, SPH1 stopped beating and needed another cycle of micro-CPR to beat again, probably because the cardiomyocytes had already reached a significant

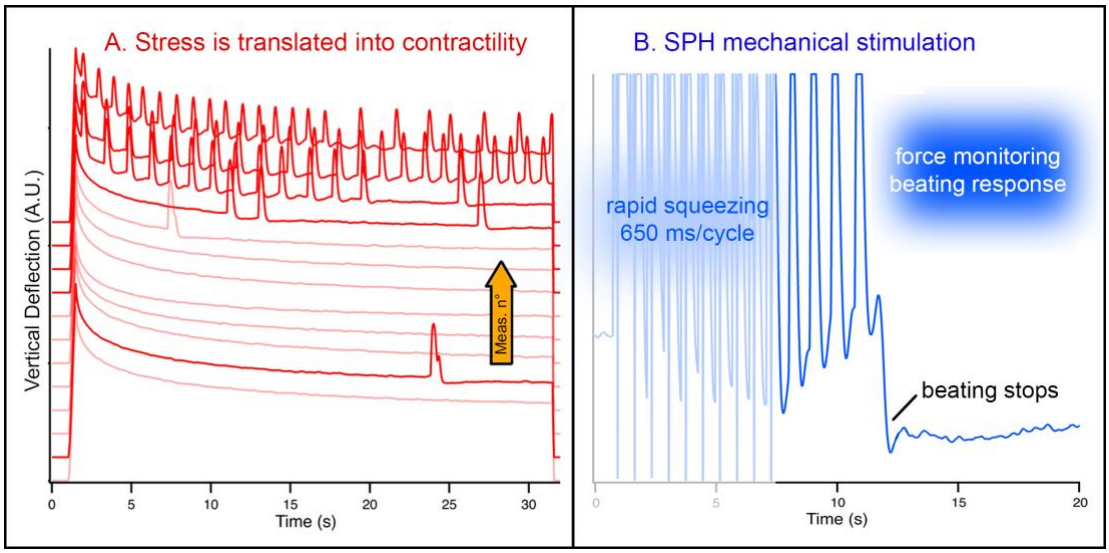

Figure 4.6, A. Inactive spheroids started beating after a few SR cycles translating a mechanical stimulus to autonomous contractility. Yellow arrow indicates progressiveness in measurement number (from 1 to 12, for SPH1). Each curve is vertically displaced by 1 A.U. to discriminate the single measurement. **B.** shows the effects of a controlled stimulation on SPH1, resulting into transient contractility from ~ 7 to ~ 12 seconds.

maturation level at P3 (plus 4 days in culture). Since our probes' spring constant is known, we could also have performed the mechanical loading using a force setpoint instead of a z-displacement one. We regard this as a prominent detail since it would allow investigating the CS response at different loading forces. We refer to this kind of experiment as "micro-CPR" because of the analogy to the human cardiopulmonary resuscitation applied as chest compressions.

In summary, our system could greatly help explore the results of prolonged mechanical stimulation on the CS development, albeit we should consider the need for a biological environment for the CSs to survive for a long time. For this purpose, a redesign of the macro-probe would be essential to be fully integrated - for example - into a cell culture incubator. In this framework, its operation would have to be decoupled from the AFM machine, e.g., by integrating a piezoelectric circuit on its legs as a sensing element (to measure its deflection) and a piezoelectric tube as a displacement actuator (to tune its vertical load).

References

[1] L. Polonchuk, M. Chabria, L. Badi, J.C. Hoflack, G. Figtree, M.J. Davies, C. Gentile, Cardiac spheroids as promising in vitro models to study the human heart microenvironment, Sci. Rep. 7 (2017). doi:10.1038/s41598-017-06385-8.

[2] R. Noguchi, K. Nakayama, M. Itoh, K. Kamohara, K. Furukawa, J.-I. Oyama, K. Node, S. Morita, Development of a three-dimensional pre-vascularized scaffold-free contractile cardiac patch for treating heart disease, J. Hear. Lung Transplant. 35 (2016) 137–145. doi:10.1016/j.healun.2015.06.001.

[3] S. Mattapally, W. Zhu, V.G. Fast, L. Gao, C. Worley, R. Kannappan, A. V. Borovjagin, J. Zhang, Spheroids of cardiomyocytes derived from human-induced pluripotent stem cells improve recovery from myocardial injury in mice, Am. J. Physiol. - Hear. Circ. Physiol. 315 (2018) H327–H339. doi:10.1152/AJPHEART.00688.2017/SUPPL_FILE/SUPPLEMENTAL.

[4] P. Beauchamp, C.B. Jackson, L.C. Ozhathil, I. Agarkova, C.L. Galindo, D.B. Sawyer, T.M. Suter, C. Zuppinger, 3D Co-culture of hiPSC-Derived Cardiomyocytes With Cardiac Fibroblasts Improves Tissue-Like Features of Cardiac Spheroids, Front. Mol. Biosci. 7 (2020) 14. doi:10.3389/FMOLB.2020.00014/BIBTEX.

[5] A.C. Daly, M.D. Davidson, J.A. Burdick, 3D bioprinting of high cell-density heterogeneous tissue models through spheroid fusion within self-healing hydrogels, Nat. Commun. 2021 121. 12 (2021) 1–13. doi:10.1038/s41467-021-21029-2.

[6] L. Polonchuk, L. Surija, M.H. Lee, P. Sharma, C.L.C. Ming, F. Richter, E. Ben-Sefer, M.A. Rad, H.M.S. Sarmast, W. Al Shamery, H.A. Tran, L. Vettori, F. Haeusermann, E.C. Filipe, J. Rnjak-Kovacina, T. Cox, J. Tipper, I. Kabakova, C. Gentile, Towards engineering heart tissues from bioprinted cardiac spheroids, Biofabrication. 13 (2021). doi:10.1088/1758-5090/AC14CA.

[7] K. Andrysiak, J. Stępniewski, J. Dulak, Human-induced pluripotent stem cell-derived cardiomyocytes, 3D cardiac structures, and heart-on-a-chip as tools for drug research, Pflügers Arch. - Eur. J. Physiol. 2021 4737. 473 (2021) 1061–1085. doi:10.1007/S00424-021-02536-Z.

[8] R.C. Boot, G.H. Koenderink, P.E. Boukany, Spheroid mechanics and implications for cell invasion, Https://Doi.Org/10.1080/23746149.2021.1978316. 6 (2021). doi:10.1080/23746149.2021.1978316.

[9] V. Vyas, M. Solomon, G.G.M. D'Souza, B.D. Huey, Nanomechanical Analysis of Extracellular Matrix and Cells in Multicellular Spheroids, Cell. Mol. Bioeng. 12 (2019) 203–214. doi:10.1007/S12195-019-00577-0/FIGURES/6.

[10] K. Guevorkian, M.J. Colbert, M. Durth, S. Dufour, F. Brochard-Wyart, Aspiration of biological viscoelastic drops, Phys. Rev. Lett. (2010). doi:10.1103/PhysRevLett.104.218101.

[11] D. Jaiswal, N. Cowley, Z. Bian, G. Zheng, K.P. Claffey, K. Hoshino, Stiffness analysis of 3D spheroids using microtweezers, PLoS One. 12 (2017). doi:10.1371/JOURNAL.PONE.0188346.

[12] N. V. Kosheleva, Y.M. Efremov, B.S. Shavkuta, I.M. Zurina, D. Zhang, Y. Zhang, N. V. Minaev, A.A. Gorkun, S. Wei, A.A. Shpichka, I.N. Saburina, P.S. Timashev, Cell spheroid fusion: beyond liquid drops model, Sci. Reports 2020 101. 10 (2020) 1–15. doi:10.1038/s41598-020-69540-8.

[13] A. Mgharbel, H. Delanoë-Ayari, J.P. Rieu, Measuring accurately liquid and tissue surface tension with a compression plate tensiometer, Https://Doi.Org/10.2976/1.3116822. 3 (2010) 213–221. doi:10.2976/1.3116822.

[14] R. Yanbarisov, Y. Efremov, N. Kosheleva, P. Timashev, Y. Vassilevski, Numerical modelling of multicellular spheroid compression: Viscoelastic fluid vs. viscoelastic solid, Mathematics. 9 (2021). doi:10.3390/MATH9182333.

[15] L. Andolfi, S.L.M. Greco, D. Tierno, R. Chignola, M. Martinelli, E. Giolo, S. Luppi, I. Delfino, M. Zanetti, A. Battistella, G. Baldini, G. Ricci, M. Lazzarino, Planar AFM macro-probes to study the biomechanical properties of large cells and 3D cell spheroids, Acta Biomater. 94 (2019) 505–513. doi:10.1016/j.actbio.2019.05.072.

[16] M. Zanetti, S.N. Chen, M. Conti, M.R.G. Taylor, O. Sbaizero, L. Mestroni, M. Lazzarino, Microfabricated cantilevers for parallelized cell-cell adhesion measurements, Eur. Biophys. J. (2021). doi:10.1007/S00249-021-01563-Z.

[17] W.L. Stoppel, D.L. Kaplan, L.D. Black, Electrical and mechanical stimulation of cardiac cells and tissue constructs, Adv. Drug Deliv. Rev. 96 (2016) 135. doi:10.1016/J.ADDR.2015.07.009.

[18] M.P. Stewart, A.W. Hodel, A. Spielhofer, C.J. Cattin, D.J. Müller, J. Helenius, Wedged AFM-cantilevers for parallel plate cell mechanics, Methods. 60 (2013) 186–194. doi:10.1016/J.YMETH.2013.02.015.

[19] J.L. Hutter, J. Bechhoefer, Calibration of atomic-force microscope tips, Rev. Sci. Instrum. (1993). doi:10.1063/1.1143970.

[20] P. Simpson, S. Savion, Differentiation of rat myocytes in single cell cultures with and without proliferating nonmyocardial cells. Cross-striations, ultrastructure, and chronotropic response to isoproterenol, Circ. Res. 50 (1982) 101–116. doi:10.1161/01.RES.50.1.101.

[21] C.S. Long, K. Kariya, L. Karns, P.C. Simpson, Sympathetic modulation of the

cardiac myocyte phenotype: studies with a cell-culture model of myocardial hypertrophy, Basic Res. Cardiol. 87 Suppl 2 (1992) 19–31. doi:10.1007/978-3-642-72477-0_3.

[22] V. Martinelli, G. Cellot, A. Fabbro, S. Bosi, L. Mestroni, L. Ballerini, Improving cardiac myocytes performance by carbon nanotubes platforms, Front. Physiol. 4 SEP (2013) 239. doi:10.3389/FPHYS.2013.00239/BIBTEX.

[23] R. Foty, A simple hanging drop cell culture protocol for generation of 3D spheroids, J. Vis. Exp. (2011). doi:10.3791/2720.

[24] P. Kohl, U. Ravens, Cardiac mechano-electric feedback: Past, present, and prospect, in: Prog. Biophys. Mol. Biol., 2003: pp. 3–9. doi:10.1016/S0079-6107(03)00022-1.

[25] K. Nakano, N. Nanri, Y. Tsukamoto, M. Akashi, Mechanical activities of self-beating cardiomyocyte aggregates under mechanical compression, Sci. Reports 2021 111. 11 (2021) 1–10. doi:10.1038/s41598-021-93657-z.

Chapter 5

Rheological properties of fibrotic cardiospheres measured by whole-spheroid stress-relaxation.

5.1 Introduction

It is well known that the ventricular function is greatly influenced by the myocardium's mechanical properties [x], and a growing amount of research recently pointed out the existence of hysteresis in its stress-strain relationship [x], calling for a broad investigation of its passive viscoelastic behavior. Indeed, the ventricular free wall displays an anisotropic and viscoelastic rheological behavior, meaning that its mechanical properties change along different directions, presenting both elastic and viscous properties while being deformed [x]. Such viscoelasticity has been investigated at different scales, using distinct techniques. Compression and pulling tests, for example, were performed onto centimeter and millimeter-sized fresh explants, showing a nonlinear stress-strain behavior [x]. The knowledge of such mechanical signature of the heart lays the foundations for a more accurate investigation of pathologies such as MF. Indeed, in vitro disease modeling allows to study MF effects on the heart tissue on a functional level, therefore helping to develop new treatments for it.

Recently, CSs were introduced as simple in vitro 3D models to study the heart microenvironment. Their cell population can be adjusted by including different ratios of multiple cell types, such as cardiomyocytes, fibroblasts, and endothelial cells. CSs were grown as a mixture iPSC-derived cardiomyocytes, human primary endothelial cells, and human primary fibroblasts, using the same ratios as the in-vivo heart tissue [x]. Such biological engineering has shown to mimic important features of human heart morphology. In a similar study, [x] hanging drop mixed 3D cultures of neonatal rat ventricular myocytes (NRVMs), and their non-myocyte counterparts, were created. The resulting CSs were than treated with transforming growth factor beta 1 (TGFβ1), a known profibrotic agent [x], causing a dramatic increase in collagen deposition as well as elevated expression levels of fibronectin and connective tissue growth factor.

Although these basic 3D models already demonstrated their effectiveness in reproducing the intricate microenvironment of MF, the assessment of their viscoelastic properties remains a significant technological challenge, mainly because of their size (from 100 μm, up to a millimeter in diameter). As previously discussed, macro-scale techniques are effective in characterizing the rheological properties of tissue biopsies

and ex-vivo tissue explants. Conversely, micro and nanoscale techniques such as AFM are well suited to study viscoelasticity at the single-cell level, and below. To bridge this gap, we have previously shown how it was possible to perform AFM-based parallel plate compression by using custom-fabricated macro cantilevers on NRVM CSs, that enabled to perform stress-relaxation tests.

In the present work, we exploited this approach to evaluate the viscoelasticity of co-cultured CM/CF spheroids. We assembled three distinct types of cardiac spheroids (CSs) using three different ratios of cardiac cells. The rationale behind was to investigate the effects of increased fibroblast densities (CFs) on the mechanical properties of CSs, evaluating the viscoelastic features of in vitro fibrotic CSs.

5.2 Experiment pipeline

5.2.1 Fibroblasts pre-activation on a 2D hard surface

The cell suspension resulting from NRVM the isolation procedure (as described in the previous chapter) was strained and pre-plated in two separate 96 mm ø polystyrene tissue culture dishes. After 45 min of pre-plating, > 90% of NRCFs adhered, and floating NRCMs were collected from the culture dish' suspension and replated in a separate, gelatin-functionalized dish, at 1 $\times 10^5$ cells/cm^2. Media was replaced every day for the following 4 days, before spheroids formation.

5.2.2 Mixed 3D cardiac spheroids assembly

NRCM and NRCF monolayers were washed with phosphate buffer saline (PBS) solution and detached by trypsinization over 5 min. Trypsin was neutralized with fresh media, the cells were counted, and CMs and CFs were collected in two separate 15 mL tubes and sedimented at 100 RCF, for 5 min. The supernatants were discarded, and each pellet was resuspended separately, at 2.5 $\times 10^6$ /mL in fresh media. For clarity, we will refer to these high-density cell suspensions as "stock CMs" and "stock CFs".

Three distinct types of cardiac spheroids (CSs) using three different ratios of cardiac cells were prepared. Starting from the four-day of 2D NRCMs and NRCFs CSs were created in three conditions: 50'000 CMs (100% cardiomyocytes, the control sample, namely CTRL), 35'000 CMs with 15'000 CFs (70% cardiomyocytes, intermediate fibrotic sample, namely F^+), and 25'000 CMs with 25'000 CFs (50% cardiomyocytes, advanced fibrotic sample, namely F^{++}). It is important to note these percentages do not necessarily reflect the amount of CMs inside the spheroid, but the mere number of cells coming from the NRCM plate with respect to the total number of cells used to obtain the spheroid.

By mixing 7 parts of stock CMs, and 3 parts of stock CFs, a 70% CMs high-density suspension was created. For the 50% CMs suspension, the mixing ratio between the two stocks was 1:1.

CSs were formed via the hanging drop method [x]. For that, 20 μL drops of either 100%, 70%, or 50% high-density cell suspensions were pipetted onto the inner side's lid of a 96 mm ø culture dish, forming at least ten drops per sample, spaced 1 cm apart

and containing approximately 50'000 cells each. Finally, the lid was rapidly flipped onto the dish' bottom, which had been previously filled with sterile PBS, thus leaving the drops hanging in a humidified environment. The cells in each drop assembled over the course of 4 days at 37°C, 5% CO_2, forming co-cultured CM/CF cardiac spheroids.

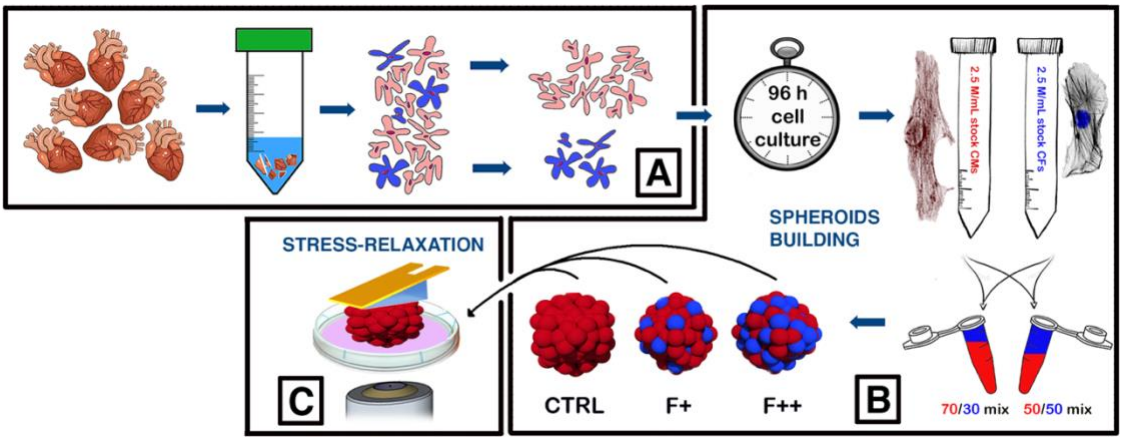

Figure 5.1. (A) Shows the experimental workflow, depicting tissue digestion and CM/CF isolation steps. **(B)** Shows the 4-days 2D cell culture of both cell phenotypes (summarized as a pocket watch), CM/CF mixing at different ratios, and co-culture spheroids assembly, up to the stress-relaxation tests done by AFM **(panel C).**

5.2.3 Immunofluorescence optical sectioning

A multichannel immunostaining was used to visualize the composition of CSs. Fibroblasts were labeled by targeting Vimentin (Vim), while cardiomyocytes by Sarcomeric α-Actinin (α-Act). First, the CSs were fixed in PFA 4% for 1 h and permeabilized for 1 h 30 min (Triton X-100, 1%) at RT. Epitopes were blocked using 1% BSA, 1 h at 4°C. Primary antibody staining was done overnight at 4°C using a mixture of mouse anti Sarcomeric α-Actinin or chicken anti Vimentin mAbs (Abcam®, 1:200 dilution) in blocking buffer. Secondary fluorescent antibodies (Alexa Fluor 488 anti-mouse, Cy5 anti-rabbit, Abcam®, 1:1000 dilution) were then incubated for 1 h 30 min at RT. To counterstain the nuclei 5 µM DAPI was used, and the spheroids were imaged using structured illumination microscopy (SIM).

For SIM, an Axio Observer Z1 inverted microscope with an ApoTome® module (1.6/1.5 transmission grid) and an AxioCam 506 monochrome camera were used (Carl Zeiss AG) to optically section spheroids through a 63x/1.4 EC Plan Neofluar oil immersion objective. Seven grid projection images were taken in 9-12 tiles at the lower, middle,

and upper Z-slices of the spheroid. The images were then reconstructed using ZEN black edition by performing ApoTome® deconvolution and tile fusion.

Starting from the optical sections, Vimentin (Vim, magenta) and Sarcomeric α-Actinin (α-Act, green) channels were isolated and separately thresholded using Fiji free sotware [x]. Then, three squared ROIs of 100'000 μm² each were randomly placed on three areas of the spheroids' outer boundary, accounting for a potentially uneven fluorophore penetration rate. The Vim-stained area was finally referenced to the aggregated stained area (i.e., the sum of Vim and α-Act-stained areas).

5.2.4 Estimation of CSs size

The optical images acquired prior to each stress-relaxation experiment (example in Figure 3, A) were imported into Fiji. For each spheroid, a circular ROI was manually drawn over its outer boundary. For slightly-elliptically shaped spheroids, an elliptical ROI was used. Then, each ROI's area was measured, and the diameter computed as:

$$d = 2 \cdot \sqrt{\frac{A}{\pi}}$$

Therefore, the elliptical spheroids were treated as they were spherical for the diameter estimation.

5.3 Mechanically activated fibroblasts proliferate in 3D

In this work, 3D spheroids were employed as in-vitro models to investigate the viscoelastic hallmarks of myocardial fibrosis. For such purpose, cardiomyocytes and fibroblasts were mixed at three different ratios, mimicking three distinct phenomena: a *physiological* tissue (CTRL), an intermediate MF (F^{+}), and an advanced MF (F^{++}). While a vast majority of studies on the CMs' *physiological* mechanical properties make use of pure cultures, a moderate presence of fibroblasts has been shown to support CMs networks in 3D [x]. In the present study, indeed, the pre-plating step was purposedly kept short (45 min), because our goal was to keep residuals CFs into the isolated CMs suspension. As the isolated CMs were aspirated, they were quickly replated at confluency (100'000 cells/cm^2), so residual fibroblasts had limited space to fill. Accordingly, as already mentioned, the theoretical percentage of CMs (100% for CTRL, 70% for F^{+}, and 50% for F^{++}) did not represent the real ratio of cardiomyocytes into the spheroid. Sections of the stained samples are shown in Figure 5.2-A.

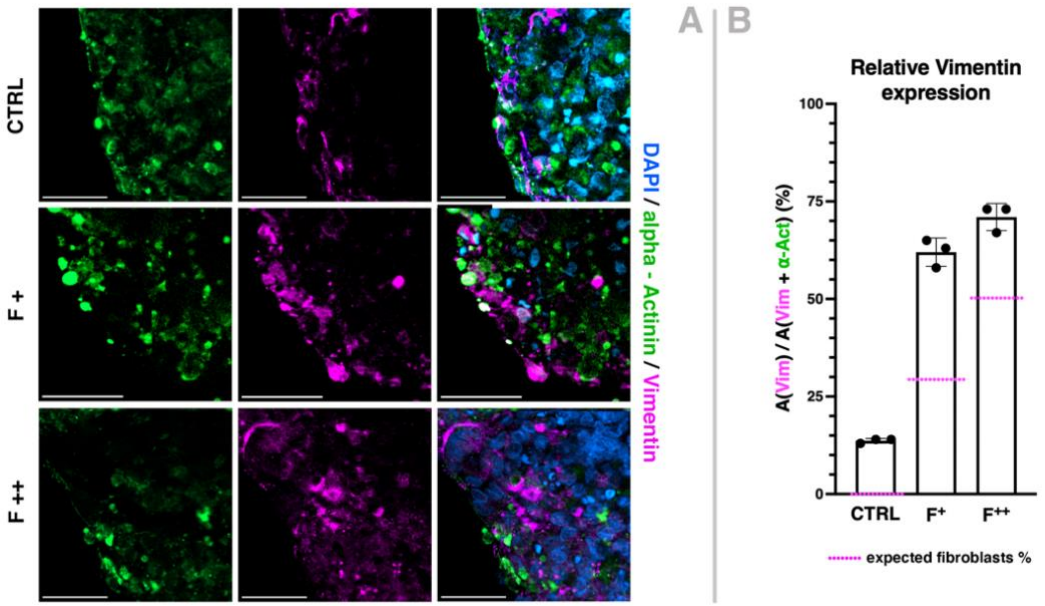

Figure 5.2. Panel (A) shows representative IF optical sections obtained by structured illumination microscopy in the case of physiological-like (**CTRL**), moderate fibrotic (**F +**) and advanced fibrotic (**F ++**) spheroids. DAPI-stained nuclei are shown in blue, α-Actinin positive cells (cardiomyocytes) are shown in green, Vimentin positive cells (fibroblasts) are shown in magenta. **Panel (B)** shows the relative stained area of Vimentin normalized by the total stained area (Vimentin + α-Actinin). Magenta dashed lines are the theoretical fibroblast amount, expressed as the theoretical percentage of fibroblasts as assembled into the spheroid (0, 30, and 50% for **CTRL**, **F +**, and **F ++,** respectively). Dots represent 100 x 100 μm averaged area counts, as taken from three distinct spheroids per each group. Bars at Mean, whiskers show SD.

The presence of vimentin-stained filaments inside the CTRL spheroid confirms what already introduced regarding CFs residues, and a progressive increase of CFs density into fibrotic spheroids. However, the exact number of fibroblasts cannot be drawn just from estimating the Vim-stained area, due to differences related to the physiology of each cell, so it would an unreasonable take to verify a proliferative behavior of CFs just by looking at that. The same logic can be applied while assessing the number of CMs. However, we can assume the number of CMs to not change significantly after seeding, due to their limited proliferative capabilities.

If the CMs population does not vary during time, in order to verify a proliferative behavior of CFs population we can use proportions. By comparing the Vim-stained area with the total amount of staining (Vim + α-Act), we estimated the ratio between fibroblast intermediate filaments and cardiomyocytes' sarcomeric proteins to dramatically increase above 60% for both fibrotic spheroid (Figure 5.2-B). This evidence may seem trivial at first, because fibrotic spheroids were obtained in the first place by deliberately mixing a higher number of CFs with respect to CMs. However, if the higher number of seeded CFs was the sole reason for the relative higher Vim expression, it would be hard to explain the reason why F^{+} shows a comparable Vim staining ratio of F^{++} (61% vs 71% respectively, see Figure 5.2-B), given that the latter was obtained using ~1.7x more fibroblasts and ~ 1.4% less cardiomyocytes than F^{+} (see magenta dashed lines in Figure 5.2-B). Therefore, especially for F^{+}, CFs must be proliferating inside the spheroid and actively producing more Vim.

Indeed, recent ex-vivo cases of ischemic heart disease [x] showed elevated Vim expression around myocardial cells undergoing remodeling. At the same time, a growing amount of research pinpoints how the mechanical interaction between cells and culture surface plays a crucial role in shaping the phenotypical transition of cells, by changing their mechanical and morphological properties [x,x,x,infinitilavori]. For example, primary rat fibroblasts have shown to incorporate pro-fibrotic αSMA into their stress fibers when cultured onto > 10 kPa substrates, as well as expressing higher levels of other pro-fibrotic markers such as PDGFRα, suggesting the need of a softer culture substrate to maintain their physiological features and prevent the transition to a pro-fibrotic phenotype.

In our work, we leveraged this otherwise detrimental mechanical interaction by pre-expanding the CFs population on a 2D stiff plastic surface, thus mechanically pre-activating the fibroblasts before the 3D CMs co-culture. Our experimental results demonstrate a proliferative stage inside F^+ CSs, suggesting that our multi-step 2D/3D approach represents a suitable workflow to induce the proliferative stage of MF in-vitro.

5.4 Size does not affect the measured viscoelasticity of CSs

After 4 days of hanging drop culture, fully formed spheroids were subjected to AFM stress-relaxation measurements In this case, the magnitude of the initially applied stress could influence the stress-relaxation behavior, and such magnitude also depends on the cellular and ECM composition of each spheroid. However, such inner composition influences the spheroid's size as well, because CMs and CFs differ in cellular volume while occupying a confined 3D space. CF and CM cultured on 2D surfaces display a flat geometry and spread out by hundreds of μm. On the contrary, they tend to be more rounded and compact while growing in supportive 3D matrices [x]. As cardiomyocytes mature and develop in a 3D culture, the activation of hypertrophic pathways leads to an increase in their cellular volume, so they eventually become larger than fibroblasts grown in the same culture conditions [x]. In fact, a reduced number of CMs in our fibrotic spheroids led to a volumetric shrinkage for both, as assessed by optical microscopy (see optical micrographs in Figure 5.3).

If we focus on the cell number alone, and assuming that the CMs number remains constant from cell seeding, while activated CFs proliferate at similar rates among the groups, we would expect a progressive decrease in volume, with the control group being the largest, followed by F^{+}, and then F^{++}. However, while the spheroid's diameter is significatively greater for the control group (362 ± 30) μm compared to (284 ± 17) μm for F+ and (282 ± 36) μm for F++, the fibrotic CSs show no significant size differences between each other. This could be due to an increased fibroblast proliferative drive in F++, or a greater ECM deposition in the same, both of which are hallmarks for MF as previously discussed.

The size variability among the spheroids can have a significant impact on their viscoelastic properties. In fact, the initial applied stress is not only influenced by the composition of the biological material and the constant Z-piezo displacement, but also by the volume of the spheroid itself. Indeed, if we keep the same Z-displacement, a larger spheroid would eventually be less stressed than a smaller one. To control for this factor, a correlation analysis was performed to examine the relationship between the relaxation times (τ1 and τ2 as calculated from the fitting procedure) and the diameter of the spheroid across all groups. Both τ1 and τ2 showed to be neither positively nor negatively correlated with the spheroid's diameter (see Figure 5.3-B). The absence of correlation between the measured viscoelastic decays and the spheroid's diameter further confirms that our AFM-based approach investigates the CS viscoelasticity without being remarkably affected by the spheroid size, at least in the 200-400 μm range.

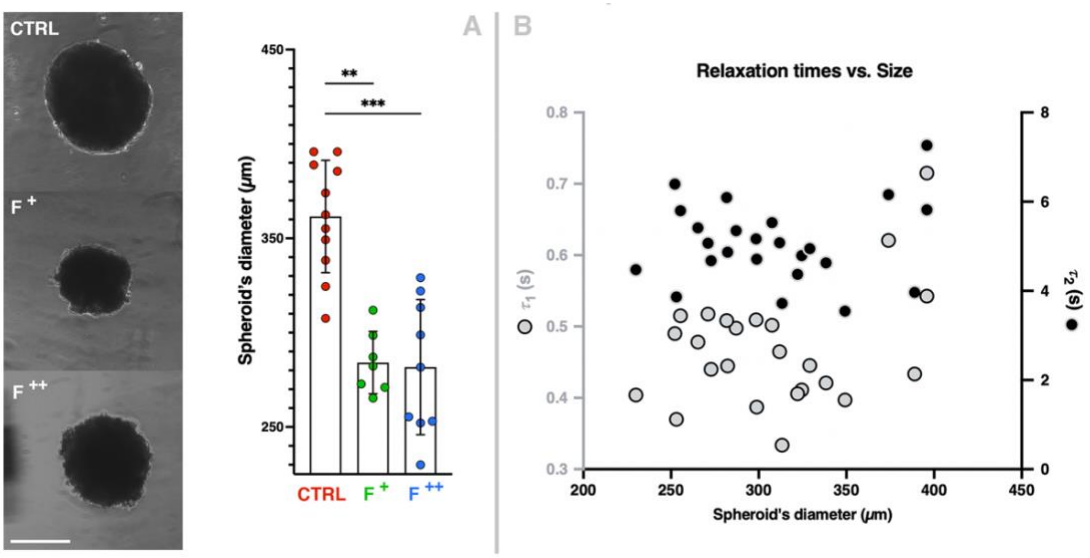

Figure 5.3. Panel A shows three representative optical micrographs of the spheroids, and the diameter distribution of the CTRL, +, and F++ populations, which are statistically different as shown by pairwise nonparametric Dunn's test (p = .0019 for CTRL vs F+, and p = .0007 for CTRL vs F++). Bars represent Mean, whiskers represent SD). **Panel B** shows the first and second relaxation times (each dot represents a spheroid) plotted against the spheroid diameter. No correlation of either first or second relaxation times with the spheroid diameter was observed through Spearman's rank order correlation statistics. Spearman's r(22) = .11, p = .60, 95% CI [- 0.32, 0.50] and Spearman's r(22) = - .027, p = .90, 95% CI [- 0.44, 0.39] for τ1 and τ2 respectively.

5.5 Viscoelasticity is altered in MF spheroids

We observed the stress-relaxation to follow a two-phase decay, characterized by a quick viscoelastic recovery that lasted up to a second, followed by a slower viscoelastic dissipation. Such behavior has been previously observed in our studies on hanging-drop cultured cardiomyocytes [Io], tumor spheroids [Laura], and oocytes [Alice]. Moreover, this two-regimen viscoelastic decay has been already observed using other methods on similar viscoelastic drops, such as micropipette aspiration on spheroids made of other cells rather than cardiac ones [x]. Accordingly, by fitting the generalized Maxwell model, two distinct relaxation times were obtained (Figure 5.4-A).

Both relaxation times show a lowering trend in the case of fibrotic spheroids, when compared to control (Figure 5.4-B/C) and such trend was statistically different for τ_1 (Figure 5.4-B)

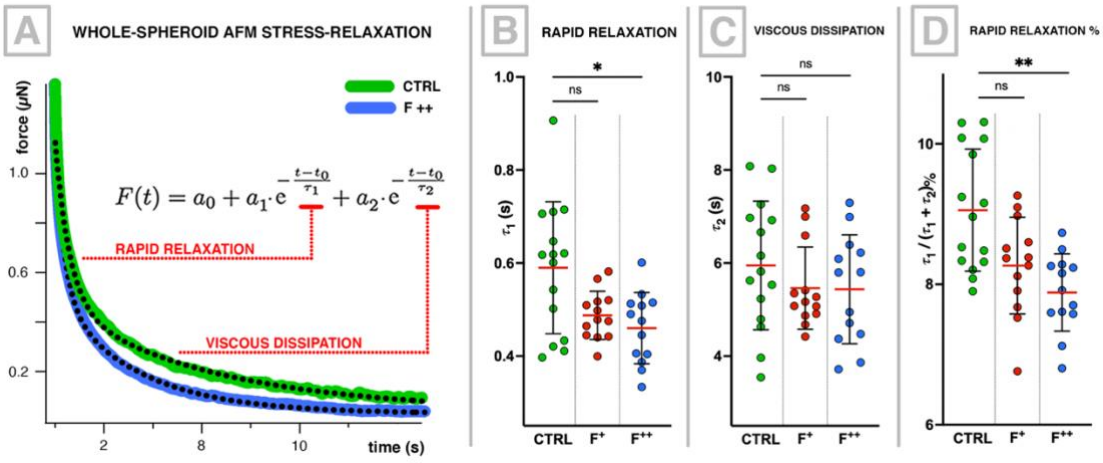

Figure 5.4. Panel (A), two exemplificative AFM relaxation curves of a CTRL (green) and advanced fibrotic F++ (blue) spheroids. Only the first 15 s are shown, to further highlight the trend variation. Dashed lines are the fit curves as obtained through least-square fitting of the two-component Generalized Maxwell model (see equation), used to extrapolate the rapid elastic relaxation time (τ_1), and the longer viscous dissipation time (τ_2). **Panel (B)** shows each spheroid's first relaxation time per each condition, CTRL vs F++ times are statistically different (p = .0157). Panel **(C)** shows the same as (**B**), but for the second relaxation time. Panel **(D)** shows the same as **(B/C)**, but for the ratio of the first divided by the sum (1+2) of both relaxations. CTRL vs F++ ratios are statistically different (p = .0012). **(B/C/D)** statistics were carried out by Dunn's nonparametric pairwise comparison. Dots represent a single measured spheroid (green for CTRL, red for F+, and blue for F++). Red lines at Mean, black whiskers are SDs.

Taken together, these results indicate a lower relaxation time for both rapid relaxation and viscous dissipation regarding fibrotic F^{+} and F^{++} spheroids. It is widely known that MF causes stiffening of the heart muscle [x,x,x,infiniti] and thus lower relaxation times

[x]. Here, by shaping the myocardium into a multicellular spheroid and approximating its rheological behavior to a pure viscoelastic material, we found a similar trend by mechanically loading such in-vitro microtissue. We must clarify that a sudden initial recovery does not imply the complete absence of a viscous behavior, as τ_1 is always dependent by the ratio between viscosity (η) and Young's modulus (E), which are mechanical properties intrinsic to the material. In the case of τ_1, η_1 and E_1 represent the viscosity and the stiffness (respectively) of those biological structures that rapidly rearrange during the first moments after the sudden deformation. In a pioneering study by G. Forgacs et al. [x], the same bimodal relaxation was observed on embryonic fragmented heart tissue subjected to parallel-plate compression (even if over a longer experimental timescale). Forgacs interpreted τ_1 as verbatim "the time scale characterizing the relaxation of the more or less elastic deformation of each individual cell in the aggregate, together with whatever extracellular matrix molecules might be present".

As already discussed, activated myofibroblasts are proliferating in intermediately fibrotic loci undergoing remodeling, which is a condition we modeled within the intermediately fibrotic spheroids (F^+). In diffuse fibrotic loci, myoFbs actively synthetize even more Col I. While further investigation is required by our side to confirm Col dynamics inside co-cultured CSs, we can hypothesize F^{++} samples contained the more secreted collagen, as the CF population were much greater than in the control, and CMs do not generally regulate collagen deposition inside the heart [x]. While Col I provides rigidity to the myocardium [x], Col III contributes to its elasticity [x]. During fibrosis, Col I deposition increases more apparently than Col III, therefore misbalancing Col I/III ratio and elevating myocardial stiffness and ventricular wall tension [x]. In our MF model, an elevated tension is easily explained by the significant reduction in τ_1 relaxation time for F^{++}, which represents the sudden elastic recovery sustained by the spheroid right after its deformation. In fact, an elevated stiffness means a higher Young's modulus. The higher E_1, the lower τ_1 will be. Therefore, we could associate the observed τ_1 reduction to an increased collagen density caused by activated fibroblasts.

To estimate the magnitude of such collagen variations in-between groups, τ_1 was referenced to the total relaxation time (i.e., $\tau_1 + \tau_2$) as shown in Figure 5.4-D. As result, the relative effect is even more pronounced, with the elastic recovery time accounting for 7.88 ± 0.55% of the total measured relaxation time in the case of F^{++}, and a greater percentage of 9.04 ± 0.9% in the case of the control. Relatively, less time was required for fibrotic spheroids to rearrange the elastic components to their original shape. Indeed, a spring with a higher stiffness will have a shorter springback time (i.e., it will rewind quickly). This highlights the importance of τ_1 in the discrimination between physiological and fibrotic spheroids, further confirming a mechanical imbalance between the two.

As the initial stress is quickly dissipated, it is followed by a long viscous response, which is characterized by the longer relaxation time τ_2. During this stage, cells must rearrange to adapt to the newly confined space. To do so, they are required to break and reform their adhesive contacts like the ones sustained by integrins and cadherins [x]. Looser adhesive contacts will reflect to a lower adhesion energy and, therefore, to a shorter viscous relaxation time. Even though we did not address specifically the adhesive molecules in our experiment, integrins and cadherins are known for being more expressed in fibrotic tissue [x]. Therefore, the trend we have found for τ_2 is paradoxical, as we would have expected longer dissipation times for fibrotic spheroids, given the hypothetical greater adhesion between cells. Nevertheless, it must be considered that τ_2 distributions are more dispersed throughout all groups and this is also why no statistical significance has been observed among them (Figure 4, C). Moreover, while τ_1 have been associated to the fast recovery of the elastic components of cells and ECM, and τ_2 to the cellular adhesive remodeling, we should avoid oversimplifying these two parameters by minimizing them to a discrete overview. If the elastic components and the adhesive viscous ones were affecting this bimodal decay exclusively, there should be no correlation between τ_1 and τ_2. However, a strong positive correlation between τ_1 and τ_2 is found by Spearman's rank-order test, $r(39) = .88$, $p < 0.0001$, 95% CI [0.78, 0.94]. Indeed, multicellular spheroids are complex heterogenous structures, and their whole mechanics results from a synergic combination of a multitude of mechanical factors at different hierarchies.

5.6 References

Chapter 6

Passive electromechanical conditioning improves 3D cardiospheres contractile performance

6.1 Introduction

In the past few decades, tremendous progress towards regenerating various tissues and organs has been made [x]. Cardiac regeneration is of particular interest as it bears the potential to treat and even reverse the debilitating effects of heart failure, a leading cause of death worldwide according to WHO [x]. However, *bona fide* regeneration of the heart remains an unmet ambition. Five heart regeneration hallmarks [x] have been recently identified in a holistic rationale by Bertero and Murry, by analogy to what had been previously proposed by the classic paper from Hanahan and Weinberg regarding cancer biology [x]. Bertero and Murry argue that a true cardiac reconstitution must obtain a proper remuscularization, fibrosis resolution, immunological balance, angiogenesis, and electromechanical stability. Concerning the latter, newly regenerated cardiomyocytes must achieve adult-like properties of their excitation-contraction coupling machinery and need to reach a deep interconnection with the hosting tissue's electrical topology [x]. Recent breakthroughs in somatic cell reprogramming have enabled the development of human induced pluripotent stem cell-derived cardiomyocytes (hPSC-CMs), which are genetically identical to the patient, ultimately reducing the risk of immune response after transplantation [x]. However, hiPSC-CMs are often immature as shown, for example, by their spontaneous contractile cycles, which led to sustained ventricular arrhythmias into non-human primates previously transplanted with such cells [x]. It follows that investigating new strategies to improve cardiomyocytes' maturity is crucial for regeneration purposes, such as in-situ repopulation or even organ bioprinting, but also to produce better in vitro models for disease modeling and drug testing.

A mature cardiac tissue results from the delicate balance between electrical communication, mechanosensing, and mechanotransduction [x]. Such intricate interplay is one of the reasons why cardiac regeneration is a field thriving at the intersection of a wide range of disciplines, including cellular biology, biophysics, and tissue engineering. hiPSC-CMs are a powerful tool for studying cardiac maturation, but they are not easy to obtain, as they require a multi-step differentiation process which can take a significant amount of time [x]. Moreover, as they need to be cultured in specific conditions (such as antibiotic-free media), they are a sensitive culture to

maintain [x]. On the contrary, neonatal rat cardiomyocytes (NRVMs) are easy to work with [x], and still display immature features such as a moderate proliferative drive, making them an ideal alternative model for in vitro cardiac maturation and mechanosensing studies.

As mechanosensation thrives in three 3D, a 3D environment is needed to let the cardiomyocytes develop more naturally [x]. CSs are 3D spheroidal structures that are easily built to match this prerequisite. As described in Chapter 4, we cultured CSs made of NRVMs and performed precisely tuned stress-relaxation SR tests via AFM. Being initially interested in their viscoelastic relaxation, we also found that CSs progressively delivered synchronous contractions after an initial set (5-10) of mechanical loadings. In a similar work, performed on iPSC-CSs, Nakano and co-workers [x] studied the mechanical effects of uniaxial creep, delivered by parallel plate rheology, showing how compression tended to strengthen and stabilize the synchronous beating [x]. Our results and Nakano's were not coincidental, and suggest that mechanical conditioning is an indispensable control parameter when evaluating the beating activities of CSs.

Here, we further discuss how such mechanical conditioning should not be limited to the very last moments of a CS growth but should persist as a supporting background variable during all its maturation phases. In light of what has been discussed, to sustain their contraction machineries, CSs needs to grow in an environment promoting their electromechanical stability. Such environment should be mechanically compliant, while also providing proper electrical cues to ease membrane potentials' propagation and enhance intercellular connectivity.

Hydrogels are polymers that absorb large amounts of water, making them soft and pliable. They have been used in a variety of medical applications, including drug delivery [x] and tissue engineering [x]. Generally, they are electrical insulators [x]; however, they can be covalently functionalized with various nanomaterials that conduct electricity, being them metallic [x], or carbon-based [x]. These nanomaterials create pathways for electrical current to flow through the hydrogel, making it a conductor. Conductive hydrogels are ideal candidates to grow electroactive cells, such as neurons or cardiomyocytes, as they facilitate the propagation of intercellular ion

currents [x]. Moreover, their stiffness can be tuned to provide mechanical compliance for the cells to grow in, which is in line with what has been discussed above.

Previously, we have created a copolymer made of poly(serinol hexamethylene urea)-co-poly(N-isopropylacrylamide), which displays a reverse phase transition, i.e., it phase transitions from sol to gel when heated above ~ 35 °C, and then reverses its phase back below this temperature. This reverse thermal gel (RTG) [x] was initially designed with a precise goal in mind, i.e., to be easily injectable, and to provide structural support for regeneration once on an infarcted site. Moreover, such RTG has been functionalized with lysine (RTG-K), thus adding several free amine groups for functionalization, paving the way for a wide variety of bio-conjugations. In previous works, we covalently conjugated to such free amine groups two types of nanostructures: carboxyl-functionalized carbon nanotubes (CTNs-COOH) [x] or gold nanoparticles (AuNPs-COOH) [x] thereby boosting the RTG electrical conductivity. RTG-CNT and RTG-AuNP already demonstrated superior performances in supporting the growth of neonatal rat ventricular myocytes (NRVMs) [x,x], offering both mechanical and electrical stability to the cultured cells.

In this work, the RTG-AuNP gel was chosen as scaffold to exert an electro-mechanical conditioning during the cardiac spheroid growth. The spheroids released from the gel demonstrated higher maturation than the unconditioned control spheroids. Moreover, when they were subjected to whole-spheroid uniaxial cyclic compression by AFM macro-probes, the NRVM CSs demonstrated improved cardiomyocytes' beating synchronicity and higher beating forces.

This work highlights the critical role of the electro-mechanical conditioning as an important engineering strategy towards novel physiological-like environments for cardiomyocytes' maturation.

6.2 Maturation into AuNP nanoengineered RTGs

6.2.1 RTG – AuNP functionalization

Gold nanoparticles (AuNPs) were produced by wet chemistry as previously described [x] and were coupled to RTG-lysine (RTG-K), which was synthesized as described in previous works [x,x]; 10 nM of AuNPs-COOH were dissolved in 15 mL of phosphate-buffered saline (PBS). Carboxyl groups were activated at RT for 15 min using five molar excesses of 1-(3-dimethylaminopropyl)-3-ethylcarbodiimide hydrochloride/N-hydroxysuccinimide. After that, 5 mL of RTG-K solution (in PBS at 0.1 g/mL) was dropped in, and the reaction was carried out at RT for 48 h. The RTG-Au polymer was then dialyzed, lyophilized, and re-treated with L-lysine to neutralize any unreacted -COOH groups, as previously described [x]. The polymer was dialyzed again, cleaned through a 2 μm filter, and finally lyophilized.

6.2.2 Preparation of RTG solutions

We estimated a volume of 25 μL per each sample being large enough to accommodate a single spheroid while ensuring a stable gas diffusion and nutrients exchange. RTG solutions (RTG-K and RTG-Au) were prepared by dissolving the lyophilized polymer in cold complete media at a 1.5% w/v concentration inside a 1.5 mL microcentrifuge tube. The polymer solution was briefly vortexed, exposed to UV irradiation over 1 h, and finally stored at 4°C before the spheroid encapsulation.

6.2.3 NRVMs spheroids assembly and encapsulation

A 96 well, round bottom, ultra-low attachment plate (Corning Inc.) was conditioned with 100 μL of fresh media per each well by keeping it in the incubator for 30', prior to cell seeding.

50 μL of the concentrated NRVM suspension was then pipetted into each well, resulting in 50'000 cells per well. The plate was centrifuged at low speed (100 RCF) to aggregate the cells on the bottom, and finally placed into the incubator on a 3D shaker orbiting at 60 RPM. These two final steps were pivotal to avoid any leftover fibroblast attaching on the well surface, and to facilitate the spheroid aggregation over the course of the next 4-5 days.

After 4 to 5 days, cardiac spheroids were formed to be encapsulated into the RTGs. For this purpose, the RTG solutions were warmed up to RT, and the exhaust media was carefully discarded from the multiwell plate. Then, each spheroid was resuspended in a 25 μL drop of RT polymer solution into the well itself, and the plate was kept at 37 °C for the next 30 min. Meanwhile, a ceramic hot plate was used to keep at ~37 °C a layer of metallic thermal beads which served as a heating pad for the following step. After 30 min, the RTGs were completely gellified. The plate was rapidly transferred on the heating pad, and ~150 μL of warm media was slowly dropped into each well. At this stage, most of the gels detached from the plate's bottom and were found floating. The increased surface area exposed to the surrounding media furtherly facilitated nutrient and gaseous exchange. The samples were finally cultivated in the incubator up to 21 days, refreshing media every other day. Figure 6.1, A shows a schematic overview of the hydrogel conditioning experiment.

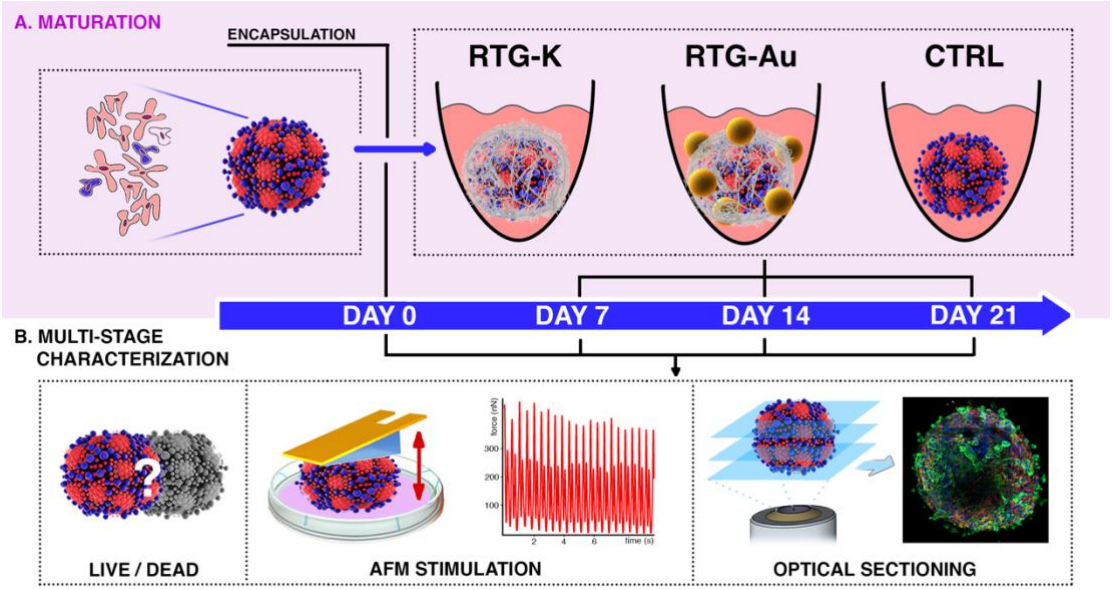

Figure 6.1 A) Overview of the experimental procedure, showing the hydrogel-conditioned maturation. Blue cells represent residual fibroblasts. Red cells represent cardiomyocytes. **B)** shows the multi-stage characterization carried out on the spheroids right before encapsulation (day 0), and after their release from RTGs at day 7, 14, and 21.

6.3 Multi-stage characterization of CSs

Figure 6.1, B shows the multi-stage characterization scheme performed before incubation, and after 7, 14, and 21 days of RTG electromechanical conditioning.

6.3.1 NRVMs Spheroids release from gel

After 7, 14, and 21 days of maturation, five to ten samples per each condition (that is, spheroids encapsulated into either RTG-K or RTG-AuNP gels) were taken out from the incubator and left at RT waiting for the gel to transition back to its sol state. To further clean the spheroids from any gellified aggregate, the entire content of the well was pipetted into a 96 mm ø dish filled with fresh media. This led to an immediate drop of the gel concentration, solubilizing any leftover RTG and thus making the free spheroid visible at naked eye.

The released spheroids were divided in three groups: one group for the viability assay (2 spheroids per condition), one group for AFM mechanical stimulation (at least 2 spheroids per condition), and the last group for immunofluorescence optical sectioning (at least 2 spheroids per condition).

6.3.2 Viability assay

To check the cell vitality and exclude the presence of a necrotic core, one spheroid per each condition was stained using the LIVE/DEAD™ viability/cytotoxicity kit (Invitrogen® L3224). In that way, cells were labeled with green-fluorescent calcein-AM to show esterase activity inside the cytoplasm, and red-fluorescent ethidium homodimer-1 to show the loss of plasma membrane integrity. Therefore, a quick, positive discrimination between viable and non-viable cells was made possible by acquiring a Z-stack series of the lower, middle, and upper spheroid sections using an EVOS M5000 Cell Imaging System (Thermo Fisher Scientific Inc.) right after the spheroid release.

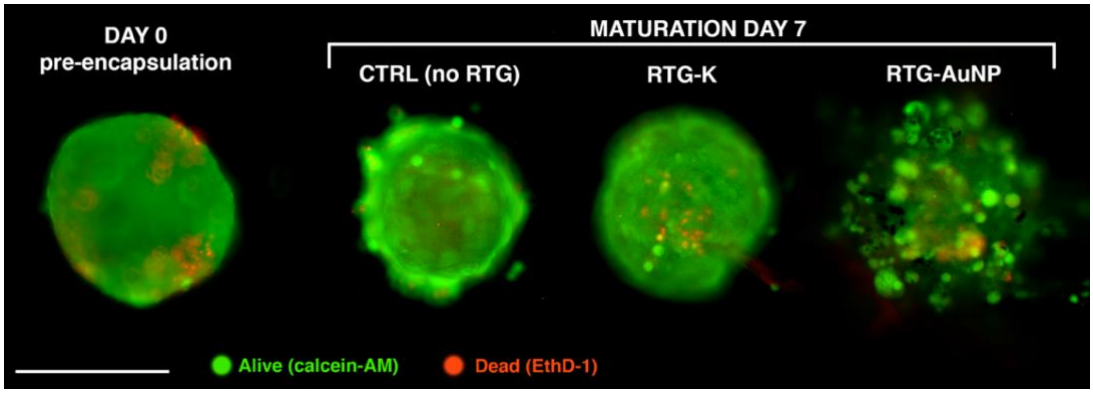

Figure 6.2. Exemplificative Live/Dead staining of spheroids before encapsulation (day 0) and after 7 days of RTG-conditioning.

6.3.3 Mechanical features of NRVMs Spheroids

The experimental procedure is already discussed in Chapter 4, however, some slight variations regarding this specific work are herein discussed. The mechanical characterization of CSs was carried out using a JPK Nanowizard® 4 AFM equipped with a CellHesion® module (Bruker Inc.) in physiological conditions, by using the dedicated JPK Petri dish heater, and by supplementing the media with Hepes (25 mM) to keep its buffering capabilities outside the incubator. Stress-relaxation measurements were performed by squeezing the spheroid with a Z-piezo extension of 15 μm with an extension speed of 30 μm/s. The Generalized Maxwell fitting procedure was applied to evaluate the viscoelastic relaxation times (τ_1 and τ_2)

6.3.4 CSs mechanical stimulation

During the viscous regime, a disorganized force oscillation could be noticed on the decaying curve. The amplitude of such oscillation was greater by some orders of magnitude than the AFM detection system's noise, for which the manufacturer declares a value < 2 pm [x] that, in our case, translates to values between 2 to 4 pN, depending on the macro-probe. As the oscillation amplitude exceeded 1-2 nN, we could safely ascribe those fluctuations to a cardiomyocyte random beating activity, although not *every* spheroid behaved just like a randomly twitching ball.

Cardiomyocyes greatly improve their contractile performance while actively stimulated (mechanically, or electrically), especially after being matured for long

periods of time. Certainly, adult cardiomyocytes do not beat by themselves. Moreover, as already introduced, when a CSs is mechanically loaded with a progressive amount of force, it counteracts the perceived stress by dynamically tuning its contractile properties, showing larger contraction peaks until reaching structural failure [x].

Therefore, right after the very first stress-relaxation, a dynamic mechanical stimulation was performed on each CS, to activate the quiescent cardiomyocytes and observe any possible synchronous coupling, and the resulting maximum beating force (MBF) thereof. To do so, such stress-relaxation loading was repeated from 20 to 30 times each (with 5 s intervals in-between), and the relaxation curves were interpreted as mechanocardiograms (MCGs).

6.3.4.1 Evaluation of CSs synchronization

For each CS, MCGs were obtained from the relaxation portion of the 10 last-acquired stress-relaxation curves. As before, the same Maxwell fitting procedure was applied to calculate the trend of viscoelastic decay. Then, such trend was subtracted to the relaxation curve itself, resulting in a baselined MCG.

To evaluate NRVMs synchronization into the CS, we visually interpreted the force peaks presented by its MCG. A disorganized force oscillation (< 10 nN, *noisy* peaks) was interpreted as a lack of synchronization. On the contrary, if any larger peak (> 10 nN) could be clearly distinguished from the MCG, such spheroid was marked as *synchronized*.

6.3.4.2 Maximum beating force analysis

To evaluate the MBF of the synchronized CSs, a multipeak fitting of the baselined MCG was done using Igor Pro. Then, the amplitudes of each peak (i.e., the force, as acquired from the AFM) were mediated for each CS.

6.3.4.3 Immunofluorescence optical sectioning

A multichannel Cx-43 and alpha-actinin immunostaining was performed to characterize gap-junction and sarcomere expression and localization.

Primary antibody staining was carried out overnight at 4°C on PFA-fixed spheroids, using a mixture of mouse anti-Sarcomeric-α-actinin or rabbit anti-Connexin-43 mAbs

(Sigma® and Abcam®, respectively, 1:200 dilution in blocking buffer). Then, spheroids were exposed to the secondary staining mix for 1 h 30 min at RT (Alexa Fluor 488 anti-mouse, Alexa Fluor 594 anti-rabbit, Abcam®, 1:500 dilution in blocking buffer). Nuclei were counterstained using DAPI 5 μM, washed three times in PBS, and included in a 10 μL drop of antifade mounting media on a microscope slide.

Spheroids were imaged as a whole, using structured illumination microscopy (SIM) or laser scanning confocal microscopy (LSCM). For SIM, an Axio Observer Z1 inverted microscope equipped with an ApoTome® module (1.6/1.5 transmission grid) and an AxioCam 506 monochrome camera was used (Carl Zeiss AG). Each spheroid was optically sectioned through a 63x/1.4 objective (EC Plan Neofluar, oil immersion) by taking 7-grid projection images in 9-12 tiles, depending on the sample size, at the lower, middle, and upper Z-slices of the spheroid. Images were reconstructed by ApoTome deconvolution and tile fusion using Zeiss ZEN black edition.

For LSCM, an LSM780 NLO inverted microscope (Carl Zeiss AG) equipped with a 34-channel Zeiss QUASAR detector was used. Fluorophores were excited using 488 nm and 561 nm laser lines for α-act and Cx-43 respectively, and nuclei by a MaiTai (Spectra Physics, Inc.) multiphoton laser tuned at 820 nm. Each spheroid was imaged through a 40x/1.2 objective (C-Apochromat, water immersion) following the same tile scheme described above for SIM. Tiles were fused together using ZEN black edition.

6.3.4.4 Evaluation of Connexin-43 expression

Cx-43 is a connexin that localizes on the plasma membrane, where electrical coupling with neighboring cells occurs [x]. It is a component of the gap junction assembly, and its distribution can be observed as individual particles or clusters thereof [x].

To evaluate Cx-43 expression, a particle count-based analysis was conducted using Fiji [x] by considering the lower and middle optical sections of each spheroid. First, the red channel was thresholded and converted into a binary image. Then, a watershed segmentation function [x] was applied to separate the clusters into smaller ones. For the lower plane, five 400 um^2 randomly selected ROIs were manually placed across the spheroid's slice, and single particles counted using a 4-pixel lower cutoff to limit the background noise contribution. For the middle plane, such ROIs were placed on

the spheroid's outermost layer (last 50 μm) accounting for possible artifacts, given by different fluorophore penetration rates, which were noticeable only at the CS center. Finally, the number of Cx-43 particles was averaged and is hereby represented as particle count per 100 um^2.

6.4 RTG conditioning does not influence CS viscoelasticity

After the sudden compression, the force decayed bimodally, displaying a fast elastic recovery lasting up to two seconds, followed by a longer viscous dissipation, as also seen in our previous works on hanging-drop cultured cardiomyocytes [x], tumor spheroids [x], and oocytes [x].

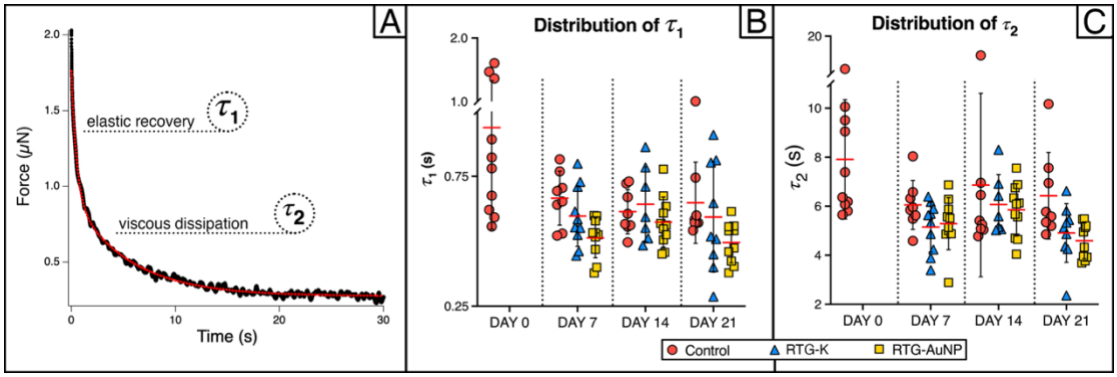

Figure 6.3 **A)** an exemplificative relaxation curve, as probed on day 7 on a CTRL CSs (black line), showing the two-component Maxwell fitting (red line) and highlighting the two decay regimens. **B,C)** Data distribution for the first and the second relaxation times (respectively) grouped per each experimental timepoint. Growth conditions (i.e., hydrogel conditioning) are nested within each group. Mean ± SD are represented by the red dash and black whiskers, respectively. CTRL and RTG-K spheroids were pooled from 5 independent replicates. RTG-Au spheroids were pooled from 4 replicates. At least 2 spheroids were probed in each experimental replicate.

Accordingly, two distinct relaxation times were extrapolated from the data (Figure 6.3); τ_1 is generally attributed to a quick recoil of CSs' elastic components, i.e., some of its ECM proteins such collagen, while τ_2 is related to the viscous readaptation of those cells experiencing a breakage of their adhesive contacts [x]. Both relaxation times showed to be consistent for up to 21 days of maturation, except for the pre-encapsulated spheroids (day 0), which were slower in terms of both elastic and viscous relaxation. At day 7, 14, and 21 CTRL, RTG-K, and RTG-Au behaved similarly, in terms of both initial elastic recovery (Figure 6.3, B) and viscous dissipation (Figure 6.3, C).

During the viscous regime, a disorganized oscillation could be noticed on the decaying curve (Figure 6.3, A). The amplitude of such oscillation was greater by some orders of magnitude than the AFM detection system's noise, for which the manufacturer declares a value < 2 pm [x] that, in our case, translates to values between 2 to 4 pN, depending on the macro-probe. Nevertheless, it should be noted that our setup was

not generally optimized for sub-nanonewton force measurements, as the usage of large cantilevers, the presence of a warm liquid environment, and the sudden initial compression (which moved a relatively large amount of fluid) all rowed against that.

However, as the oscillation amplitude exceeded 1-2 nN, we could safely ascribe those fluctuations to a cardiomyocyte random beating activity, although not every spheroid behaved just like a randomly twitching ball. In fact, after ~ 10 stress-relaxation loadings, some CSs started beating, showing large contraction peaks on the relaxation curve (Figure 6.5, left).

6.5 RTGs conditioning influences beating synchronism

The amount of synchronized beating CSs was evaluated as the ratio between the number of synchronized spheroids and the total number of CSs probed per each hydrogel conditioning group (Figure 6.4).

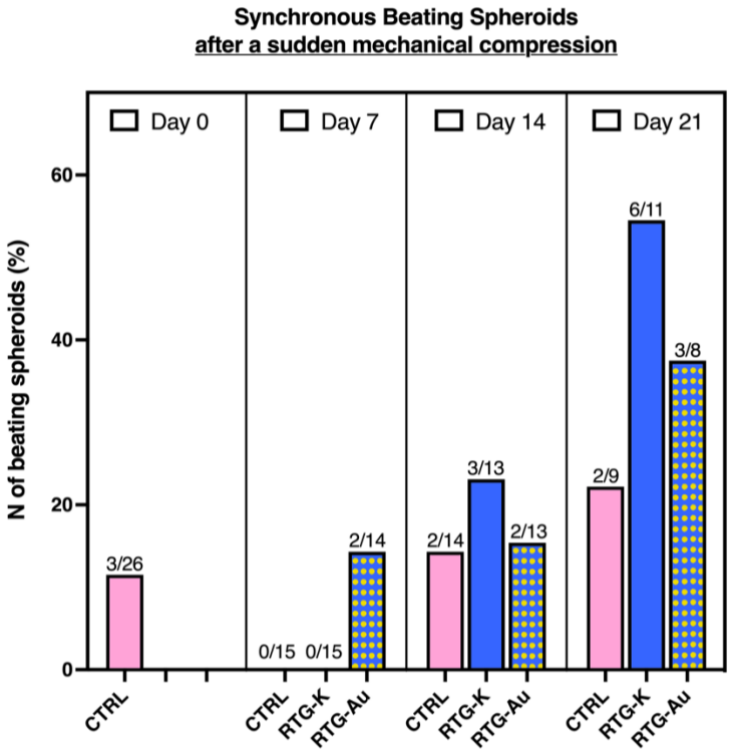

Figure 6.4. Percentage of spheroids displaying at least one synchronous spark per each compression curve. CTRL (pink) represent spheroids grown in absence of RTG-conditioning (bare media). RTG-K (blue) represents the spheroids grown with the RTG-lysine *mechanical* conditioning hydrogel. RTG-Au (blue with yellow dots) represents the spheroids grown into the RTG-Gold-Nanoparticle *electromechanical* conditioning hydrogel. Numbers above each bar represent the number of synced spheroids / total number of spheroids probed per each condition. CTRL and RTG-K spheroids were pooled from 5 independent replicates. RTG-Au spheroids were pooled from 4 replicates. At least 2 spheroids were probed in each experimental replicate.

Before encapsulation, i.e., four days after the spheroid's assembly procedure, a small amount of CSs (about 12 %, Day 0 CTRL in Figure 6.4) showed synced beating sparks. After a week of hydrogel conditioning of such, no CTRL nor CSs grown in lysine gels beat while mechanically stimulated, while about 14% of the ones grown into the conductive AuNP gel showed contraction sparks (Day 7 RTG-Au in Figure 6.4).

After 14 days of hydrogel conditioning, the response to the AFM mechanical stimulation started to be relevant. At day 21, about 60 % of those spheroids grown into

the RTG-K displayed such synchronization, followed by the RTG-Au ones (38%), while the number of synced unconditioned CTRLs stayed relatively low throughout all the experimental timepoints. Although the inclusion of gold nanoparticles in the RTG-Au gel lowered the material's electrical resistance, encapsulation in those gels did not enhance synchronization, compared to those grown in RTG-K. Therefore, the addition of gold nanoparticle in the RTG-Au gel does not further increases the spheroids' synchronization capabilities.

These results demonstrate that an active mechanical load influences the dynamic activity of NRVMs in cardiac spheroids which were electro-mechanically pre-conditioned into the RTGs.

For a long time, it has been thought that electrical communication between cardiomyocytes plays a key role in the synchronization of their pulsations [x], but recent findings suggest a that mechanical interplay may also be involved [x]. Indeed, the existence of a mechano-electric feedback (MEF, i.e., a feedback loop arising when mechanosensitive channels such as Piezo-1 [x] are mechanically stretched) within cardiomyocytes is a longstanding concept [x]. In a similar effort of ours, other authors observed an enhanced electromechanical coupling of hPSC-CM aggregates under parallel plate uniaxial loading showing that, although such aggregates had weak, asynchronous contractions on their own, a mechanical compression could be a trigger for their strong mechanical beating [x].

In our case and in addition, way before the AFM-induced deformation, a forced mechanical confinement was induced by trapping the spheroids into the RTGs. In fact, as the RTG gelation occurred in proximity and all-around, the spheroid found itself physically trapped into the gel and was mechanically conditioned under static mechanical compression, up to 21 days. Following the recent advances in literature, we can hypothesize a strong contribution by this confinement onto the cardiomyocyte's contractile performance [x], even if it remains unclear whether the gold nanoparticles helped or hindered this process, since the RTG-Au samples were still displaying lower synchronicity after 14 and 21 days. Whilst this trend is not statistically significant due to a limited population number, it is also worth mentioning

that the mechanical properties of the RTG-K and RTG-Au gels are different. More specifically, the mean storage modulus varies from G' = 182 Pa for RTG-K to G' = 255 Pa for RTG-Au as measured in previous experiments on 3% gels [x]. Hence, the conductive one is stiffer by a factor of 1.4 and this difference might be the reason for the lower mechanical reactivity showed by the RTG-Au grown spheroids. Therefore, a softer gel might represent a better growth substrate for our 3D constructs, but additional experiments are required to confirm this compliancy.

6.6 RTG-Au conditioning boosts CSs' q

We have shown how an active mechanical load influences the dynamic activity of NRVMs in cardiac spheroids which were mechanically pre-conditioned into RTGs. Thanks to our approach, we were able to identify those peaks indicating synchronism, and evaluate their twitch force. After 14 days of hydrogel maturation, both RTGs showed higher average beating amplitudes compared to CTRLs (Figure 6.5). However, such difference sparked after 21 days, when RTG-Au CSs showed a higher average beating force even when compared to the RTG-K ones. After three weeks, both RTG samples outperformed the control group in terms of beating force, reaching contraction peaks close to 2 μN in the case of RTG-Au CSs. [xxx]

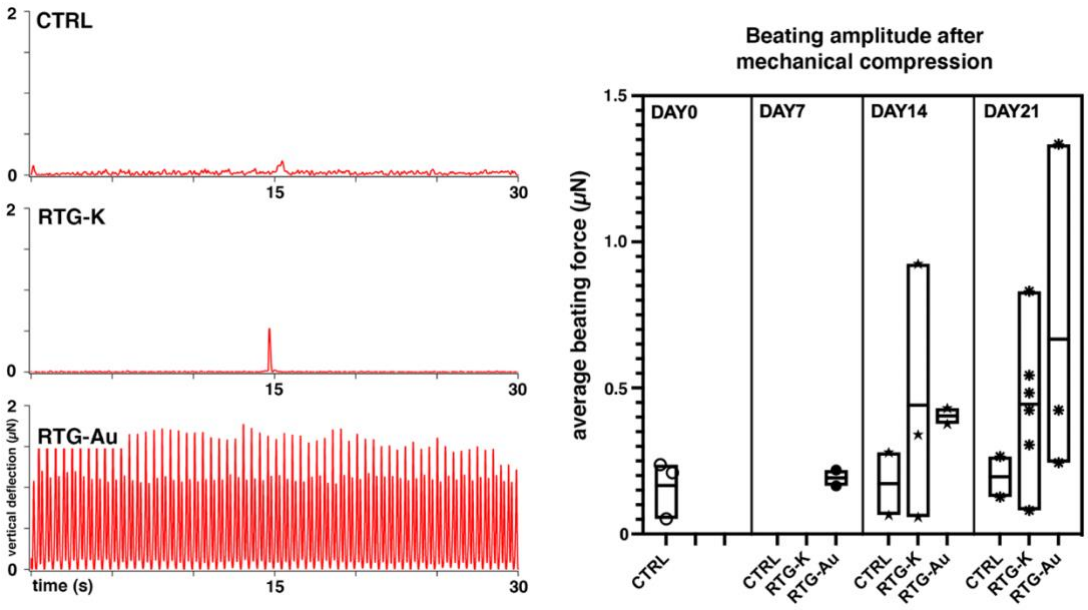

Figure 6.5. **Left**, three representative MCGs referenced to baseline after relaxation fit subtraction. **Right**, data distribution of the calculated force amplitudes.

6.7 RTG conditioning elevates CSs' gap junction expression

In a previous work, it has been shown how by culturing sparse single cardiomyocytes into a 3D scaffold made of RTG-Au led to an improvement of their electrical communication by augmenting cellular Cx-43 expression after 21 days of fibroblast co-culture [Brisa].

We observed a similar effect in the in the present study by electromechanically conditioning CSs. The analysis of the SIM and LSCM immunofluorescence images (Figure 6.6) shows that CSs cultured in the RTG-Au hydrogel for 21 days averaged a greater count of Cx-43 particles (113 ± 50 / 100 μm²) compared to CSs cultured in the RTG-K hydrogel (40 ± 22 / 100 μm²) and to the CTRL CSs kept in bare media (48 ± 11 / 100 μm²). The same goes for CSs grown for one or two weeks, but this difference is less pronounced.

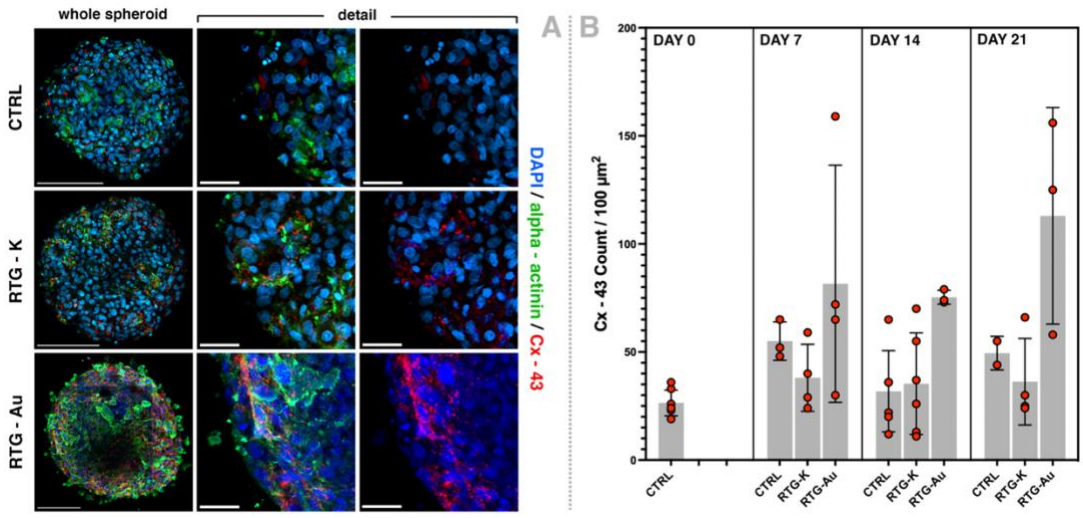

Figure 6.6. **A)** Whole-spheroid mount and detailed IF mid-sections, showing DAPI-stained nuclei (blue), Scale-bars for the whole spheroids: 100 μm. Scale-bars for the detailed sections: 20 μm. These specific CTRL and RTG-K representative images were acquired using SIM, while LSCM was used to image this specific RTG-Au. **B)** Data distribution of Cx-43 expression as estimated by particle count analysis. Each red dot is the result of the average count inside five ROIs (each red dot represents one spheroid).

The protein Cx-43 is highly expressed in the myocardium, as it makes up the gap junctions, which are ion exchange channels that allow the propagation of calcium transients between cardiomyocytes. A down-regulation of Cx-43 is

correlated with an impaired cardiac function [x]. For example, Cx-43 expression in the heart is strongly remodeled in various forms of cardiomyopathy. Therefore, numerous efforts are being made to improve electrical coupling and, ultimately, reduce the frequent arrhythmias seen in these diseases [x]. In a previous work performed by Tan et al., NRVM CSs were grown scaffold-free by adding trace amounts of conductive silicon nanowires (e-SiNWs) [x] during spheroid's assembly. While - as in our case - such spheroids' spontaneous beating activity was weak and occasional, the average beating amplitude after active electrical pacing was remarkably higher (> 55%) compared to the non-treated spheroids.

However, the nature of our stimulation was different, as we used a mechanical stimulation instead of an electrical pacing, but the observed results were comparable. Therefore, it is reasonable to assume that the enhanced electroactivity and twitch power are not primarily due to the nature of the stimulation itself, but rather to the electrical cues provided by the material in which the spheroids are grown.

REFERENCES

Conclusion

Mechanobiology of heart tissue is a rapidly growing field of research that holds important promises in numerous fields. The rising availability of three-dimensional constructs for heart tissue modeling could help create novel drug-testing platforms, further reducing the gap between animal models and the human heart. Moreover, it opens new possibilities regarding the bio-fabrication of cardiac patches for infarcted tissue regeneration in personalized medicine. On another side, the AFM is a powerful tool to inspect these constructs' mechanical properties but is practically limited by their size, allowing a local nano-investigation only. For this reason, we have shown how it is possible to extend the AFM capabilities to the mechanical investigation of cardiac spheroids by fabricating flat macro-cantilevers. We have designed and later performed their micromachining in a cleanroom environment and showed their optical and SEM characterization. We have used these macro-probes to perform stress-relaxation measurements of whole cardiac spheroids made of primary neonatal rat cardiomyocytes. We were able to measure their beating force and frequency, and we stimulated their beating via the AFM itself via a so-called "micro-CPR". To our knowledge, this was the first time cardiac spheroids were individually probed and stimulated by such a sensitive instrument.

Furtherly, such spheroidal models were used to mimic a fibrotic condition. With that, we investigated the mechanics of myocardial fibrosis using a 3D co-culture model of NRVMs and fibroblasts. We found that pre-culturing fibroblasts on 2D hard surfaces promotes fibrotic proliferation in 3D, which is a key feature of MF. To model a 3D fibrotic tissue that more closely mimics the in vivo situation, we co-cultured these fibroblasts into 3D CM spheroids. The mechanical properties of these co-cultured spheroids exhibit a two-phase decay, characterized by a quick viscoelastic recovery followed by a slower viscoelastic dissipation. We found that both relaxation times showed a lowering trend in the case of fibrotic spheroids when compared to control spheroids. The fact that fibrotic spheroids exhibit a lower relaxation time is consistent

with the known stiffening of the heart muscle in MF, and our study highlights the importance of developing improved models and techniques to better understand the underlying mechanisms of MF. The 3D co-culture model and the use of macro-cantilevers are steps forward in this field and may be useful in developing new strategies for the treatment of this globally detrimental disease.

Finally, we went on by studying the importance of an electromechanical conditioning of cardiomyocytes in a confined 3D environment, from the maturation perspective. Indeed, NRVM spheroids grown in compliant nano-engineered hydrogels demonstrated advanced levels of maturation, as indicated by increased gap junction expression, beating synchronism, and stronger beating force.

Such research greatly benefited from the employment of custom-made macro cantilevers as well, as they enabled to probe the CSs' viscoelasticity in one-shot and, at the same time, to enhance CSs contractility by active mechanical pacing.

Our findings indicate the conductive RTG-Au gels improved CSs' contractility by providing the necessary electrical cues as the cardiomyocytes grew in close relationship with it, resulting in higher Cx-43 expression and higher contraction amplitudes.

Indeed, the RTG-Au provided long-term mechanical and electrophysiological cues to the cardiac spheroids, and the discussed results suggest a prolonged electromechanical confinement might represent an effective strategy to promote the transition from a neonatal-like to an adult-like phenotype in spheroidal models.

However, the RTG-Au hydrogel full potential is not limited to CSs conditioning, as it is also important to note that RTGs are highly versatile, performing sol-gel transition by simply tuning the environmental temperature. This represents a remarkable solution for such applications requiring a provisional scaffold that needs to be dissolved once a desired maturation level is reached. Therefore, RTG-Au could successfully be exploited as a pre-conditioning vessel for different 3D cardiac constructs meant for organ bioprinting, disease modeling, and drug testing.

In the end, we hope this journey has conveyed to the reader the immense potential of combining micro and nanotechnologies for the advancement of heart research. Our technologies allowed us not only to investigate, but also to improve the mechanical and electrophysiological properties of the in-vitro cardiac tissue, with unprecedented precision and unmatched sensitivity.

As we move forward, it is our hope a continued multidisciplinary effort will unravel the complexities of the heart and ultimately improve the lives of those affected by heart disease. The future of cardiac research is bright, and we are confident that the work presented in this dissertation will continue to inspire and drive further innovation in the field of the Heart Mechanobiology.

APPENDIX

AFM Macro probes for parallelized cell-cell adhesion measurements and mass estimation.

8.1 Introduction

AFM Macro-probes hold tremendous potential for the mechanical characterization of cardiac spheroids, being able to interrogate their viscoelasticity, as well as contractile properties. Here, an additional application regarding the investigation of intercellular adhesion is introduced.

Adhesion forces play a pivotal role in regulating tissue organization during morphogenesis and post-developmental life, which both require a well-defined control of cell-cell and cell-ECM interaction. Indeed, cell adhesion is involved in stimulating signals that regulate cell cycle, cell migration, and cell survival [1] where it plays an important role in embryogenesis and cell differentiation [2]. Alterations in cell adhesion physiology is associated with several major diseases such as cancer [3,4] and heart failure [5,6].

The cellular adhesion to other cells or to the extracellular matrix is mediated by several families of cell-adhesion molecules (CAMs) which are usually transmembrane glycoproteins that bind firmly with the cytoskeleton via their cytoplasmic domain, and have an extracellular specialized domain to recognize its adhesion counterpart but may also act as membrane receptor. The most conserved families are integrins, heterodimeric molecules responsible for cell-substrate adhesion [7], and cadherins, which are a family of glycoproteins found in most kinds of tissues. Antibody passivation of cadherins results in the dissociation of cell layers, indicating their fundamental role in controlling the multicellular organization. [8]. An important subfamily of the latter are desmoplakin and desmocollins whose mutations are thought to be the main cause of arrhythmogenic cardiomyopathy [9].

Cell adhesion mechanisms have been extensively investigated in the last decades for their importance in several life-threatening diseases, however many questions remain open and many other aspects still need to be addressed, because of the experimental difficulties to quantify adhesion forces in a physiological environment.

Traditionally, in biology laboratories, the adhesion capabilities of the cells are investigated using washing assays, in which cells in culture are more or less energetically washed, and the percentage of remaining ones is evaluated. Several improvements have been proposed in the years but this approach, although easy and

statistically relevant, just provide a purely qualitative on/off answer [10]. Microfluidics helps in the application of a more controlled shear force: cells are exposed to a laminar flow and the detachment is observed in real time under a microscope. Unfortunately, cell shape and size influence significantly the actual value of the applied force, so that these assays still provide only qualitative information [11]; moreover, only lateral forces are investigated which do not cover all the possible adhesion interactions of interest. A general drawback of the traditional cell-adhesion assay is that they address specifically cell-substrate interaction, while it is much more difficult to investigate cell-cell adhesion. Indeed, cells in vitro tend to grow in monolayers or develop quasi 3D structures, which is not representative of the natural 3D environment and of its natural cell-cell adhesion interaction.

To exploit the richer variety of interactions, in term of type of molecules involved, cell geometry, force values, force direction, and so on, a single cell approach is needed. The oldest method is based on micropipettes aspiration to manipulate cells. The range of measurable forces depends on the specific approach adopted and can be as small as fractions of pN [12] to μN [13]. In optical tweezers, a micropipette is replaced with an optical trap whose force depend on the laser intensity and is therefore limited to a few hundred of pN [14]. Both methods deal mostly with cells in suspension and may miss some features typical of adherent cells grown within a solid environment.

Atomic force microscopy (AFM) based single cell force spectroscopy (SCFS), on the other hand, offers extreme versatility and an unpaired range of forces, from 5 pN, the breaking of a single hydrogen bond, to about 100 nN, the force exerted by a cell undergoing mitosis [15]. Usually, in AFM-SCFS cell adhesion experiment, an individual suspended or weakly adherent cell is fished on a protein coated cantilever, allowed to stabilize for 5 – 30 minutes, and then brought in contact with the sample, controlling time and pressure during the contact. SCFS has been employed on an enormous variety of situations such as breast cancer cells [16], glioma [17], bacteria [18], stem cells [2]. A common feature of all the mentioned experiments, and of the many others not cited here is the limited number of cells investigated per condition, which seldom exceeds the 100 units: this because the cells once attached to the cantilever can no longer be detached and therefore a fresh cantilever is required. This

process is expensive and time consuming and limits significantly the statistical relevance of these experiment. A second common feature is that experiments are usually performed on cell lines or cancer cells since they display fast recover rates after being fished on the cantilever. On the contrary, experiments with delicate primary cell culture, such as neurons or cardiomyocytes, or with cells derived from human induced pluripotent stem cells are difficult to design since the suffering condition of the just-fished cells pose the high risk of result misinterpretation.

Recently, a solution to the scarce size of the sample in cell-cell adhesion measurements have been offered by the introduction of FluidFM [19], basically a hollow cantilever, which acts at the same time as a micropipette. By a suction process, a cell can be hold firmly on the cantilever, brought in contact with the desired target, adhesion forces measured and finally discarded, with the cantilever ready to pick up another cell. [20] In this way up to 20 cells can be investigated using the same probe, and up to 100 cells can be measured during a single session, which enable to reach a statistical regime compatible with biological standards. Unfortunately, the second drawback described above about AFM-SCFM remains unchallenged.

For an exhaustive review of the available adhesion assays, we invite the reader to look at the historical perspective by Rita Ungai-Salánki, et al. [21]. For a review focused on AFM-SCFM we refer to the excellent paper by Helenius at al. [22]

In this method paper we propose an alternative approach, based on the fabrication of AFM macro- cantilevers able to host up to 100 cells, depending on the cell size. The main difference with the traditional approach is that the cells under investigations are cultured directly on the cantilever, which opens the field to extremely sensitive culture, and allows the investigation of the adhesion properties of a statistically significative population in a single shot. The price to pay is a moderate loss in sensitivity, and of the membrane tethers that characterize the final portion of the retraction curve in a traditional single cell force spectrum.

8.2 Experiment pipeline

The main purpose of this experiment was to demonstrate that, by using our macro-cantilevers, we can obtain a mediated information with higher statistical significance but still retaining the qualitative and quantitative information provided by SCFS. As a test sample we choose to use human embryonic kidney cells (HEK 293), for they are easily cultured on bare glass without the need of poly-l-lysin or gelatin coating that could influence the mechanical response of the cantilever. Moreover, HEK 293 is a very well-known cell line, easy to characterize and find in every laboratory. SCFM on HEK cells showed single cell adhesion forces ranging from 600 pN when the substrate is covered by a monolayer of fibrinogen (which maximizes adhesion), to 190 pN on bare uncoated mica. It was also shown that 120 seconds of contact time are required to develop full adhesion [26].

8.2.1 Geometrical and mechanical implications

Cantilevers were fabricated by standard silicon micromachining as already reported in Chapter 4. The geometry of the AFM macro-cantilevers allowed to have a surface large enough to host about one hundred of cells and to exert enough force to detach all of them at the same time. Considering that the detachment force of an *highly adhesive cell* such as mouse embryonic fibroblast (MEF) grown on sticky substrates as gelatin (collagen) or nanowires is about 0.5 nN [24], and typical cantilever spring constants used in this regard are in the range of 0.05 N/m, we expected to observe detachment forces as large as 100nN. Therefore, the theoretical spring constant of 4 N/m was appropriate for a multiple cell force spectroscopy (MCFS) approach. By reference, we obtained a calibrated spring constant of (7 ± 1) N/m.

8.2.2 Macro probes as a 2D culture surface

HEK cells were grown on cantilevers and on plastic Petri dishes in 10% FBS-supplemented DMEM for 3 dd before experiments. In order to localize the highest possible number of cells on the cantilever flat area, a 10 μL culture droplet containing about 36000 cells in suspension was formed on a highly hydrophobic PDMS surface to

minimize the contact area between the droplet and the supporting surface and thus minimize the number of cells that are lost to the support.

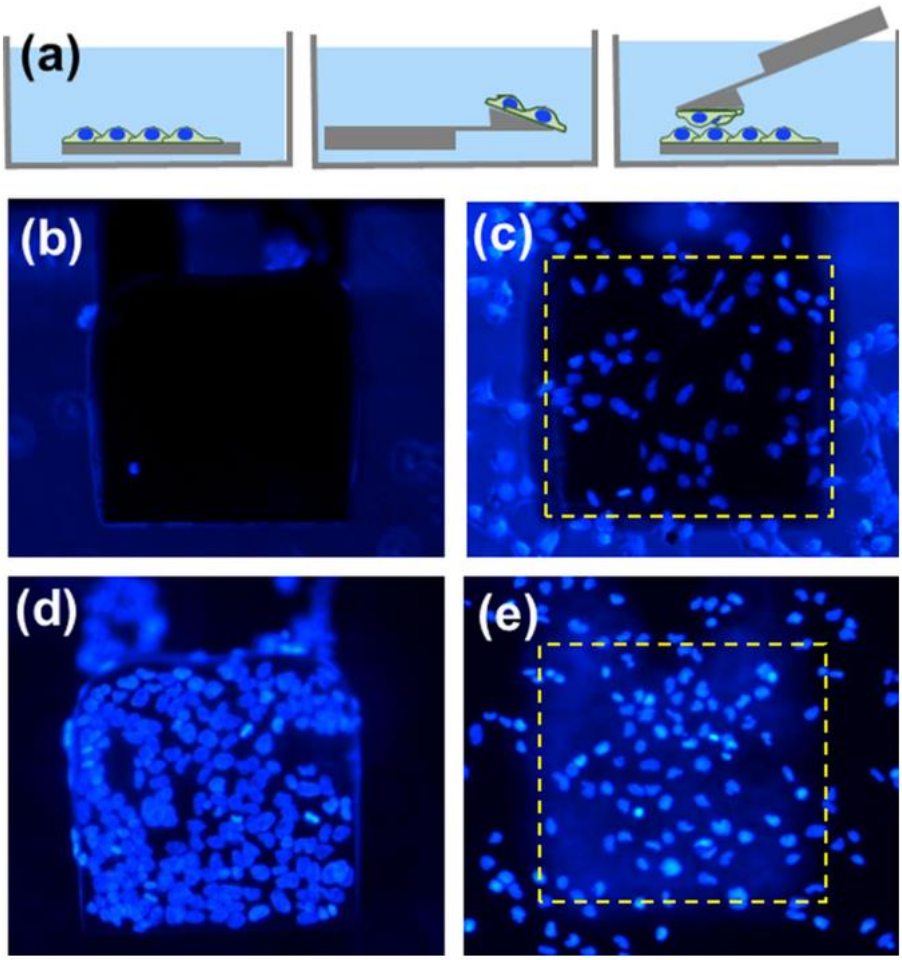

Figure 8.1. a) Schematics of the MCFS experiments. Cells are separately grown on a substrate and on the cantilever in standard Petri dishes, or multiwells, in the incubator. When cells are mature the cantilever is mounted on the AFM head and cells are brought in contact. **b-c)** Fluorescence images of the cell nuclei, live-stained with Hoechst NucBlue. The microscope is focused alternatively on the glass slide or on the cantilever, which for this purpose is kept 100 μm apart, so that nuclei are blurred on the background, but the cantilever profile is still visible and the involved cells on the glass slides can be enumerated. **d-e)** For cell-cell MCFM experiments, the cells on the cantilever are near confluence and it is possible to assume that they form a continuous layer, so that the active number of interactions is determined only by the cells on the glass slide included within the dashed area.

The cantilever was then quickly immersed in the droplet and maintained at 100% humidity atmosphere to limit evaporation for 60 minutes allowing cells to sediment on the cantilever and not on the surrounding superhydrophobic surface.

Then, the cantilever was transferred in a 35 mm Petri dish and placed overnight inside the incubator at 37°C, 5% CO2. For the experiments with HEK cells, both Petri dishes

and cantilever surfaces were not functionalized; however, the cantilevers could be covered with a suitable functionalization if needed, without affecting the overall methodology. 30 minutes prior to measurement, the samples were live-stained with NucBlue to allow the direct counting of the interacting cells.

8.3 Multicellular force spectroscopy

The cantilevers were mounted on a Nanowizard® 4a AFM (JPK Instruments AG) equipped with the CellHesion® stage, making sure that cells did not suffer from medium evaporation. Therefore, both the glass block and the metal holder were previously wetted and more medium was added right after securing the cantilever. After assembly, the whole block was then immediately immersed in the Petri dish where the medium was thermalized at 37°C.

The experimental sequence is schematized in Figure 8.1a.

To record Multicellular Force Spectroscopy (MCFS) measurements, the cells on the cantilever and on the substrates were first imaged and counted taking advantage of the NucBlue staining. The cells involved by the measurement on the substrate were defined using the cantilever shadow. Representative images used for cell counting are shown in Figure 8.1c for cell-cantilever MCFS, and in Figure 8.1e for cell-cell MCFS. In the latter case we only considered the situation where either the cantilever or the Petri dish was covered with a confluent layer, and the other by scattered cells. In this scenario we could assume that all the cells on the partially covered surface find a partner on the confluent side. Within this assumption, we limited the counting to the scattered cells.

After the optical selection of the proper location on the Petri dish, the cantilever was pressed against the surface with a force of 800 nN, either for 20 seconds, shorter than the time for the aggregation of focal adhesion points, or the much longer time of 240 seconds. Finally, the cantilever was retracted at 10 m/sec and the force recorded.

Figure 8.2a shows the adhesion energy, obtained by integrating the area comprised between the negative force part of the retraction curve and the F = 0 axis. The same cantilever was positioned on 9 different locations, in a random sequence, including two positions with no cells on the substrate, and the data are displayed as a function

of the number of cells contacted. We expect the total detachment energy to be proportional to the total number of cells involved in the process, while the detachment force could be dominated by few contacts and display a weaker dependence. Figure 8.2b displays individual curves relative to the measurement on zero and on 95 cells at increasing contact times and on a bare glass for 240 seconds of contact time.

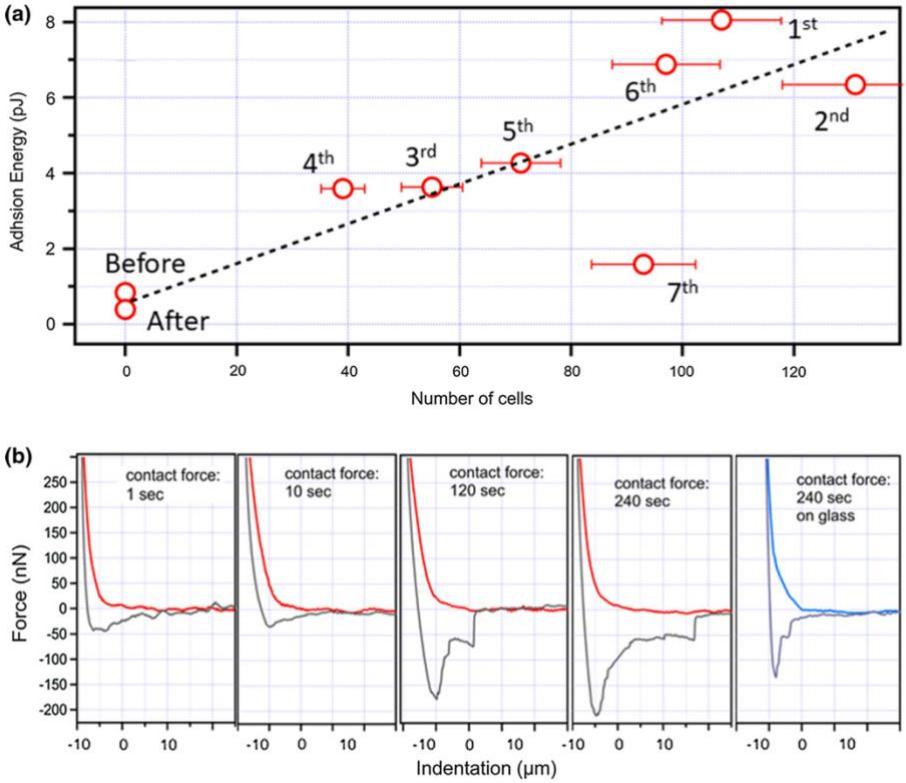

Figure 8.2. a) Adhesion energy is measured for a cantilever with 98 cells grown on it. The cantilever is brought in contact on 9 different positions, with a different cell density. Data are plotted versus the number of cells involved in the adhesions. The numbers close to each experimental point indicates the temporal sequence of the measurement. The dashed line is only meant as a guide for the eyes and has a slope of 40 fJ/cell. First and last measurements were performed on two areas of the substrate free of cells and returned an unspecific adhesion value of 500 pJ. **b)** Force-distance curves at increasing contact time. Cell-cell adhesion develops at 120 seconds of contact. A curve on glass is also displayed for comparison.

We observe that adhesion does not develop for short contact times; when the contact time is long enough, the force peak is only twice for cell-cell with respect to cell-substrate interaction, while the total energy is significantly increased. We can clearly observe a linear increase of the adhesion energy with the number of the cells involved, that can be linearly fitted with an intercept of 500 fJ and a slope of 40 fJ/cell, which is higher than what observed by Yermolenko and coworkers on mica, and compatible

with what observed on fibrinogen coated samples [26]. This difference can be easily understood if we consider that the HEK cells normally investigated by SCFS are collected on the cantilever just few minutes in advance, have no time to rebuild their cytoskeleton and have a still spherical shape, while the cells investigated by MCFM have been in culture for three days, have a well elongated shape, expose a larger membrane surface for adhesion and have a completely reconstituted cytoskeleton. Interestingly, the recorded values do not depend on the measurement sequence; moreover, after the measuring session we repeated the measurement in an area without cell obtaining the same value, thus proving that the measurement does not affect the cell properties.

8.4 MCFS to investigate cytoskeletal alterations

In order to prove the capability of MCFM of catching a biological effect and, at the same time, investigate the role of the cytoskeleton in the determination of the adhesion energy, we treated HEK cell with Cytochalasin D. Cytochalasin D is known to alter actin polymerization and the organization of actin filaments, and thus to affect cell mechanics and cell adhesion properties [32].

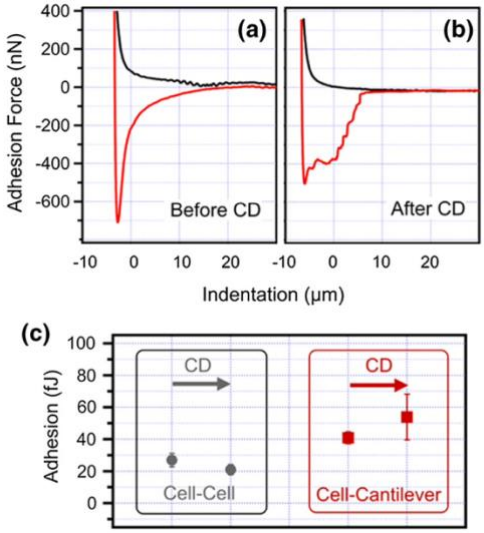

Figure 8.3. **a)** Force-distance curves for the same group of cells before and after Cytochalasin D incubation. **b)** The adhesion per cell value obtained before and after Cytochalasin D incubation in the case of cell-cell and cell-cantilever interaction.

After measuring both cell-cell and cell-cantilever MCFS adhesion curves on wild type cells, the same were incubated with a 2 μM solution of Cytochalasin D for 30 minutes, which is the concentration which most affects cellular cytoskeleton [32], and then measured again. We did not observe any cell suffering or detachment after treatment. Two representative adhesion curves, before and after incubation are displayed in Figure 8.3a and 8.3b respectively: the curve shape changes, the force peak is decreased and more tether-like structures, characterized by a flat F-d dependence are observed after the incubation. Indeed, it is well known that the disruption of the cytoskeleton decreases the forces needed to pull membrane tubes out if the cell membrane and increases their number [33]. On the contrary, the overall adhesion force results only slightly affected.

In Figure 8.3c and we display the variation in the cell detachment energy per cell before and after the actin disruption by Cytochalasin D. The data are the results of a variable number of pulling curves from 6 to 26, involving on average 100 cells each. When cell-cell adhesion is considered, the Cytochalasin D action reduces the adhesion energy by a factor 0.75 while when measuring the adhesion of the cells on the glass slide with the bare cantilever it results increased by a factor 1.3. If we consider the measurements as independent events, the differences are not significant with a t-test value of 0.6 and 0.3 respectively. However, if we consider that the variability of our statistical population is at the single cell level and we apply a proper correction factor, which is proportional to the square root of the number of cells in each measurement (roughly 100), and we apply the statistical analysis to the whole population the data results statistically significative. Our findings for the cell-glass situation are remarkably consistent with the results reported by Mescola et al. who measured the adhesion energy between HEK cells and polystyrene beads [34] finding on average a 30% increase for Cytochalasin D – treated cells, which they attributed to the change in the cytoskeleton contribution. On the contrary, in the cell-cell situation the adhesion energy per cell is half than in the previous case and is further reduced by the effect of Cytochalasin D. A possible explanation is that in this latter case the contact force is shared between two opposite cells and is not enough to trigger the formation of focal adhesion points and the mechanical link between membrane and cytoskeleton.

Indeed, Mescola et al. did not observe any effect of Cytochalasin D when considering the height of the steps, which depends only on membrane properties. However, these observations are not conclusive, and more specific experiments with a more precise control of the substrate chemistry, and a precise evaluation of the approach forces are required to get more insight on this topic.

8.5 Macro probes as micromechanical resonators

Our macrocantilevers can be seen as micromechanical resonators. Micromechanical resonators have been used to detect of single cells [27], single viruses [28] down to DNA molecules [29]; more recently the group of Daniel Müller [30] was able to use cantilevers to track the mass variation of a single cell during the cell cycle, recording fluctuation of ± 4%. Taking advantage on the micromechanical nature of the macrocantilevers, we also explored the possibility of counting the cells deposited on

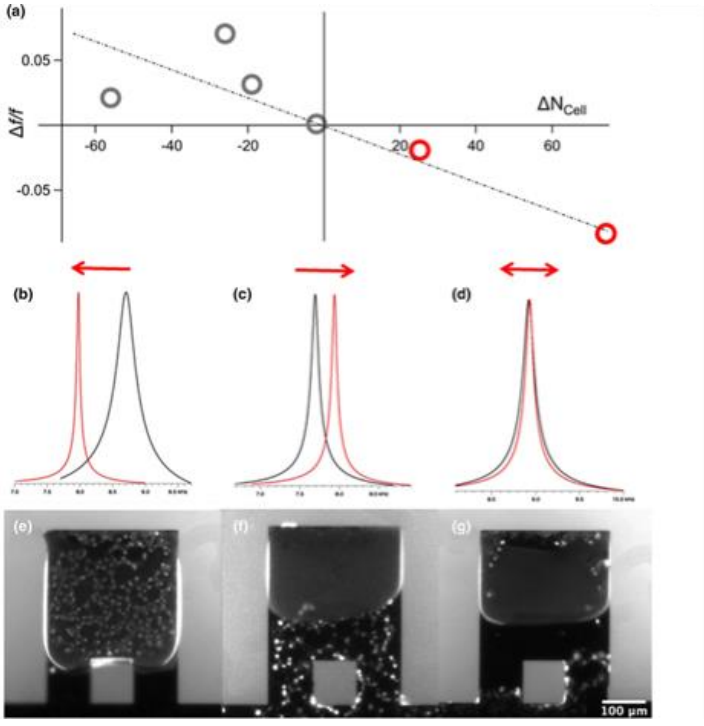

Figure 8.4. Enumeration of the cells on the cantilever by the measurement of the resonance frequency shift. **a)** relative resonance frequency shift versus the number of cells on the microcantilever reduced by the number of cells on the legs; grey points are used when the number of cells on the legs is greater than those on the flat area, red point for the opposite case; **b-d)** Plots of frequency response of the cantilever before (black curve) and after (red curve) the cell growth. The plots refer to the situation depicted by the underneath image; **e)** most cells grown on the flat; **f)** most cells grown on the legs; g) cells evenly distributed on the flat and on the legs. The images in **e-g** are the superposition of bright field and epifluorescence of the nuclei marked with DAPI after fixation and dehydration.

the cantilever by evaluating the shift of their resonance frequency. The resonance frequency has been recorded before and after the cell growth on each microcantilever in dry conditions using the same software of the AFM microscope: cells were grown as previously described, fixed (PFA 2% for 15 minutes), DAPI-stained, and subjected to ethanol series dehydration. Nuclei were independently enumerated by epifluorescence microscopy.

The relative frequency shift is displayed in Figure 8.4a as a function of the difference of the number of the cells on the flat area and of those on the legs, using red marks for positive values and grey marks for negative values. Representative resonance frequency spectra with the relative cell distribution are displayed in Figure 8.4b and 8.4e for cells only on flat, Figure 8.4c and 8.4f for cells only on the legs and Figure 8.4d and 8.4g, for cells evenly distributed on flat and legs. When the cells grow on the flat, they increase the oscillator mass, thus causing a negative frequency shift (Figure 8.4b). On the contrary, when the cells grow on the cantilever legs they induce a stiffening of its elastic constant [31] then inducing a positive frequency shift, as shown in Figure 8.4c, finally if cells are both on flat and on the legs their opposite contribution may balance causing an underestimation of the cell number up to a full compensation resulting in no frequency change. A well-controlled cell culture protocol, finely tuned on the cell growth and seeding conditions, should be adopted to use the frequency shift as the only method for cell enumeration.

8.6 Conclusion

We demonstrated that large and flat cantilevers can be used to perform cell-cell and cell substrate measurements on a large cell population increasing the statistical significance of the measurements. Cells under investigation are cultured directly on the cantilevers so that during the experiment their properties are not affected by the procedure of capture on the cantilever, as in standard SCFS protocols.

The obtained adhesion energy data is proportional to the number of cells involved and to the cell properties: in particular, we showed that adhesion forces and energies, as well as the force distance curves are affected by the modification of the cytoskeleton structure induced by the exposure to Cytochalasin D.

The adoption of the MCFS approach could be beneficial in all the scientific topics involving the evaluation of the overall cell adhesion energy, and not focused on rupture forces at the single receptor level, since it would speed up the experimental data acquisition. However, the most promising application of MCFS concerns those cells whose culture conditions are particularly difficult and cannot be adapted to weakly interacting substrates and to the subsequent fishing protocols such as neurons and cardiomyocytes from primary cultures or derived from induced pluripotent stem cells.

8.7 References

[1] Huang S., Ingber D.E. The structural and mechanical complexity of cell-growth control. Nat. Cell Biol. 1999;1:E131

[2] Migliorini, et al. Nanomechanics controls neuronal precursors adhesion and differentiation. 2013 Biotechnology and Bioengineering 110(8), pp. 2301-2310

[3] Okegawa T., Pong R.-C., Li Y., Hsieh J.-T. The role of cell adhesion molecule in cancer progression and its application in cancer therapy. Acta Biochim. Pol. 2004;51:445–457.

[4] Wijnhoven, B.P.L., Dinjens, W.N.M., Pignatelli, M E-cadherin-catenin cell-cell adhesion complex and human cancer 2000 British Journal of Surgery 87(8), pp. 992-1005

[5] Devaux, B., Scholz, D., Hirche, A., Klovekorn, W.P., Schaper, J. Upregulation of cell adhesion molecules and the presence of low grade inflammation in human chronic heart failure 1997 European Heart Journal 18(3), pp. 470-479

[6] L. Puzzi et al. Knock Down of Plakophillin 2 Dysregulates Adhesion Pathway through Upregulation of miR200b and Alters the Mechanical Properties in Cardiac Cells 2019 Cells 8(12):1639.

[7] Albelda, S.M., Buck, C.A Integrins and other cell adhesion molecules 1990 FASEB Journal 4(11), pp. 2868-2880

[8] Takeichi Masatoshi The cadherins: Cell-cell adhesion molecules controlling animal morphogenesis 1988 Development 102(4), pp. 639-655

[9] Camors, et al. Lethality Due to a Novel Desmoplakin Variant Causing Infantile Epidermolysis Bullosa Simplex with Fragile Skin, Aplasia Cutis Congenita, and Arrhythmogenic Cardiomyopathy 2020 Circulation: Genomic and Precision Medicine pp. 98-10

[10] Weitz-Schmidt G., Chreng S. (2011) Cell Adhesion Assays. In: Shimaoka M. (eds) Integrin and Cell Adhesion Molecules. Methods in Molecular Biology, vol 757. pp. 15-30

[11] Christ K.V., Williamson, K.B., Masters, K.S., Turner, K.T. Measurement of single-cell adhesion strength using a microfluidic assay 2010 Biomedical Microdevices12(3), pp. 443-455

[12] Merkel R, Nassoy P, Leung A, Ritchie K, Evans E. Energy landscapes of receptor-ligand bonds explored with dynamic force spectroscopy. 1999 Nature, 397, 50–3.

[13] Salánki R, Hős C, Orgovan Norbert, Péter B, Sándor N, Bajtay Z, et al. Single cell adhesion assay using computer-controlled micropipette. 2014 PLoS One 9:e111450.

[14] Zhang Hu and Liu Kuo-Kang Optical tweezers for single cells 2008 Optical tweezers for single cells J. R. Soc. Interface.5671–690

[15] Stewart MP, Helenius J, Toyoda Y, Ramanathan SP, Muller DJ, Hyman AA. Hydrostatic pressure and the actomyosin cortex drive mitotic cell rounding. 2011 Nature. 469 226-30.

[16] Jagoba Iturri, Andreas Weber, María d.M. Vivanco and José L. Toca-Herrera Single-Cell Probe Force Studies to Identify Sox2 Overexpression-Promoted Cell Adhesion in MCF7 Breast Cancer Cells 2020 Cells, 9(4), 935

[17] Andolfi, L., Bourkoula, E., Migliorini, E., Palma, A., Pucer, A., Skrap, M. 2015, Scoles, G., Beltrami, A.P., Cesselli, D., Lazzarino, M. Investigation of adhesion and mechanical properties of human glioma cells by single cell force spectroscopy and atomic force microscopy PLoS ONE, 2014 9, art. no. e112582

[18] Dufrêne, Y.F. Sticky microbes: Forces in microbial cell adhesion 2015 Trends in Microbiology 23(6), pp. 376-382

[19] Guillaume-Gentil, O., Potthoff, E., Ossola D., Franz C.M., Zambelli, T., Vorholt, J.A. Force-controlled manipulation of single cells: From AFM to FluidFM 2014 Trends in Biotechnology 32(7), pp. 381-388

[20] Eva Potthoff, Orane Guillaume-Gentil, Dario Ossola, Jérôme Polesel-Maris, Salomé LeibundGut-Landmann, Tomaso Zambelli, Julia A. Vorholt Rapid and Serial Quantification of Adhesion Forces of Yeast and Mammalian Cells 2012 PLOS-ONE 7, e52712

[21] Rita Ungai-Salánki, et al. A practical review on the measurement tools for cellular adhesion force Advances in Colloid and Interface Science Volume 269, July 2019, Pages 309-333

[22] Jonne Helenius, Carl-Philipp Heisenberg, Hermann E. Gaub, Daniel J. Muller Single-cell force spectroscopy 2008 Journal of Cell Science 121: 1785-179

[23] Laura Andolfi et al. Planar AFM macro-probes to study the biomechanical properties of large cells and 3D cell spheroids. 2019 Acta Biomaterialia 94505–513

[24] Laura Andolfi, Anna Murello, Damiano Cassese, Jelena Ban, Simone Dal Zilio and Marco Lazzarino. High aspect ratio silicon nanowires control fibroblast adhesion and cytoskeleton organization. 2017 Nanotechnology 28, 155102

[25] M.P. Stewart, A.W. Hodel, A. Spielhofer, C.J. Cattin, D.J. Müller, J. Helenius, Wedged AFM-cantilevers for parallel plate cell mechanics, 2013 Methods 60,186–194.

[26] Ivan S. Yermolenko et al. Origin of the Nonadhesive Properties of Fibrinogen Matrices Probed by Force Spectroscopy 2010 Langmuir, 26(22), 17269–17277

[27] K. Park, J. Jang, D. Irimia, J. Sturgis, J. Lee, P. Robinson, M. Tonerd and R. Bashir, Living cantilever arrays for characterization of mass of single live cells in fluids. 2008 Lab Chip, 8, 1034–1041

[28] A. Gupta, D. Akin, R. Bashir, Single virus particle mass detection using microresonators with nanoscale thickness, 2004 Applied Physics Letters 84, 1976– 1978

[29] M. Melli, G, Scoles and M . Lazzarino Fast Detection of Biomolecules in Diffusion-Limited Regime Using Micromechanical Pillars 2011 ACS Nano 5, 7928–7935

[30] Martínez-Martín, et al. Inertial picobalance reveals fast mass fluctuations in mammalian cells. 2017, Nature 550, 500–505.

[31] D. Ramos, J. Tamayo, J. Mertens, and M. Calleja and A. Zaballos Origin of the response of nanomechanical resonators to bacteria adsorption 2006 J. Appl. Phys 100, 106105

[32] Tetsuro Wakatsuki, Bill Schwab, Nathan C. Thompson and Elliot L. Elson Effects of cytochalasin D and latrunculin B on mechanical properties of cells 2001 Journal of Cell Science 114:1025-36

[33] Mingzhai Sun et al. Multiple Membrane Tethers Probed by Atomic Force Microscopy 2005 Biophysical Journal 89 4320–4329

[34] Andrea Mescola et al. Probing cytoskeleton organisation of neuroblastoma cells with single-cell force spectroscopy 2012 J. Mol. Recognit. 25, 270–277